Design of Redox Proteins as Catalysts for Fuel Production

by

Zahra Bahrami Dizicheh

A Dissertation Presented in Partial Fulfillment
of the Requirements for the Degree
Doctor of Philosophy

Approved May 2019 by the
Graduate Supervisory Committee:

Giovanna Ghirlanda, Chair
James P. Allen
Dong Kyun Seo

ARIZONA STATE UNIVERSITY

August 2019

ABSTRACT

Redox enzymes represent a big group of proteins and they serve as catalysts for biological processes that involve electron transfer. These proteins contain a redox center that determines their functional properties, and hence, altering this center or incorporating non-biological redox cofactor to proteins has been used as a means to generate redox proteins with desirable activities for biological and chemical applications. Porphyrins and Fe-S clusters are among the most common cofactors that biology employs for electron transfer processes and there have been many studies on potential activities that they offer in redox reactions.

In this dissertation, redox activity of Fe-S clusters and catalytic activity of porphyrins have been explored with regard to protein scaffolds. In the first part, modular property of repeat proteins along with previously established protein design principles have been used to incorporate multiple Fe-S clusters within the repeat protein scaffold. This study is the first example of exploiting a single scaffold to assemble a determined number of clusters. In exploring the catalytic activity of transmetallated porphyrins, a cobalt-porphyrin binding protein known as cytochrome c was employed in a water oxidation photoelectrochemical cell. This system can be further coupled to a hydrogen production electrode to achieve a full water splitting tandem cell. Finally, a cobalt-porphyrin binding protein known as cytochrome b_{562} was employed to design a whole cell catalysis system, and the activity of the surface-displayed protein for hydrogen production was explored photochemically. This system can further be expanded for directed evolution studies and high-throughput screening.

DEDICATION

To Ehsan, my forever best friend

ACKNOWLEDGMENTS

I moved to the US about six years ago to pursue my PhD, with a big hope in my heart for the new chapter in my life upon me, and of course, all the concerns a young student could have about living in a foreign country. I knew there was going to be a challenge to adopt into this almost entirely new environment, and I was even aware there was going to be lots of ups and downs. However, I always believed that I can live anywhere on this globe peacefully, as long as there are great people around me with big hearts, those who do not believe in borders, walls, and bans. To this end, I would like to express my deep and sincere gratitude to the following people:

First and foremost, I wish to express my special appreciation to my advisor, professor Giovanna Ghirlanda. I would like to thank her for encouraging my research and for allowing me to grow as a research scientist. I would also like to thank my committee members, professor James P. Allen and professor Don Kyun Seo for seving as my committee members even at hardship. I also want to thank Dr. Gary F. Moore for serving as my comprehensive exam's committee and for his brilliant comments and suggestions to my project.

I am grateful to Giovanna's present and former lab members: Dr. Anindya Roy for being my first mentor and inspiration to work hard in the lab! Dr. Dayn Sommer, for his support and all the music he used to play in the lab while we were working! Rafael Alcala Torano and Nick Halloran, for all the great moments we shared with each other, my amazing undergraduate students Linh Hazard and Kathrine McDonald for being my hands for mass production of proteins, and for all those nights and weekends we had

spent together in the lab! I would like to thank Dr. Prerna Sharma, for all of her help and support with my projects, and her great insights into scientific questions. Apart from being my colleague, Prerna has turned out to be one of my best friends. I will never forget our time together whether in the lab or trying to let the hardships of our lives go by long conversations. Thank you Prerna for everything, you are just amazing!

I would not have been in the same place where I am today, without my family's support, specially my mom and my sister who have been always there for me, even from miles across the ocean. They could have been present in my defense, but the US travel ban did not let us share a hug at this moment.

To my friends, mentors, instructors: Dr. Scott Lefler, Eduardo Espiritu, Tien Olsen, Alex Jahromi, Zahra Rabet, Andrew Serban, Morteza M. Waskasi, Reza Vatan Meidanshahi, Alan Heays, Lucie Jilkova, Varda Faghir Hagh, Mehdi Sadjadi, Hajar Mazaheri, Zahra Behroozi, Maryam Elyasi, Shahla Gholami, thank you for listening, offering me advice, and supporting me through this entire process.

Last but not least, I want to thank someone who has been my best friend since I was an undergraduate student, and the love of my life for the past few years. Someone who has taught me what an unconditional love means and has been truly there for me in my happiness and sickness. Thank you Ehsan, I have a lot to say, but I just say thank you for being YOU.

TABLE OF CONTENTS

LIST OF TABLES

LIST OF SCHEMES

LIST OF FIGURES

Figure Page

Figure Page

LIST OF EQUATIONS

LIST OF ABBREVIATIONS

Abbreviation	Extended Form
ATP	Adenosine Triphosphate
BME	β-Mercaptoethanol
CD	Circular Dichroism
Co-PPIX	Cobalt-Protoporphyrin IX
CTPR	Consensus Tetratricopeptide Repeat
CV	Cyclic Voltammetry
DAS	Decay-Associated Spectrum
DTT	Dithiothreitol
EADS	Evolution-Associated Difference Spectra
EDTA	Ethylenediaminetetraacetic acid
EPR	Electron Paramagnetic Resonance
ET	Electron Transfer
FT-IR-ATR	Fourier Transformed Infrared-Attenuated Total Reflectance
FTO	Fluorine doped Tin Oxide
GC	Gas Chromatography
GSB	Ground State Bleaching
HiPIP	High Potential iron-sulfur Protein
HPLC	High-Pressure Liquid Chromatography

ICP-MS	Inductively Coupled Plasma Mass Spectroscopy
IM	Inner Membrane
ITO	Indium Tin Oxide
IPCE	Incident Photon to Current Efficiency
IPTG	B-D-1-Thiogalactropyranoside
LMCT	Ligand to Metal Charge Transfer
LPS	Lipopolysaccharides
MALDI	Matrix Assisted Laser Desorption Ionization
MRE	Molar Residue Ellipticity
MWCO	Molecular Weight Cut Off
Ni-NTA	Nickel-Nitrilotriacetic Acid
OD	Optical Density
OM	Outer Membrane
PBS	Phosphate Buffer Saline
PCET	Proton-Coupled Electron Transfer
PET	Photoelectrochemical
PDB	Protein Data Bank
PEC	Photoelectrochemical Cell
RPM	Round Per Minute
RuP	Tris(bipyridine) ruthenium (II) chloride
SCE	Saturated Calomel Electrode

SDS-PAGE	Sodium Dodecyl Sulfate Polyacrylamide Gel Electrophoresis
SWV	Square Wave Voltammetry
TB	Terrific Broth
TCEP	Tris(2-carboxyethyl) phosphine
TCD	Thermal conductivity detector
TCO	Transparent Conductive Oxide
TEV	Tobacco Etch Virus
TFA	Trifluoroacetic acid
TON	Turn Over Number
TPR	Tetratricopeptide Repeat
UV-Vis	Ultraviolet-Visible

CHAPTER 1

INTRODUCTION

Research Aims

The human population is projected to continue growing over the next century, and therefore, there is a critical demand for more energy. Most (84%) of the energy that we are using comes in the form of fossil fuels, which is Earth stored bank of sunlight.[1] While we do not want to run out of that stored bank, using that reserved sunlight makes permanent changes to our climate. Instead, we need renewable and sustainable energy sources. Some of the sources which have been used by humans are wind power, hydroelectric power, and solar power.[2] The problem with all the current renewable sources of energy is that they are all very intermittent. That basically means when the sun sets, or the wind stops, our energy source diminishes. That is why fossil fuels are so popular, because they are the stored form of energy in chemical bonds. Thus, we need a renewable energy source that is scalable and affordable without all the drawbacks. Sunlight is one of the few energy sources that has enormous potential to meet the growing global energy demand. Therefore, efficient and cost-effective systems are required to capture, store, and utilize the solar energy.[3]

The long-term objective of my dissertation is designing and employing porphyrin-binding and Fe-S cluster binding proteins as target catalysts and electron transfer systems, in biofuel production. In chapter, I present a brief description of the following topics: oxidoreductase enzymes in photosynthesis and what we have learned from natural

photosynthesis, long-range electron transfer in enzymes, redox enzymes for biofuel production, biofuel production reactions, Fe-S clusters, porphyrins, and a brief description of each chapter of my dissertation.

Oxidoreductase Enzymes in Photosynthesis

The large-scale solar energy harvesting and storage in nature is photosynthesis, which is executed in green plants and certain bacteria.[4] In photosynthesis, photocatalytic water oxidation coupled to CO_2 reduction transform sunlight to energy dense reduced carbon compounds which provides food and fuels life on earth.[5] In fact, nature provides a blueprint to develop renewable energy sources using the sun light to produce simple and small compounds with the capability to store a sufficient amount of energy. There are three crucial processes involved in photosynthesis including light harvesting, charge separating, and catalytic reactions, and the balance between thermodynamics and kinetics of these reactions determines the overall efficiency of the process.[6] A network of oxidoreductase proteins make an electron transport chain to shuttle electrons through the membrane in photosynthesis. Discovered enzymes which are involved in natural electron transport processes offer a wide range of redox potentials from -800 mV to +400 mV vs SHE.[7] Theoretical models developed by Rudolph Marcus predict electron transfer probability and thermodynamics. Apart from the complexity of involved proteins and cofactor in photosynthesis, the overall process has a very low efficiency (< 1%); thus, it is necessary to simplify this process in biomimetic fuel production.

Long-range Electron Transfer in Enzymes

Electron transfer processes, such as photosynthesis, require transferring electrons

through a long network of involved components in the protein. Electron transfer through large distances (more than 15 Å) via tunneling is not efficient and the mechanism for long-range electron transfer has been the object of a lot of research.[8] Gray et.al have investigated the role of protein matrix in modulating multistep electron tunneling (hopping); their results demonstrated that the distance between redox centers is not the only important factor in determining the electron transport rate and intervening amino acids play an important role in this context.[9,10] In natural metalloenzymes, inorganic cofactors are located with protein scaffolds with optimized distances and orientations with respect to each other and their coordinating ligands.

Redox Enzymes for biofuel production

Studies on biological electron transfer has provided powerful tools for many groups to design bio-inspired oxidoreductase proteins for catalyzing redox reactions, including hydrogen production and water oxidation. A remarkable feature of biological systems is that they employ abundant and non-precious metals such as Mn, Fe, and Ni to catalyze reactions. In addition, biological systems have evolved to possess a high degree of selectivity towards reactions that they catalyze. Finally, the existing balance between kinetics and thermodynamics in biological systems have optimized them for electron transfer catalysis.[11] Despite their critical role in interconversion of energy, natural redox enzymes are not considered as best candidates for biofuel catalysis for several reasons including their complex structure, oxygen sensitivity, and difficulties in studying their mechanism of activity. Large-scale applications of natural enzymes are not trivial as they are typically produced in milligram scale using natural organisms. Due to these reasons,

designed model proteins and peptides are emerging as alternative candidates to interface organometallic complexes with protein scaffolds. In catalyzed biofuel production reactions, the electrons are stored in chemical bonds to form fuels. In order to perform these reactions, electrons must be flowing to or from a place and this can be facilitated by interfacing enzymes with electron transfer modules. These enzymes must have high rates of reaction, be easy to overproduce, and carry low overpotentials for catalysis.[12] In this context, hydrogenases (Scheme 1.1) , the enzymes that catalyze the reversible oxidation of hydrogen, have received substantial attention. Among different types of these enzymes, [FeFe] hydrogenase offers higher rates (TOF up to 21000 s^{-1}) towards hydrogen production from protons and has been a promising candidate for biofuel production catalyst design. The protein environment in these enzymes facilitates the hydrogen production catalysis by providing a pathway for electron and proton transfer to the active site of the enzyme, as well as stabilizing the catalytically-active conformation of the active site.[13] However, hydrogenases function is restricted by their high oxygen sensitivity.[14,15] Many research groups have studied these natural enzymes to design robust and efficient mimics of hydrogenase for biofuel production. The designed redox-active proteins in our lab provide blueprints for improving primary coordination and long-range interactions between the redox center and the protein to stabilize the catalytic site and facilitate proton and electron transfer. The coordination sphere of the catalytic site can be easily modified by mutagenesis and variations can be made to the organometallic center as well. Finally, connecting the catalyst to either electron carriers or an electrode surface requires designing efficient electron transfer networks to transfer electrons to/from the

metal center.[16–18]

A distinctive feature of redox enzymes is harboring a redox-active organometallic cofactor. Iron-sulfur clusters and porphyrins are among the most common organometallic cofactors found in proteins (Figure 1.2), which perform electron transfer and extensive amount of studies have been carried out on them both within natural proteins and designed scaffolds.[19–25]

Fe-S clusters

Iron-sulfur clusters are one of the most ancient and versatile cofactors existing in nature thatfunction in electron transfer and catalysis. They are an important component of complex redox active proteins including hydrogenases and photosystem I.[12] Depending on their function, Fe-S clusters uptake a variety of forms among which [2Fe-2S] and cubane-type [4Fe-4S] are the most prevalent ones. These clusters are buried into the hydrophobic core of proteins through cysteine ligands and bridging inorganic sulfides and they offer a wide range of redox potentials from -700 to +450 mV.[26] The redox potential of Fe-S clusters depend on the solvent accessibility of the cluster, the hydrogen bonding of bridging sulfurs, and the dipole moment of the protein.[27] Two strategies that have been used to design Fe-S cluster binding pockets into model proteins and peptides include computational methods and using minimalistic peptides which are designed based on natural proteins. One of the strategies to design [4Fe-4S] cluster in a helical environment is “metal-first” approach, in which a minimal helical [4Fe-4S] cluster-binding protein is required as a model. In a recent study, a library of C_2 symmetrical helices with a CXXC motif to accommodate the clusters were designed and connected to

two additional helices in an antiparallel manner through insertion of loops. The [4Fe-4S] cluster was then reconstituted into the resulting four-helix bundle. This designed peptide was optimized to prevent forming aggregates in a separate studt.[28,29] While all of the designed Fe-S cluster systems harbor a single and electronically isolated cluster, natural Fe-S clusters are exclusively organized into a network to provide an efficient electron transfer conduit. In our group, a dimeric peptide known as DSD (Domain Swapped Domain) was exploited to design two Fe-S cluster binding sites. The [4Fe-4S] cluster of *Thermotoga maritima* tryptophanyl t-RNA synthase and its primary coordination sphere was docked into DSD's hydrophobic core. Among the several positions available to match to geometry of a 4-cysteine motif, the one that provided the correct rotamers and backbone conformations was selected. The resulting DSD-2[4Fe-4S] cluster incorporated two clusters at a distance of 36 Å while maintaining its helical structure. This design was modified in a separate study by relocating the binding sites towards the center which resulted in a construct with two clusters within 12 Å apart. This study demonstrates the flexibility of DSD scaffold to incorporate more than one cluster with controlled distance.

Porphyrins

Metalloporphyrins are of fundamental significance in biology in different ways such as oxygen storage and transport. Porphyrins are used in natural metalloproteins for oxygen transport, electron transfer, NO sensing, and catalytic purposes, stemming from the ability of bound-metals to cycle between two redox states.[30] Porphyrin-containing proteins are one of the most extensively studied classes of proteins,[31] and. many studies have been performed on designing porphyrin-binding proteins for various applications

The function of heme-binding proteins can be altered by replacing the native iron with other metals such as cobalt. This approach has been further discussed in chapter 4. An alternative approach to introduce new reactivity into natural porphyrin-binding proteins is generating a second metal-binding site close to the heme. In a study performed by Lu et. al, the copper-heme binding site of cytochrome c oxidase (CcO) was mimicked within myoglobin.[32] During O_2 reduction by CcO, a tyrosine residue in the cupper binding site plays an important role by donating an electron and a proton. This feature was replicated in myoglobin by replacing Phe33 by 3-methoxy tyrosine (OMeY) via genetic code expansion and a cupper binding site was generated between three His residues and OMeY. This non-natural amino acid has more electron-donating capability than tyrosine. The designed cupper-binding myoglobin catalyzed oxygen reduction with a TON of 1100 which is twofold higher than that of the wild type. This study demonstrates that tuning the reduction potential of the binding site residues is important for improving the catalytic activity of redox enzymes.

Cytochromes are a prominent group of natural porphyrin containing proteins and they present in both eukaryotes and prokaryotes with various functions. Hydrophobic interactions hold the porphyrin into the binding site and one or two additional amino acids are employed as axial ligands to coordinate to the porphyrin. These axial ligands are of large importance in determining the apparent reduction potential of the metal center. For example in heme, the $Fe^{3+/2+}$ reduction potential decreases with more basic ligands due to their electron donating properties which stabilizes the Fe^{3+} state.[33] C-type cytochromes are ligated the central iron through axial ligands (Met and His) and two

additional covalent bonds to the cysteine residues of the protein scaffold.. Electron transfer between heme-containing proteins in nature has been tuned to create a potential gradient between them. For instance, bacterial cytochrome peroxidase reduces H_2O_2 by up taking an electron from a highly-reducing mono-heme cytochrome. Electrostatic interactions and the dielectric nature of the protein environment are two other factors that influence the reduction potential of porphyrin-binding proteins.[34]

Biofuel Production Reactions

Water oxidation and proton reduction (Scheme 1.1) are two catalyzed reactions to produce energy-rich molecules. Designing efficient catalysts for water oxidation has been the subject of remarkable interest in recent years and a wide range of molecular and non-molecular photocatalysts based on noble and Earth abundant metals have been investigated.[35–43] Interfacing designed organometallic catalysts with protein scaffolds or engineering natural metalloenzymes has been used as a viable strategy to boost the activity of such catalysts. Protein second sphere and outer sphere environment can be used a means to modulate the redox potential, fine tuning the donor/acceptor feature of the metal center, and control the ligand geometry.[44–48]

Hydrogen production has been subject for many research studies as well. Hydrogen is considered to be a key fuel of the future because it packs three times the energy of petrol or diesel, and the only waste product when it burns is water[49]. Until recently, the only way of producing hydrogen was steam reformation, where fossil fuels are heated with steam under high pressure. This is obviously not a renewable source of hydrogen and it does not reduce our reliance on fossil fuels.[50] Thermochemical H_2 production exploits a

fraction of solar energy to generate high temperature to produce H_2 from water. This approach benefits from using abundant, low cost, and non-corrosive chemicals; however, generating and maintaining high temperatures and scaling up the technology are pitfalls related to this strategy.[51] In a photoelectrochemical (PEC) approach, semiconductors coupled with catalysts are used to generate charge-separated states, and electrons and holes for water oxidation and H_2 production.

Thesis Projects

To employ metalloproteins as catalysts for electron transfer reactions, my thesis exploits natural and designed proteins in redox reactions involved in fuel production. My work has initially been focused on design and characterization of repeat proteins to incorporate multiple iron-sulfur clusters determined by the size of the scaffold. The robustness and flexibility of modular proteins renders them as ideal platforms for molecular engineering and external cofactor incorporation. This project is the subject of chapter 2.

In chapter 3, I have employed redox-active proteins known as cytochromes in water oxidation by interfacing the protein to a mesoporous semiconductor to design a photoelectrochemical cell (Figure 1.3). The strong electrostatic interactions between the proteins surface positive charges and the metal oxide negative charges on the semiconductor offers the opportunity to interface the protein with the semiconductor. On the other hand, cytochrome *c* binds to a heme cofactor which makes it redox active and suitable for electron transfer processes.

The subject of Chapter 4 is my work on hydrogen production capability of cobalt-porphyrin-binding proteins, particularly cytochromes. In this work, I have designed a whole cell bacterial display system for cobalt-cytochrome b_{562} (Co-cyt b_{562}) as a hydrogen production catalyst which can further be expanded to directed evolution studies. Employing a special strain of E. coli which is not capable of biosynthesizing heme, yet is permeable to external porphyrins, helped to express cyt b_{562} with cobalt protoporphyrin ix (Co-PPIX) in vivo.

Figures

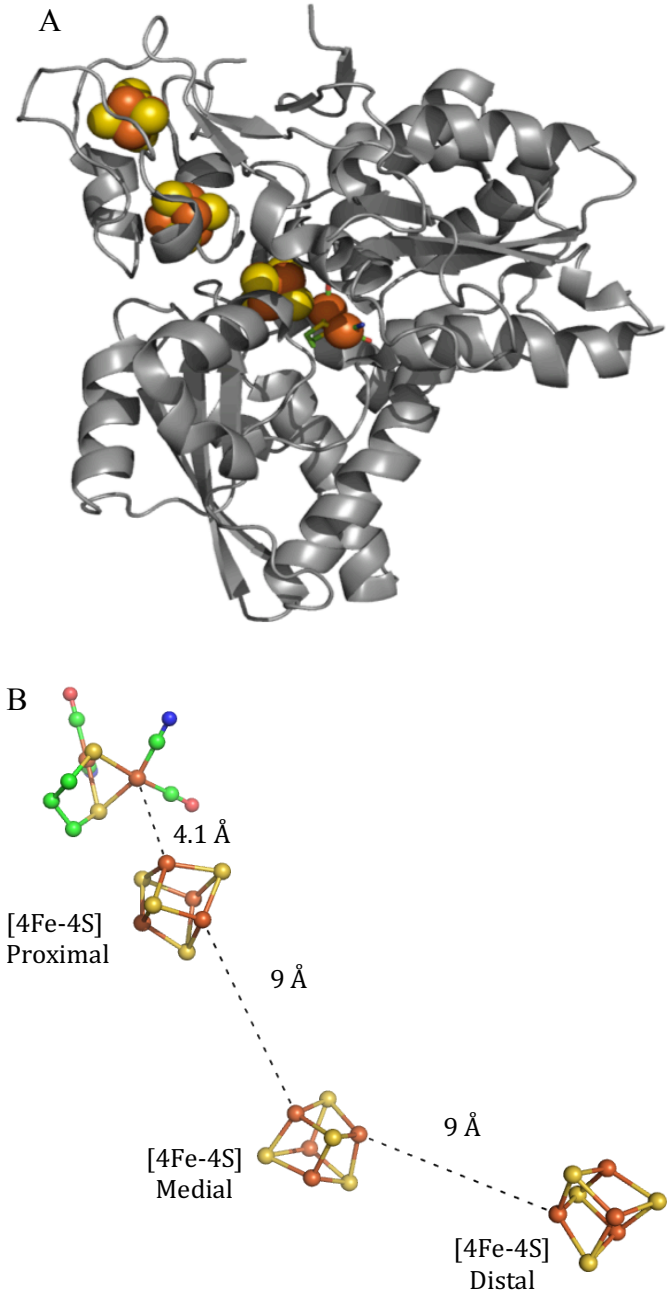

Figure 1.1. (A) Crystal structure of Fe-Fe hydrogenase, PDB 1HFE. (B) Closer look at the active site and electron transfer network of Fe-Fe hydrogenase with associated distances between each cofactor.

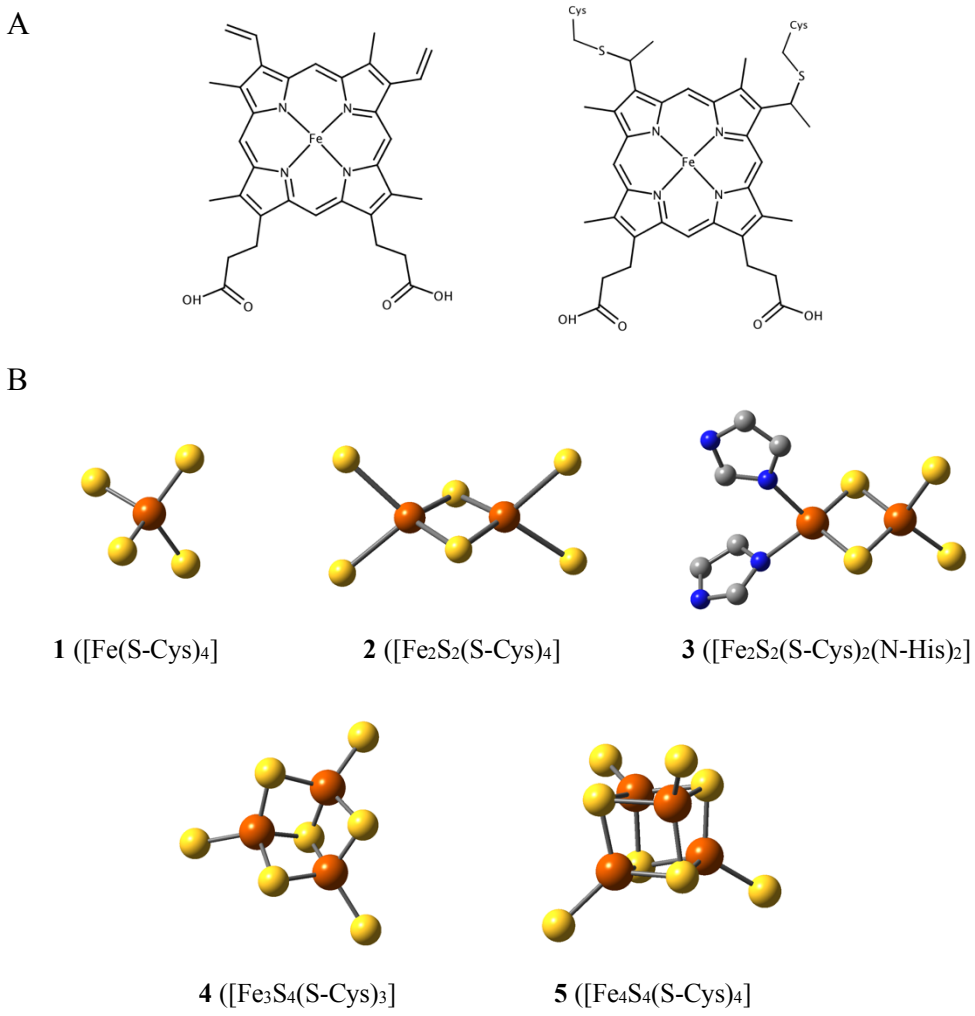

Figure 1.2. Common cofactors in metalloproteins (A) Two different types of heme, heme b (left) and heme c (right). (B) Fe-S clusters found in nature. Orange: Fe atom, yellow: S atom, gray: C atom, blue: N atom. The clusters are classified based on the number of Fe and S atoms they contain, and their names are as following: 1) Rubredoxin, 2) [2Fe-2S] cluster, 3) Rieske cluster, 4) [3Fe-4S] cluster, 5) Cubane [4Fe-4S] cluster.

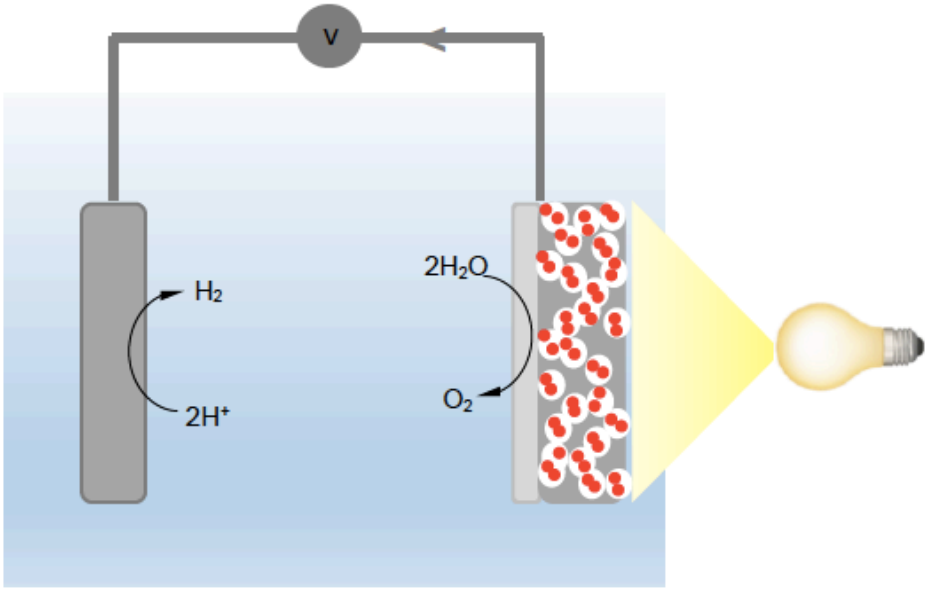

Figure 1.3. Overall scheme for photoelectrochemical water oxidation cell. The red dots represent water oxidation catalyst which is interfaced with the solid semiconductor

$2H_2O \longrightarrow O_2 + 4H^+ + 4e^-$ $\quad E = 1.23\ V - 0.059\ pH\ vs\ NHE$

$4H^+ + 4e^- \longrightarrow 2H_2$ $\quad E = 0\ V - 0.059\ pH\ vs\ NHE$

Scheme 1.1. Water oxidation and proton reduction half reactions with their associated redox potentials

CHAPTER 2

REPEAT PROTEINS AS VERSATILE SCAFFOLDS FOR ARRAYS OF REDOX-ACTIVE FE-S CLUSTERS

Reproduced from Chem. Commun., 2019, 55, 3319-3322

The work I completed for the publication was taking the data, making figures, and writing parts of introduction, materials and methods, and results.

Abstract

Arrays of one, two and four electron-transfer active [4Fe-4S] clusters were constructed on modular tetratricopeptide repeat protein scaffold, with the number of clusters determined solely by the size of the scaffold. The constructs show reversible redox activity and transient charge stabilization necessary to facilitate charge transfer.

Introduction

Molecular materials for solar energy harvesting, molecular electronics and nanoscale devices require systems capable of facilitating long-range electron transfer (ET) with high quantum yield.[1,53] As the biological ET becomes better understood, nature-inspired ET systems are emerging as alternatives to purely synthetic designs. In nature, medium and long-distance electron transfer is often performed by arrays of cofactors held at specific distances within complex proteins[54–56]. Fe-S clusters are one of the most common cofactors utilized for this purpose. They are implicated in fundamental biological processes, with an array of functions ranging from electron transfer to catalysis, iron level regulation and storage, as well as transport of ligands within the cell. Remarkably, they are often used in multielectron redox processes, most prominently proton reduction, sulfite reduction, and elemental nitrogen reduction. The chemical properties of iron–sulfur proteins, such as their low redox potential and high oxygen sensitivity, their prevalence, structural flexibility, and functional versatility, suggest that they emerged early in evolution. They are thought to have evolved in a pre-photosynthetic world by incorporation of inorganic precursors found in the highly reducing, iron and sulfur-rich environment into

primitive peptide sequences.[57,58]

The cubane-type [4Fe–4S] cluster is the most abundant and versatile type of Fe–S clusters. The [4Fe-4S] clusters are composed of four iron atoms, each coordinated by three inorganic sulfurs and one cysteine residue; positioning the cluster within the hydrophobic core of the protein is achieved by anchoring through four cysteines that can be part of a number of secondary structure motives.[59] Clusters are found either isolated, in pairs, or arranged in multicluster chains within protein structure ranging from small and water soluble, such as the ferredoxins, to large multiprotein complexes, such as hydrogenases, nitrogenases, and photosystem II.[60] The wide range of redox potentials exhibited by proteins containing [4Fe–4S] clusters points to the role of secondary shell and long range interactions in modulating their intrinsic reactivity: iron–sulfur proteins exhibit redox potentials ranging from -700 to 450mV. These properties have spurred intensive investigations of natural cluster-binding proteins, leading to elucidating several distinctive features. For example, this range of potential is achieved in part by accessing three different redox states: $[4Fe–4S]^{+3/+2/+1}$. In bacterial ferredoxins the $[4Fe–4S]^{2+}/[4Fe–4S]^{1+}$ transition can occur near -600mV, while in high potential iron–sulfur proteins (HiPIPs) redox potentials near +500mV have been measured for the $[4Fe–4S]^{3+}/[4Fe–4S]^{2+}$ couple. The similarities in structure and geometry of the clusters embedded in ferredoxins and HiPIPs suggest that such large differences in redox potential are due to the surrounding protein environment.[61]

Building on the information gleaned on natural proteins, our group and others have designed model proteins, with the dual purpose of further unmasking relationships

between sequence and structural motifs on one side, and function on the other, as well as generating proteins tailored to specific applications. The rational design of metal-binding sites is well established in the literature.[62–70]

One of the approaches for the de novo design of [4Fe–4S] proteins uses both rational and computational strategies: rather than replicating natural sequence motifs, the examples described later start from the geometric requirements of a disembodied cluster that is, a cluster and the four cysteines that form the first coordination sphere and search for protein scaffolds that are compatible with the geometry. The protein structure is then carved out to accommodate the cluster.

Grzyb et al. further extended this approach by designing a four-helix bundle around a disembodied [4Fe–4S] cluster, rather than relying on the PDB as a source of protein scaffolds. Starting with an analysis of bound clusters within protein structures, they focused on the binding motif of tryptophanyl-tRNA synthase (PDB 2G36) and discovered that the cluster, including the cysteine ligands and [4Fe–4S] atoms, had inherent tetrahedral symmetry. The first coordination sphere could be described as two CXXC motives within a helical structure and related by C_2 symmetry. The CXXC motifs were extended into two parallel helices, and the structure of the four-helix bundle was finalized using protCAD to build the backbone of two additional helices and the loops connecting them. Finally, the best sequence for the backbone structure was selected using protCAD for core residues, and Rosetta for surface exposed amino acids. The resulting protein was experimentally characterized. UV–CD analysis upon [4Fe–4S] cluster incorporation showed an increase in alpha-helical structure compared to the apoprotein,

indicating higher stability.[68] The metal-first approach used here introduced an alternative method for [4Fe–4S] protein design, described in detail in a recent review.[71]

Most synthetic models aimed towards engineering of functional redox enzymes have been designed to bind a single electronically isolated cluster in the protein scaffold or in the proximity of a catalytically active cofactor. [67,72,73] Recently, the first examples of two [4Fe-4S] clusters incorporated at design-determined distances in the hydrophobic core of a three-helix bundle have been reported.[74,75] However, designing multi-center Fe-S proteins remains a challenge.

Modular assembly of multi-center ET-active systems based on repeat proteins was identified as a viable strategy. The structural simplicity and intrinsic modularity of the repeat proteins allow to use them as simple units for bottom-up fabrication, where each repeat unit can be used as a building block with individually engineered properties and functionalities[76,77]. Consensus tetratricopeptide repeat (CTPR) protein, composed of helix-turn-helix motifs that connect in a sequence to form a right-handed super helical structure,[78] possesses the robustness and stability needed to support supramolecular assemblies[79–81]or act as support structures in solution and solid state.[82–84] In the current work, a four-sulfur coordination site was ′grafted′ onto CTPR protein scaffold, forming arrays of functional ET-active [Fe-S] clusters with precisely defined distance and orientation. The system establishes a foundation for the modular design of long-range ET conduits. To the best of our knowledge, this is the first example of a single scaffold used to assemble a controlled number of clusters.

Materials and Methods

Protein design and purification:

Mutations were introduced in CTPR1 units to generate two mutated repeats C1 (Y5C and N9C) and C2 (E2C and N6C) by quick-change site directed mutagenesis. The two mutated CTPR1 units C1 and C2 were then fused to create the CTPR2_4cys gene by sequential cloning of C1 and C2 into pPro-EXHTa vector (sequence in Figure 2.1). CTPR4_8cys and CTPR8_16cys genes were generated by sequential additions of two and four copies of the CTPR2_4cys gene into pPro-EXHTa vector.

The proteins were expressed in *E. coli* C41 strain with an *N*-terminal His-tag and purified using Ni-NTA affinity chromatography based on previously published protocols for His-tagged CTPR proteins, using 0.5 M urea in the lysis buffer to improve protein solubility. The proteins were then dialyzed against PBS buffer (150 mM NaCl, 50 mM phosphate, pH 7.4). Protein concentration was determined using absorbance at 280 nm with the extinction coefficient calculated from the amino acid sequence of each protein (32110 M^{-1} cm^{-1} for CTPR2_4cys, 59750 M^{-1} cm^{-1} for CTPR4_8cys and 115030 M^{-1} cm^{-1} for CTPR8_16cys). TEV protease in PBS buffer with 1 mM DTT and 0.5 mM EDTA was added to remove the His-tag in a 1:20 TEV: CTPR protein molar ratio and incubated at 4 °C overnight. His-tagged TEV protease was removed using Ni-NTA affinity chromatography, in which CTPR proteins without His-tag were collected in the flow-through, while the His-tag and the tagged TEV protease remained bound to the affinity resin. CTPR proteins were dialyzed against 100 mM Tris-HCl pH 8.5 buffer and stored at -20 °C.

Incorporation of [4Fe-4S] clusters into CTPR proteins:

Iron−sulfur clusters were incorporated into the designed proteins by adapting a previously established protocol. All reactions were performed in an anaerobic chamber (Coy Scientific) under 95% N_2 and 5% H_2 atmosphere. To a 50 μM CTPR protein solution in 100 mM Tris-HCl, pH 8.5 was added β-mercaptoethanol to a final concentration of 0.8% (v/v) (total reaction volume of 2.5 ml), and the solution was incubated for 20 min. Freshly prepared solution of ferric chloride ($FeCl_3$) was then added dropwise to a final concentration of 3 mM. After additional 20 min, freshly prepared solution of sodium sulfide (Na_2S) was added to a final concentration of 3 mM. The dark brown solution was incubated overnight at room temperature and was then desalted using PD-10 column (GE Healthcare) pre-equilibrated with 100 mM Tris at pH 7.5, to remove all non-protein low molecular mass contaminants and salts. The protein-cluster fractions were then collected for further characterization.

Cluster identification and quantification:

UV−vis spectra were acquired using a Perkin-Elmer Lambda-35 spectrophotometer under anaerobic conditions. The absorption spectra from 230 nm to 800 nm were acquired in a 1 cm path-length quartz cuvette using a 4 nm slit-width. The spectra of the CTPR-$[4Fe\text{-}4S]^{2+}$ proteins were acquired directly from desalted samples. Freshly prepared sodium dithionite was added to a final concentration of 1mM to reduce the clusters.

To assess the cluster incorporation quantitatively, iron and protein concentrations were measured separately in each sample. Iron concentration was determined using the

ferrozine assay, and protein concentration was quantified using Bradford assay for CTPR2-[4Fe-4S], CTPR4-2[4Fe-4S] and CTPR8-4[4Fe-4S] proteins. The proteins were denatured at 95 °C for 15 min prior to the Bradford assay to ensure that the Bradford reagent interacts effectively with the proteins. The relative iron/protein concentrations were then calculated.

Circular dichroism (CD) spectroscopy:

CD characterization of apo proteins and of CTPR2-[4Fe-4S], CTPR4-2[4Fe-4S] and CTPR8-4[4Fe-4S] complexes in 10 mM Tris-HCl buffer pH 7.5 was performed with a JASCO J- 815 spectropolarimeter, using a quartz cuvette with a path length of 0.1 cm. CD spectra were recorded from 260 to 190 nm in 1 nm increments. Thermal denaturation curves were monitored by following the CD signal at 222 nm as a function of temperature from 10 °C to 95 °C. The measurements were taken in an airtight cuvette to exclude air during the course of the experiment. CD spectra of apo proteins were recorded in the presence of excess tris(2-carboxyethyl) phosphine (TCEP) to maintain the cysteine side chains in a reduced state. Molar residue ellipticity (MRE) was calculated using cuvette path length in centimeters, and the number of amino acids of 73, 141 and 277 for CTPR2, CTPR4 and CTPR8, respectively.

Electron paramagnetic resonance (EPR) spectroscopy:

Protein-cluster fractions eluted from PD-10 column were concentrated using ultrafiltration centrifugal tubes with a molecular weight cut-off of 3000 Da (GE Healthcare) to approximately 1 mM. The samples were reduced with 100 mM sodium dithionite in 1 M glycine buffer at pH 10.0 to a final concentration of 20 mM sodium

dithionite. 10% (v/v) glycerol was then added as cryoprotectant and the samples were flash-frozen in quartz EPR tubes in liquid N_2. EPR experiments were carried out at the EPR facility of the University of Arizona, on an X-band EPR spectrometer Elexsys E500 (Bruker) equipped with a standard TE_{102} resonator and an ESR900 flow cryostat (Oxford Instruments). The measurements were performed at 15 K with microwave (mw) frequency 9.335 GHz, mw power 2 mW and magnetic field modulation amplitude 0.5 mT. The numerical simulations of the EPR spectra were performed using the SimBud software available at https://cbc.arizona.edu/research/support-services/facilities/electron-paramagnetic-resonance-epr-facility/software. For the simulated spectra of CTPR2-[4Fe-4S], CTPR4-2[4Fe-4S] and CTPR8-4[4Fe-4S], the principal g-values (g_1, g_2, g_3) = (1.878, 1.927, 2.060), (1.878, 1.927, 2.06), (1.883, 1.927, 2.057) and the corresponding intrinsic linewidths of (8, 5, 4.5), (8, 5.5, 5) and (8, 4.7, 4.5) mT were used.

Cyclic voltammetry (CV):

Electrochemical experiments were performed on a CH Instruments 1242B potentiostat in an oxygen free glovebox using a three-electrode configuration. A glassy carbon (3 mm diameter 0.28 cm^2 surface area) working electrode, a platinum mesh counter electrode, and a Saturated Calomel Electrode (SCE) reference electrode was used for cyclic voltammetry. Working electrode was cleaned by sequential polishing with 1 μm, 0.05 μm, and 0.03 μm alumina. Cyclic voltammetry measurements were taken using 10 μM of the proteins in 100 mM Tris, 100 mM NaCl pH 7.5 electrolyte with the scan rate of 100 mV/s. Square wave voltammetry measurements were taken in the same electrolyte

as CVs, with the increment potential of 0.004 V and square wave frequency of 20 Hz. The data collected shown without further processing or background subtraction.

Transient absorption spectroscopy:

Transient absorption spectra and kinetics were obtained using HELIOS Fire spectrometer (Ultrafast Systems). Excitation at 400 nm was from an optical parametric amplifier (Spectra Physics) pumped with laser pulses of 100 fs at 800 nm generated by an amplified, mode-locked titanium sapphire laser system (Millennia/Tsunami/Spitfire, Spectra Physics) operating at 1kHz repetition rate. The angle between the polarization of the excitation and probe pulses was set at 54.7° (magic angle) with respect to each other to eliminate anisotropic effects associated with rotational dynamics. The instrument response function was *ca*. 200 fs. The protein samples were dissolved in 100 mM Tris pH 7.5 and were loaded into the 5 mm path length tightly capped quartz cuvette (Spectrocell Inc.) inside a glovebox under nitrogen atmosphere. Solutions were stirred during the measurement using a Teflon coated stir bar to avoid excessive exposure of the samples to multiple laser shots.

Data analysis:

Data analysis was carried out using locally written software (ASUFIT) within a MATLAB environment (Mathworks Inc.). Decay-associated spectra were obtained by fitting the transient absorption change curves over a selected wavelength region simultaneously as described by the equation below (parallel kinetic model),

$$\Delta A(\lambda, t) = \sum_{i=1}^{n} A_i(\lambda) \exp(-t/\tau_i) \qquad \text{Equation 2.1}$$

where $\Delta A(\lambda,t)$ is the observed absorption change at a given wavelength at time delay t and n is the number of kinetic components used in the fitting. A plot of $A_i(\lambda)$ versus wavelength is called a decay-associated spectrum (DAS), and represents the amplitude spectrum of the i^{th} kinetic component, which has a lifetime of τ_i. Kinetics at early decay times (<500 fs) were obscured by the strong CPM artifacts and stimulated Raman signal of water therefore it was difficult to extract useful information about the shortest-lived species if any from the data.

Evolution-associated difference spectra (EADS) were obtained by global analysis of the transient absorption data using a kinetic model consisting of sequentially interconverting species, e.g. 1→ 2→3→…n. The arrows indicate successive mono-exponential decays with increasing time constants, which can be regarded as the lifetimes of each species. Associated with each species is a lifetime and a difference spectrum. Each EADS corresponds in general to a mixture of states and does not portray the spectrum of a pure state or species. This procedure enables us to visualize clearly the evolution of the transient states of the system. The global analysis procedures described here were adapted from literature methods.[49] Random errors associated with the reported lifetimes obtained from transient absorption measurements were typically ≤ 5%.

Results and Discussion

Based on the crystal structure of tryptophanyl-tRNA synthethase (PDB ID: 2G36) and on a previous design of a [4Fe-4S] cluster-coordinating peptide[74,75], a four-cysteine [4Fe-4S] coordination site was modeled at the interface of two adjacent CTPR repeats (PDB: 2HYZ), on the concave surface of CTPR superhelix. Of the several possible

positions for the cysteines, the design that supported the correct distances and rotamers for the four coordinating cysteines, Y5C and N9C in the first repeat and E2C and N6C in the second repeat, was selected. A [4Fe-4S] cluster was then manually docked into the designed binding pocket using PyMOL software and the resulting model was subjected to three rounds of energy minimization using GROMACS. The side chain conformations and backbone geometry of the designed cysteines were compatible with the TPR helical fold and with the cluster coordination distances observed in natural coordination sites. The two-repeat cluster-forming unit was sequentially aligned with consecutive sections of an eight-repeat model to provide models of two- and four- cluster assemblies. The optimized models showed no global structural deviations from the crystal structure of CTPR proteins. Based on the models, the clusters in the multi-cluster constructs are about 17 Å apart (Figure 2.2).

Cubane-type [4Fe-4S] clusters within the proteins were formed using an established *in situ* synthetic procedure from iron (III) chloride and sodium sulfide under anaerobic conditions.[85] The UV-Vis spectra of the resulting CTPR2-[4Fe-4S], CTPR4-2[4Fe-4S] CTPR8-4[4Fe-4S] proteins (Figure 2.3) showed broad absorption peaks at 345, 430, and 630 nm characteristic of charge transfer excitations from sulfur to iron in $[4Fe\text{-}4S]^{2+}$ clusters[86], but red-shifted compared with inorganic [4Fe-4S] clusters due to the hydrophobic environment of the protein[73,87,]. The absorption at 430 nm disappeared upon reduction of the clusters to $[4Fe\text{-}4S]^{+}$ state with sodium dithionite, as expected for cuboidal [4Fe-4S] clusters.[88–90]

Table 2.1 Quantification of iron content in designed proteins using ferrozine method.

Construct	Fe atoms/protein chain
CTPR2-[4Fe-4S]	4.60 ± 0.38
CTPR4-2[4Fe-4S]	7.62 ± 0.22
CTPR8-4[4Fe-4S]	16.44 ± 1.33

Iron content (measured using the ferrozine method[91]) in the protein complexes (determined using Bradford assay[92,93]) was in agreement with a single [4Fe-4S] clusters forming in a binding cavity (Table 1): one cluster in CTPR2 scaffold, two clusters in CTPR4 and four clusters in CTPR8. Circular dichroism (CD) analysis showed the CTPR proteins retained α-helical structure in all three complexes, indicating that the incorporation of the [4Fe-4S] clusters did not affect the structure of the protein scaffolds (Figure 2.4). To the contrary, thermal denaturation analysis showed that cluster formation increased global stability of the proteins, with the effect most pronounced for the 2-repeat protein, which cannot benefit from the stabilizing effect of the extended superhelical structure due to its size (Figure 2.5). The T_m values for CTPR2, CTPR4 and CTPR8 were 55 °C, 68 °C, and 75 °C, respectively, while the respective T_m values for CTPR2-[4Fe-4S], CTPR4-2[4Fe-4S] and CTPR8-4[4Fe-4S] were 65 °C, 73 °C and 75 °C. This stabilizing effect, arising from a rigid [4Fe-4S] cluster holding protein helical fragments in place, is in line with previous results. [74,75]

Electron paramagnetic resonance (EPR) spectroscopy confirmed the iron-sulfur clusters initially formed in an EPR-silent $[4Fe\text{-}4S]^{2+}$ resting state. The lack of signal further confirmed cluster identity, ruling out other possible clusters (e.g. [3Fe-4S]) that are EPR active in their resting state. Reduction with sodium dithionite yields the EPR active $[4Fe\text{-}4S]^{1+}$ state: all three constructs display nearly identical spectra with principal *g*-values of 1.88, 1.93, and 2.06 (Figure 2.6), typical of $[4Fe\text{-}4S]^{1+}$ clusters.[16] Features indicative of exchange and/or magnetic dipole interactions between the clusters, observed with natural ferredoxins containing two $[4Fe\text{-}4S]^{1+}$ clusters at 10−15 Å from each other[94], were not detected for CTPR4-2[4Fe-4S] and CTPR8-4[4Fe-4S] constructs, suggesting lack of interactions between the clusters.

Square wave voltammetry was used to assess the redox potential of the clusters. Electrochemically quasi-reversible signals were observed for all three CTPR-[4Fe-4S] proteins, with redox potentials of -0.21 V, -0.24 V and -0.24 V *vs* SCE for CTPR2-[4Fe-4S], CTPR4-2[4Fe-4S], and CTPR8-4[4Fe-4S], respectively (Figure 2.7), and peak to peak separation of about 250 mV, indicative of moderate electron transfer rate between the electrode and proteins[95]. These values fall within the range expected for the relatively solvent exposed low-potential [4Fe-4S] clusters[86,87,96]. The similar behavior of the three constructs suggests the clusters react mostly independently, with little interaction between neighboring clusters within the larger assemblies. At constant protein concentration, current intensity is proportional to the number of clusters in the constructs, as expected (Figure 2.8). However, the larger constructs showed increasingly more negative redox potentials, despite identical environment around the clusters. This trend could be attributed

to the difficulty of successive cluster reduction after a first cluster in a construct has been reduced, thus suggesting at least some degree of interaction between the clusters. Transient absorption spectroscopy was employed to investigate charge transfer pathways of the clusters. Laser pulses of ~100 fs at 400 nm were used to promote ligand to metal charge transfer (LMCT) transitions from the sulfur to the iron atoms (Figure 2.9).[97] Global analysis of the transient absorption data yielded three evolution-associated-difference spectra (EADS).[98] EADS from all three proteins have similar features and the TA was satisfactorily fitted with almost identical lifetimes (Figure 2.10), indicating at least 3 transient states (species) involved in the photo induced charge transfer process, but no direct electron transfer between the [4Fe-4S] clusters in the protein. However, the EADS showed that the 400 nm laser pump induces an internal reduction of the [4Fe-4S] cluster, and the surrounding protein is capable of stabilizing that state *via* long-range redox reaction to its outside, creating long lived (about 7 ns) charge separated state. As such, the EADS corresponding to the species with ~0.4 ps lifetime shows broad ground state bleaching (GSB) with maxima below 460 nm and around 600 nm, characteristic of the S (3p) → Fe (3d) LMCT excited state[97] that, due to the short lifetime, is attributed to the transient internal electron transfer (ET) from a bridging sulfide (ET pathway 1, Figure 2.11). Similarly, the ~ 6 ps EADS shows GSB maxima below 460 nm and around 650 nm. In this case, due to the longer lifetime, the most probable path involves a cysteinyl sulfur transferring an electron to the iron in the 4Fe-4S cluster (ET pathway 2, Figure 2.11), thus generating an electron hole in the cysteine. Interestingly, this state decays in part by forming a transient state with about 7.5 ns lifetime and characteristic bleaching of tyrosyl

or tryptophanyl radical around 510 nm.[99] This suggest the electron hole in the cysteine is most likely quenched by proton coupled electron transfer (PCET) promoted by the linked tryptophan where the electron acceptor is the cysteine hole and proton acceptor is possibly the water (path 3, Figure 2.11).[100] Cysteine-linked tyrosine might be involved in this PCET as well, but shorter distance (less connecting bonds between chromophores) and bigger driving force for the electron transfer would probably favor the tryptophan.

This study demonstrates the application of CTPR proteins as a scaffold for [4Fe-4S] clusters, enabling to coordinate a desired number of redox active clusters within a single protein, with the cluster count controlled solely through the number of CTPR repeats in the sequence. The repeat nature of the protein scaffold also imposed a consistent distance of about 1.6 nm between the clusters in multi-cluster assemblies. The designed proteins coordinate the clusters with the expected stoichiometry, with one cluster per engineered binding site, and with spectral characteristics similar to those observed in natural ferredoxins. The CTPR-[4Fe-4S] complexes remain well folded, with the characteristic helical structure of the TPR domain. The EPR spectra of the reduced protein-cluster complexes corresponded to the $[4Fe\text{-}4S]^{1+}$ state. Square wave voltammetry confirmed that the [4Fe-4S] clusters coordinated by the designed proteins are redox active and have redox potentials within the range of low-potential protein-clusters. Transient absorption spectroscopy showed that the clusters form long-lived charge-separated states stabilized by the protein matrix, as observed in proteins involved in long range energy transfer.

Direct interaction between the [4Fe-4S] clusters was not observed, but instead the excitation pathway was traced to the surface of the protein. This work demonstrates

potential application of CTPR-[4Fe-4S] proteins to organize multiple cofactors, establishing the foundation for the modular design of long-range ET conduits and serves to further demonstrate the versatility of CTPR proteins as a platform for designing functional materials or assemblies with order maintained at a molecular level. CTPR proteins have proven to be robust scaffolds for complex multifunctional systems, which include diverse functional elements. The stabilization of redox active clusters brings the possibility of combining photo- and redox-active elements at controlled distances and orientations for full-fledged energy transfer conduits. As such, CTPR proteins show virtually unmatched potential as a protein scaffold for nanotechnological systems, including potential artificial photosystems.

Figures:

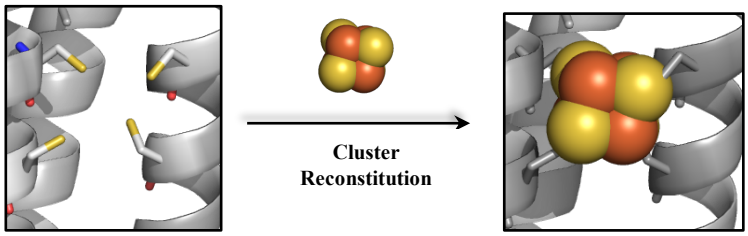

CTPR	GAMGSAEAWYNLGNAYYKQGDYDEAIEYYQKALELDPRS
	AEAWYNLGNAYYKQGDYDEAIEYYQKALELDPRS
CTPR2-[4Fe-4S]	GAMGSAEAWCNLGCAYYKQGDYDEAIEYYQKALELDPRS
	ACAWYCLGNAYYKQGDYDEAIEYYQKALELDPRS

Figure 2.1. Design strategy for incorporation of [4Fe-4S] clusters into CTPR proteins. Top: structural model of the 4-Cys cluster binding site (left) and the CTPR-[4Fe-4S] protein (right). Bottom: sequence of wild type CTPR protein and modified CTPR protein to incorporate the clusters; mutated residues are Y5C and N9C in the first repeat and E2C and N6C in the second repeat, which are highlighted in red.

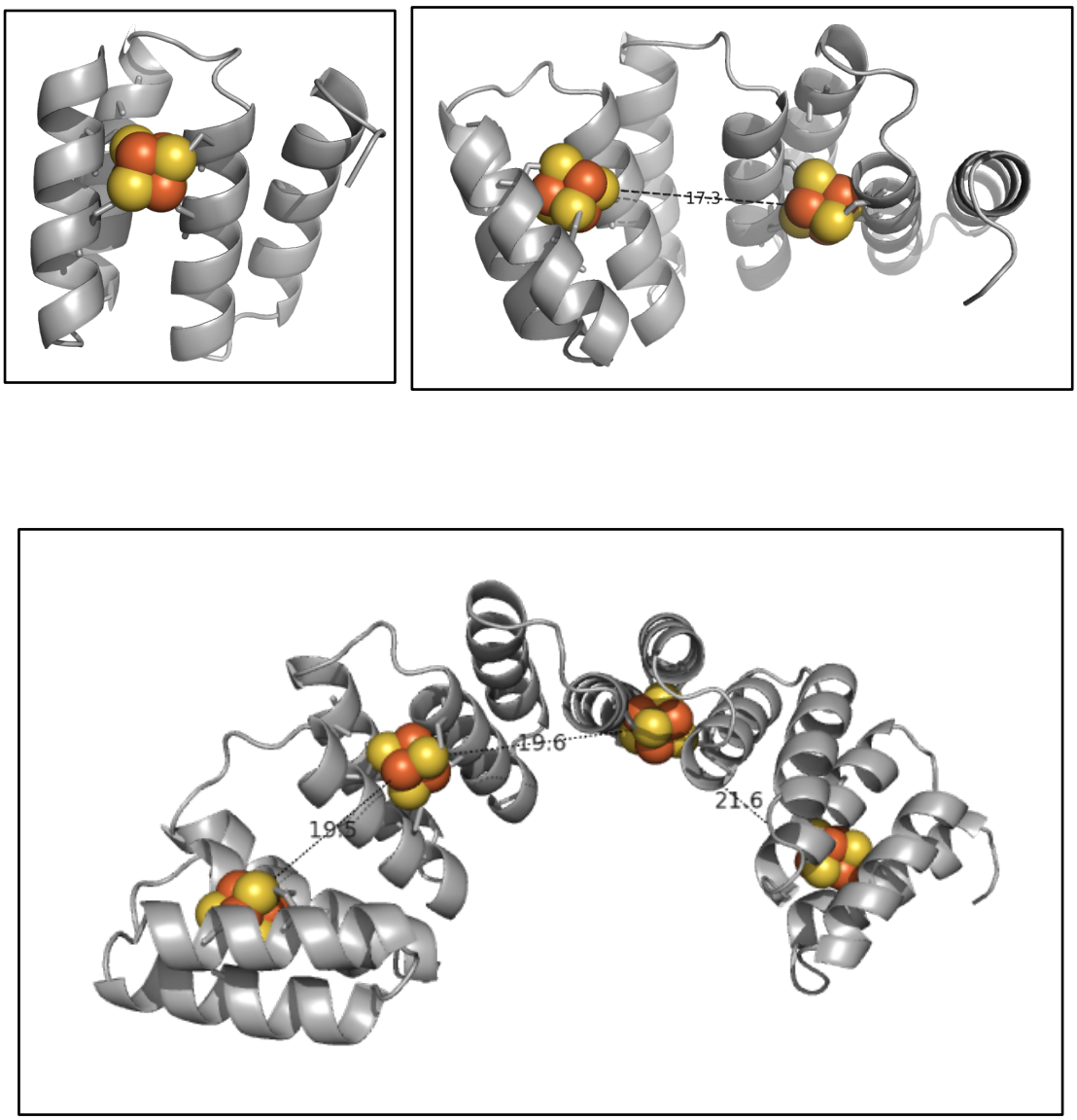

Figure 2.2. Model of designed [4Fe-4S] cluster-binding proteins. Top left: CTPR2-[4Fe-4S], top right: CTPR4-2[4Fe-4S], bottom: CTPR8-4[4Fe-4S] models. Cluster distances are shown in Angstroms.

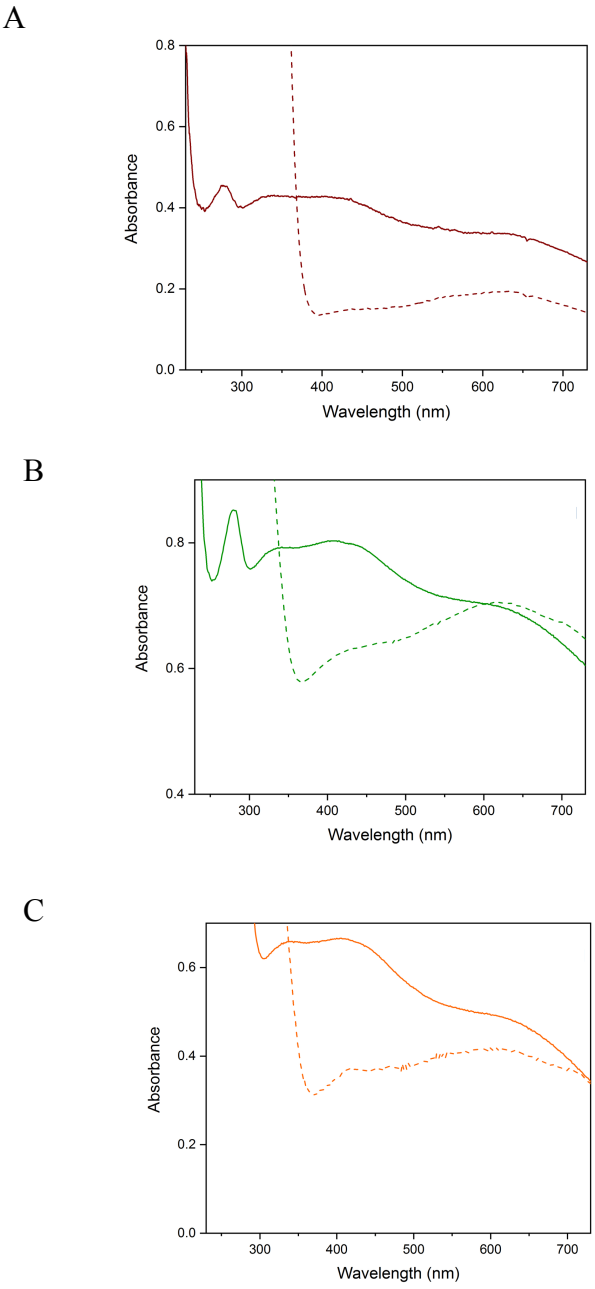

Figure 2.3. UV-Vis characterization of CTPR-[4Fe-4S] proteins. UV-Vis spectra of (A) CTPR2-[4Fe-4S], (B) CTPR4-2[4Fe-4S], (C) CTPR8-4[4Fe-4S]. Solid red, green, and orange lines indicate holo CTPR2, CTPR4, and CTPR8 proteins respectively. Dashed lines indicate dithionite reduced proteins.

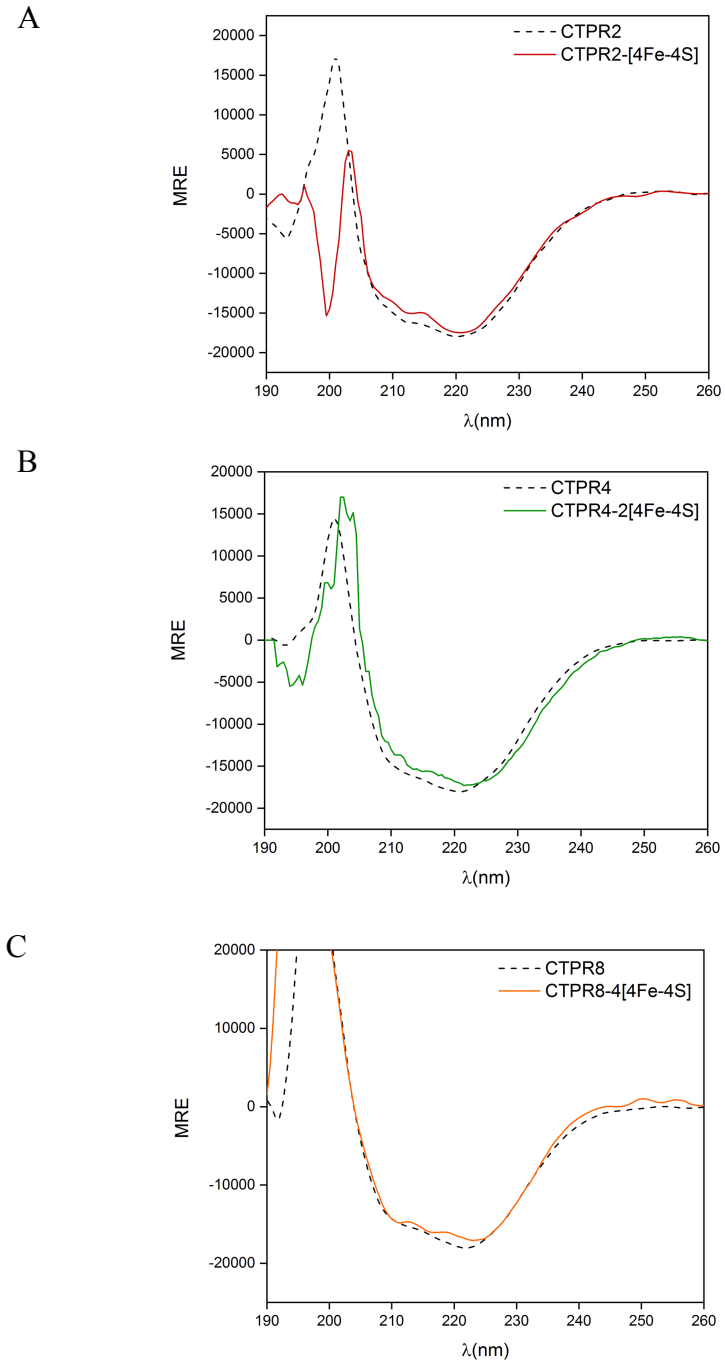

Figure 2.4. CD characterization of CTPR-[4Fe-4S] proteins. CD spectra of (A) CTPR2-[4Fe-4S], (B) CTPR4-2[4Fe-4S], CTPR8-4[4Fe-4S]. Solid red, green, and orange lines indicate holo CTPR2, CTPR4, and CTPR8 proteins respectively. Dashed lines indicate apo proteins.

A

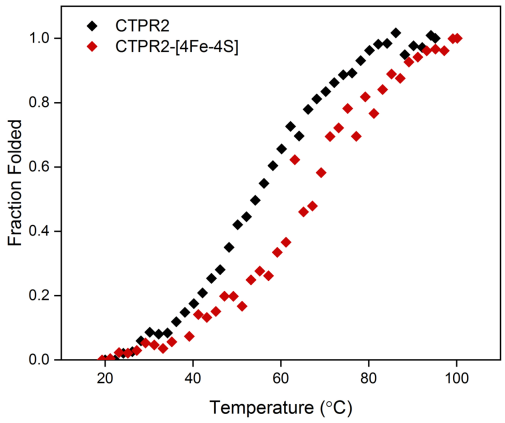

B

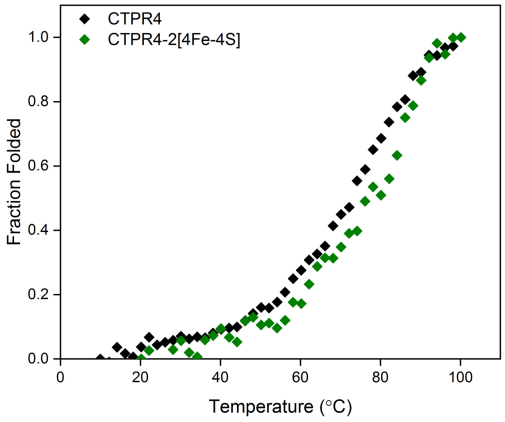

C

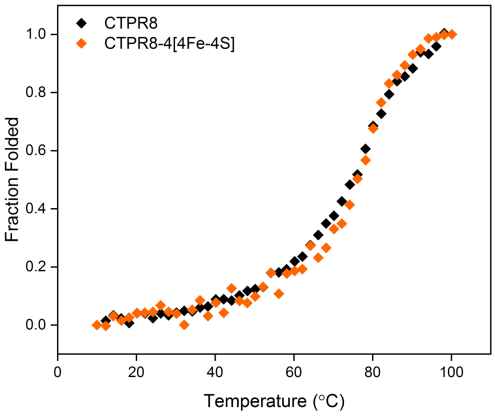

Figure 2.5. Stability analysis of CTPR-[4Fe-4S] proteins**.** Thermal denaturation of (A) CTPR2-[4Fe-4S] (A) CTPR4-2[4Fe-4S] (A) CTPR8-4[4Fe-4S] in red, green, and orange squares respectively. Black squares indicate corresponding apo proteins. CD signal was measured at 222nm while the temperature was increased from 4°C to 96°C.

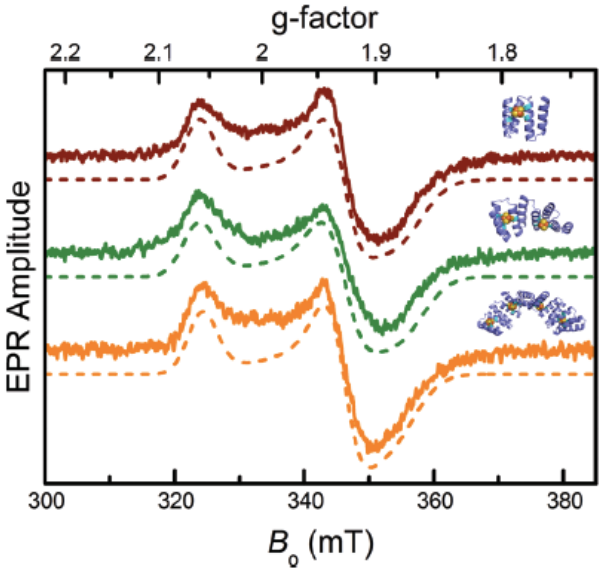

Figure 2.6. EPR characterization of the CTPR-bound [4Fe–4S] clusters. From top to bottom: EPR spectra of sodium dithionite-reduced CTPR2-[4Fe–4S] (red), CTPR4-2[4Fe–4S] (green) and CTPR8-4[4Fe–4S] (orange) proteins and numerically simulated EPR spectra (dashed lines)

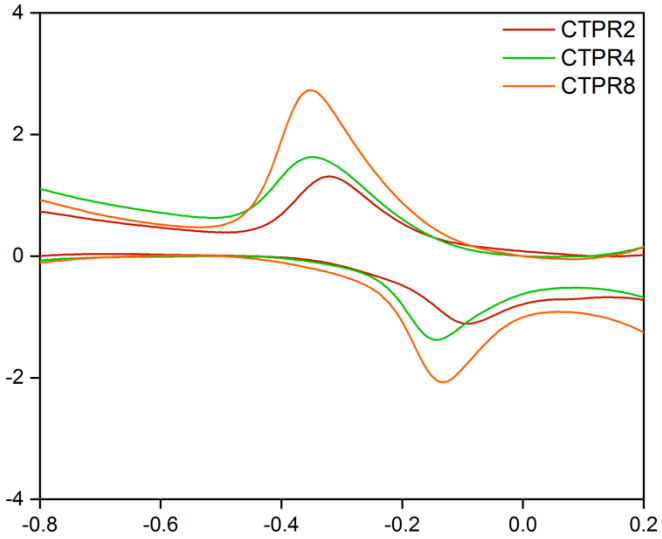

Figure 2.7. Square wave voltammetry of the CTPR-[4Fe-4S] cluster proteins. Voltammograms of CTPR2-[4Fe-4S], CTPR4-2[4Fe-4S], CTPR8-4[4Fe-4S] are shown in red, green, and orange, respectively.

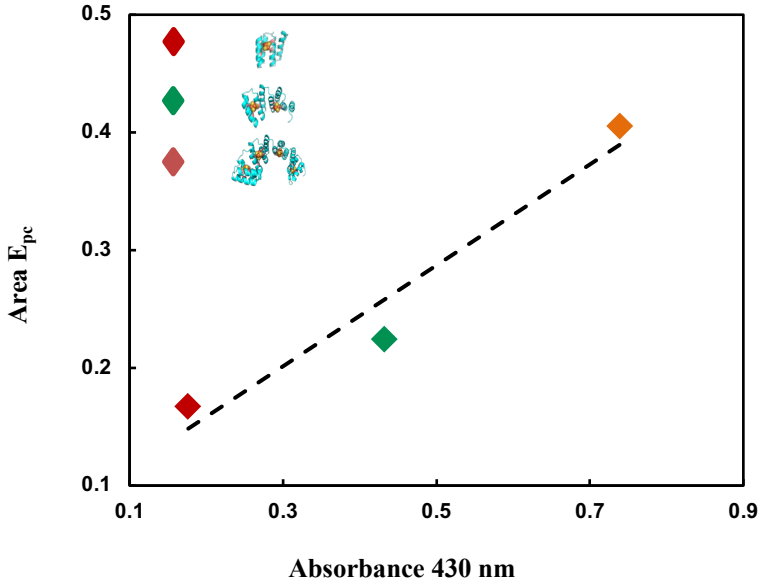

Figure 2.8. Dependence of redox current on [4Fe-4S] cluster population. The area of the E_{pc} peak from the square cyclic voltammogram (Figure 2.7) against sample absorbance at 430 nm. CTPR2-[4Fe-4S] in red, CTPR4-2[4Fe-4S] in green and CTPR8-4[4Fe-4S] orange. As absorbance at 430 nm depends on cluster concentration, the trend implies a linear relationship between redox current and cluster population.

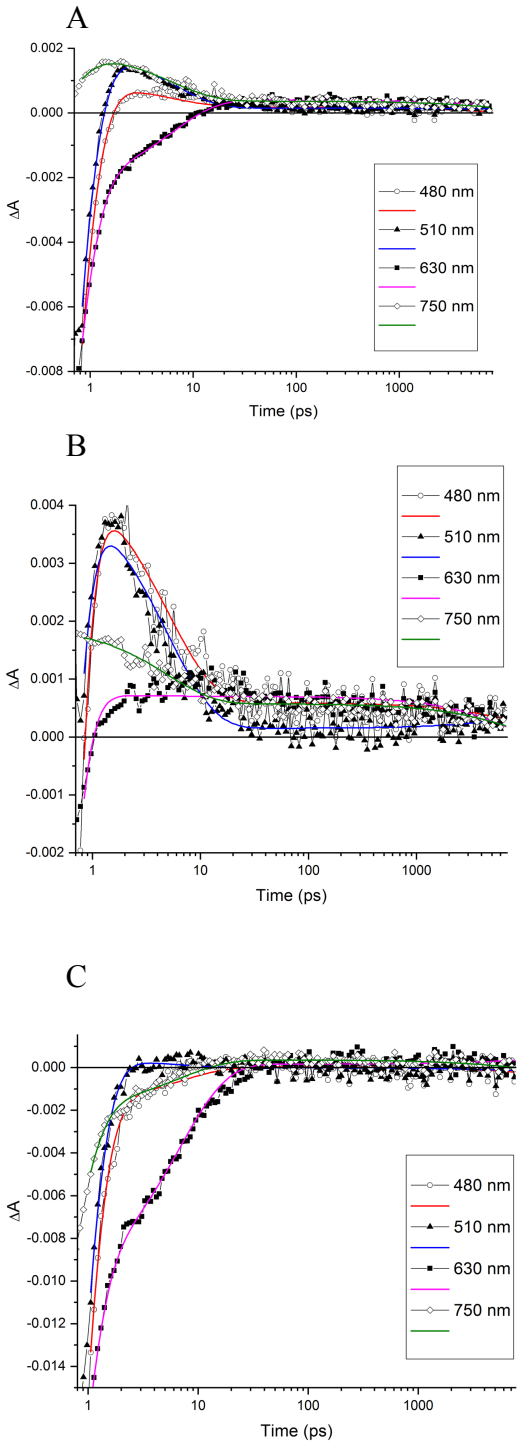

Figure 2.9. Transient absorption kinetics. From top to bottom, transient absorption kinetics of CTPR2-[4Fe-4S] (A), CTPR4-2[4Fe-4S] (B) and CTPR8-4[4Fe-4S] (C) at different wavelengths after excitation at 400 nm.

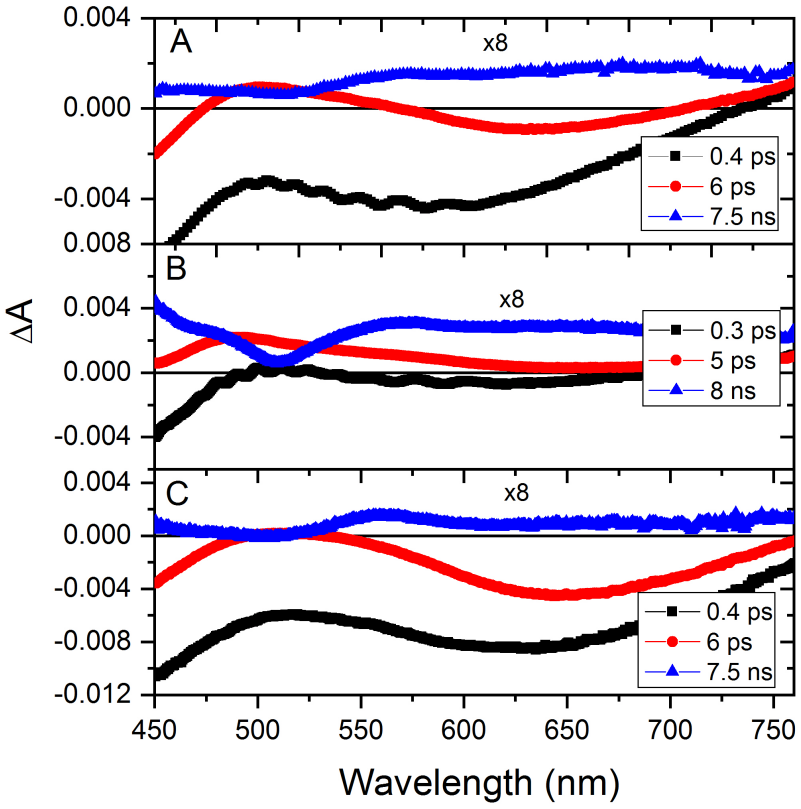

Figure 2.10. EADS for the CTPR-[4Fe–4S] proteins from the global fit of TA data with three lifetimes: (A) CTPR2-[4Fe-4S], (B) CTPR4-2[4Fe-4S], and (C) CTPR8-4[4Fe-4S], at three lifetimes corresponding to 0.4 ps (black), 6 ps (red) and 7.5 ns (blue). The 7.5 ns EADS is magnified by a factor of 8 for better visibility.

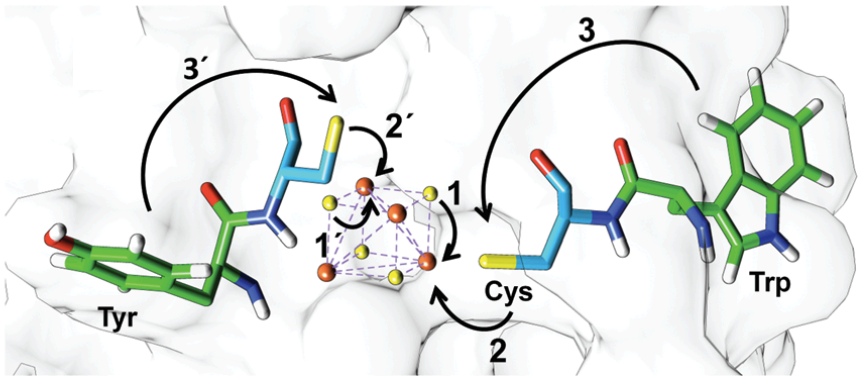

Figure 2.11. Proposed electron transfer pathways between [4Fe-4S] clusters and their adjacent amino acids. Arrows show the direction of the electron transfer.

CHAPTER 3

PHOTOELECTROCHEMICAL WATER OXIDATION BY COBALT CYTOCHROME C INTEGRATED-ATO PHOTOANODE

Abstract

Co-PPIX-substituted cytochrome c (Co-cyt c) is immobilized on Antimony-doped Tin Oxide (ATO) as a catalyst for photoelectrochemical oxidation of water. Under illumination with blue light ($\lambda > 450$ nm), the ATO-Co-cyt c photoanode displays ~ 6-fold enhancement in photocurrent density relative to ATO-Co-protoporphyrin IX (Co-PPIX) at 0.3 vs SCE at pH 5.0. Light-induced water oxidation activity of the system was demonstrated by detecting evolved stoichiometric H_2 and O_2 with gas chromatography and incident photon to current efficiency was measured as 4.1%. The faradaic efficiency for generated oxygen was 97% with TON number of 671 after six hours. The current density had a slow decay over the course of six hours of constant irradiation and applied potential, which exhibits the robustness of catalyst-ATO interaction.

Introduction

The ability to capture and store solar energy efficiently into renewable fuels is a fundamental soluton for the growing energy demand. Photoelectrochemical (PEC) water oxidation using semiconductor materials is a promising technology to harvest and store solar energy.[101–103] Water splitting could be divided into two half reactions: 1) water oxidation in which O_2, $4H^+$, and 4e are generated, 2) proton reduction in which H_2 is the final product. The bottleneck of the full process is the first step which occurs on the photoanode and involves multiple electron and proton transfers, as well as O-O bond

formation, thus requiring high overpotenial[104]. Hence, development of stable and cost-effective photoanodes with high efficiency is a crucial step in designing water splitting systems. One effective approach to overcome the high overpotential barrier of water oxidation is using water oxidation catalysts (WOCs). Metal oxide complexes harboring ruthenium, iridium, nickel, and cobalt has been reported as efficient water oxidation catalysts[105–110], although their dependence on organic solvents limits their application in water oxidation catalysis. Water-soluble biomolecules offer an alternative approach for biofuel catalysis and energy conversion.[111] Integrating biological units of life, for example proteins, into artificial inorganic materials combines natural biological functions with the attractive properties of solid-state electronics.[112] Porphyrin is an organometallic cofactor in many natural metalloproteins and offers the ability to bind to various metals such as Ni, Fe, Mn, and Co.[113,114] Cytochromec (cyt c) is a heme binding redox-active protein with the cofactor covalently coordinated to two of its cysteine residues and serves as an electron transport component of the respiratory chain of anaerobic specious (Figure 3.1.).[115] The affinity of cyt c to a series of solid materials semiconductors and light absorbers including Indium doped Tin Oxide (ITO), WO_3, SnO_2, TiO_2 has been investigated, yet its capability to serve as a catalyst remained unexplored.[116–118] Among all of the explored materials, mesoporous Antimony doped Tin Oxide (ATO) has emerged as a favored TCO (Transparent Conductive Oxide) due to its low-cost and excellent optical properties.[119] In addition, ATO's high electrical conductivity combined with its unique large surface area marks it as an interesting framework for integrating biomolecules.[120] It has been demonstrated that ATO provides protective encapsulation for

the biomolecule of interest, without destructing its biological functionality. In this context, Simmons et.al showed DNA nanostructures can be absorbed in ATO pores and their structure remains intact.[121] The high capability of ATO for functional inclusion of biomolecules was also demonstrated by Seo et.al, in which they showed cyt c is absorbed in thin films of highly mesoporous ATO with retention of its native structure and electron transfer properties.[122] The immobilization strategy of binding cytc to ATO is based on the electrostatic interaction between substantial negative charges on the metal oxide surface and the protein's positively charged surface, mediated by lysine residues. This ATO-cyt c assembly displays a promise for fabrication of a catalytic system.

In this work, we fabricated a photoelectrochemical water oxidation system with ATO-absorbed Co-cyt c. The system exhibits maximum TON of 671 for oxygen at pH 5.0. Increased photocurrent density relative to Co-PPIX demonstrates that protein scaffold provides a protecting environment on the active site by keeping it from degradation.

Materials and Methods

General Information:

All chemicals and solvents were purchased from commercial suppliers and used without further purification. UV-Vis spectra were recorded on a Varian Cary Bio Spectrophotometer. Concentration of Co-cyt c was measured using cyt c's extinction coefficient of 11580 M^{-1} cm^{-1} at 280 nm. ICP-MS data were collected from a Thermo-Finnigan Neptune ICP-MS. FT-IR-ATR data were collected using a Bruker IFS 66v/S instrument equipped with a diamond ATR and KBr beam splitter. Gas analysis was performed in an SRI instruments, Model no. 310C GC with a 5Å molecular sieve column

with a thermal conductivity detector and argon as carrier gas. Calibration curves for H_2 were made by injecting various volumes of a standard gas mixture containing 1% H_2 and 99% N_2 onto the GC. Calibration curve for O_2 was created using various volumes of air.

Preparation of ATO Film on FTO Glass:

ATO-coated FTO slides were prepared using reported protocols in literature.[22]

Metal Substitution Procedure:

10 mg lyophilized cyt c was dissolved in 10 mL of glacial acetic acid and 500 µl of concentrated HCl were added to the solution. Working in the dark, the solution was added to a Schlenk flask and oxygen was removed via 3 freeze-pump-thaw cycles. 100 mg of $FeCl_2$ was added and the solution was refluxed under argon for 8 hours until its color changed from red to purple, indicating successful demetallation. The acid was removed under vacuum and 2 ml of water was added and evaporated. The resulting powder was dissolved in 2.5 ml of 50 mM sodium acetate, 100 mM EDTA, and desalted with Sephadex G-25 pd10 desalting columns.

Cobalt insertion

40 mg Co $(OAc)_2$ was dissolved in 2 ml methanol and added to the demetallated cyt c. The solution was degassed with argon and refluxed for 5 hours. Completion of the reaction was detected with emerging the Soret band at 421nm. The reaction mixture was then purified with RP-HPLC C18 Semi-Preparative column.

Incorporation of Co-cyt c into ATO coated FTO slides:

ATO coated FTO slides were dried by heating at 180°C for 30 min add cooled to room temperature prior to immersion in the protein solution. Binding of Co-cyt c to the ATO

pores was accomplished by soaking the ATO-coated slides in a solution of 50 μM Co-cyt c overnight. The slides were then rinsed with water to remove the physiosorbed specious and were dried for further experiments.

Photocurrent measurements and Cyclic Voltammetry:

Photoelectrochemical measurements and cyclic voltammetry were performed on a CH-Instruments 1242B electrochemical workstation with a three-electrode system containing a SCE reference electrode, a Pt counter electrode, and ATO-Co-cyt c working electrode. All scans were performed at 100 mV/s unless otherwise mentioned. Illumination was performed using a Kessil blue lamp.

ICP-MS

To prepare the ICP-MS samples, Co-cyt c functionalized ATO slides were immersed into 10 mL of concentrated OmniTrace sulfuric acid and heated at 60 °C for 20 min. The solution was then sonicated for 1 hour and diluted for the measurement. Three samples of Co-cyt c functionalized ATO was prepared as well as blank ATO as the control.

Photoelectrochemical Water Splitting:

All photoelectrochemical water splitting experiments were performed in a three-electrode configuration as mentioned before in 100 mM citrate buffer pH 5.0 and 1M KNO_3 as the supporting electrolyte and were purged with argon for 1 hour prior to each experiment to degas the buffer. The amount of produced H_2 and O_2 was measured by taking 150 μL of the cell's headspace with a gas tight syringe and was injected to a GC instrument with 5Å molecular sieve column, a TCD detector, and argon carrier gas.

FTIR-ATR

FTIR spectra were recorded on a Bruker instrument by placing the ATO-Co-cyt c on a diamond ATR for surface measurements and putting a drop of Co-cyt c solution in a liquid cell for in solution measurements. 200 scans were performed to obtain the maximum signal to noise ratio.

Faradic Efficiency Calculations

The passed charge carriers through the external circuit were measured with integrating the area under the i-t plot in a 6 h photoelectrochemical water splitting experiment. Simultaneously, amounts of produced H_2 and O_2 was detected by gas chromatography. The Faradic efficiency was calculated according to the following equation:

$$\eta_{\text{oxygen}} = \frac{\text{amount of oxygen (mol)}}{\text{amount of e/4 (mol)}} \qquad \text{Equation 3.1.}$$

The Incident Photon to Current Efficiency (IPCE):

The following equation was used to calculate the IPCE:

$$\text{IPCE (\%)} = \frac{\text{Number of electrons generated}}{\text{Number of incident photons}} * 100 \qquad \text{Equation 3.2.}$$

Ferrioxalate actinometry experiment was used to calculate the number of incident photons. The two solutions required for conducting actinometry are 0.15 M potassium ferrioxalate and 0.1% buffered phenanthroline solution.

To prepare the 0.15 M potassium ferrioxalate, 1.3g of potassium ferrioxalate was dissolved in 18mL of water with 2 mL of 1.0 N H_2SO_4. 0.1% buffered phenanthroline was prepared by dissolving 1.12g of sodium acetate, and 5mg of phenanthroline in 5mL of 1.0 N H_2SO_4.

To conduct the actinometry experiment, 3 mL of potassium ferrioxalate were added to a 1cm × 1cm quartz cuvette and irradiated with the Kessil lamp for 1 minute while stirring, and another cuvette was left in the dark as the control. 500 μL of 0.1% buffered phenanthroline solution was added to both cuvettes upon completion of the irradiation and allowed to develop in dark for 5 minutes. The absorption for both samples were measured at 510 nm, and the amount of produced Fe^{2+} during irradiation was measured using the following equation:

$$[Fe^{2+}] = \frac{A_{light} - A_{dark}}{\varepsilon_{510\ nm}\ l}$$ Equation 3.3.

The photon flux absorbed by the sample then calculated by the established methods in literature.[123]

Results and Discussion

Co-cyt c was obtained by removing iron via reductive demetallation, and inserting cobalt by heating the protein in Cobalt acetate.[124] The absorption spectrum of the resulting product is consistent with six-coordinated Co (III) porphyrin. Co-cyt c were then deposited on highly mesoporous ATO coated FTO via soaking the ATO electrode in 50 μM solution of the protein in 50 mM tris pH 7.0 overnight. As shown in Figure 3.2., the position of the Soret and Q bands does not change upon grafting the protein in the mesoporous ATO. This indicates the efficient interaction of Co-cyt c with ATO while retaining its native structure within the pores.

ATR-FTIR spectroscopy shows the integrity of Co-cyt c in the pores of ATO. Proteins give rise to multiple characteristic peaks in IR spectroscopy, from which amide I and amide II are the most important bands. The amide I band arises from the C=O stretching

vibrations of the amide bonds and is found in the range between 1600 – 1700 cm^{-1}. The amide II is found in the range of 1480 – 1575 cm^{-1} and derives mainly from N-H bending and C-N stretching vibrations.[125] The observed peaks at 1637 cm^{-1} and 1640 cm^{-1} in Figure 3.3 arise from the CO stretching of Co-cyt c in solution and on ATO respectively. The amide II band at 1530 cm^{-1} is detected for both in solution and ATO-integrated Co-cyt c.

These results confirm the binding of Co-cyt c to the ATO by electrostatic interactions. Electrochemical activity of ATO incorporated Co-cyt c was investigated by cyclic voltammetry. The pair of voltammetric redox signals shown in Figure 3.6 exhibits electrochemically reversible faradaic oxidation/reduction peaks centered at -0.34 V vs SCE which is consistent with Co (III)/Co (II) redox couple anchored to the metal oxide.

The reduction potential of Co-cyt c in solution was measured to be -0.43 V vs; the consistency between Co-cyt c's redox potential in solution and immobilized on ATO suggests that the protein is in a native conformation. The electrochemical peaks were not weakened or changed upon keeping the slide in solution for 15 mins, indicating the relatively stable absorption of Co-cyt c on ATO. However, the quite large peak separation of 250 mV indicates a relatively slow interfacial electron transfer kinetics.

The linear dependence of the peak current density to the scan rate is shown in Figure 3.5. This is a common feature of surface immobilized specious and confirms the strong binding of Co-cyt c to the ATO surface, which is opposite to the loosely bonded cyt c on ITO surface with a diffusion-limited behavior.[126]

Based on the estimated area under the CV wave of Co (III)/Co (II) redox couple, the electrochemically active surface coverage of Co-cyt c was determined to be 2.2 ± 0.5 nmol cm^{-2}, this value is in a good agreement with previous reported amounts of incorporated cyt c on ATO.[122] ICP-MS measurements resulted in an average surface coverage of 5.45 ± 0.48 nmol cm^{-2} for cobalt, indicating approximately 40% electroactive coverage. Indeed, ATO's ability to immobilize high loading of Co-cyt c in its electroactive form brings about reliable quantification of the results and efficient photo-oxidation of water.[127] To build a photoelectrochemical (PEC) water splitting cell, a three-electrode system was used including ATO-Co-cyt c as the photoanode working electrode, Pt wire as the counter cathode, and SCE as the reference electrode with a visible light source ($\lambda > 450$ nm). The electrodes were placed in a glass cell which was sealed with rubber septa and equipped with inlet and outlet syringes for degassing.

Figure 3.7 demonstrates ability of the ATO-Co-cyt c photoanode to generate a photocurrent upon irradiation with a blue light and a maximum of 55 μA cm^{-2} is achieved at pH 5.0 when 0.3 V of potential vs SCE was applied. The positive photocurrent is indicative of electron flow from the electrons to the ATO. The oxidized cobalt then catalyzes oxidation of water molecules. The photocurrent remains stable over 30s light-on intervals and then decays to zero when the light is turned off.

The effect of pH on the generated photocurrent is shown in Figure 3.8. A photocurrent of less than 5 μA cm^{-2} was observed at pH values from 8.9 to 6.4, and it raised to 11.63 μA cm^{-2} upon decreasing pH to 5.8. Notably, the photocurrent bounced to 55 μA cm^{-2} at pH 5.0 and remained stable during 30 s light illumination. As shown in Figure 3.1, Co-

PPIX in cyt c is coordinated to two axial ligands as histidine and a methionine. The jump in the generated photocurrent from 11.63 μA cm^{-2} in pH 5.8 to 55.52 μA cm^{-2} in pH 5.0 indicates higher activity of the catalyst due to protonation of the axial histidine and leaving an open coordination site for the water molecule. The second coordinated ligand along with the two thioether linkages between porphyrin and protein scaffold keep the Co-PPIX prostatic group in the active site while maintaining the protein folded. The pH dependence of PEC water oxidation suggests a proton coupled electron transfer (PCET) mechanism involved in the catalysis. Considering the highest water oxidation activity of Co-cyt c at pH 5.0, we selected citrate buffer at this pH for further studies.

Generated photocurrent from ATO-Co-cyt c at different external bias were measured in 100mM citrate buffer pH 5.0. The maximum photocurrent was obtained at 0.3 V vs SCE and further increase was not observed at higher potentials. In addition, bare ATO shows negligible (2 μA cm^{-2}) photocurrent density upon illumination with the blue light at 0.3 V vs SCE, demonstrating the function of Co-cyt c as the catalyst component of the system.

In order to compare the water oxidation activity of Co-cyt c with Co-PPIX, ATO was immersed in a 50 μM solution of Co-PPIX in methanol overnight. The photocurrent density of ATO-Co-PPIX in citrate buffer was measured and a maximum of 9 μA cm^{-2} was observed, while ATO-Co-cyt c shows a much stronger signal (Figure 3.9). Moreover, a decay in the photocurrent was observed for ATO Co-PPIX in 30 s of light illumination as opposed to ATO-Co-cyt c's stable photocurrent over long irradiation periods. 5 μM of Co-cyt c in solution generated 8 μA cm^{-2} of photocurrent, while only 2 μA cm^{-2} was obtained from 5 μM Co-PPIX. To determine whether this observation is due to the

enhanced catalytic activity of Co-cyt c or its better diffusion to the electrode, diffusion coefficient of Co-PPIX and Co-cyt c in solution was measured using Randles-Sevcik equation (Equation 3.4.), where n is the number of transferred electrons, A (cm^2) is the electrode surface area, C^0 (mol cm^{-3}) is the analyte bulk concentration, and D_0 (cm^2 s^{-1}) is the diffusion coefficient of the analyte. This equation describes the peak current i_p (A) dependence on the square root of scan rate ν (V s^{-1}) for electrochemically reversible electron transfer processes.[128]

$$i_p = 0.446nFAC^0\left(\frac{nF\nu D_0}{RT}\right)^2 \qquad \text{Equation 3.4}$$

The generated current at varying scan rates for Co-cyt c and Co-PPIX at the same concentration (5μM) in 100 mM citrate buffer pH 5.0 was measured and the current vs square root of the scan rate was plotted as shown in figures 3.10 and 3.11. The calculated diffusion coefficient from these plots is 1.68 *10 $^{-9}$ cm^2 s^{-1} and 2.31*10^{-9} cm^2 s^{-1} for Co-cyt c and Co-PPIX respectively. The higher diffusion coefficient for Co-PPIX indicates that the higher photocurrent generated from Co-cyt c in solution is due to the impact of the protein environment on enhancing porphyrin's water oxidation capability.

Bulk electrolysis for ATO-Co-cyt c photoanode was conducted in a gas-tight photoelectrochemical cell with three electrode configurations in 100 mM citrate buffer at pH 5.0 (1M KNO_3 supporting electrolyte) with a 0.3 V vs. SCE applied bias. As shown in Figure 3.12, stable photocurrent was obtained with blue illumination of the photoanode over 1000s. FT-IR-ATR spectrum of ATO-Co-cyt c after irradiation was performed to investigate the stability of the catalyst in ATO pores after catalysis. As depicted in Figure

3.4, amide I and amide II peaks are still observed with a slight shift towards higher wavenumbers. This shift is attributed to hydrogen bond formation between protonated side chains in the protein due to exposing to lower pH value of 5.0. The observed bubbles on the surfaces of the working electrode and Pt counter electrode are shown in Figure 3.13 and they demonstrate evolution of gas in the system. The evolution of oxygen and hydrogen were confirmed and measured with gas chromatography, by taking a sample of the photoelectrochemical cell's headspace at the end of the photo-electrolysis. 1.9 μmol H_2 and 1.1 μmol O_2 was produced, and a and TON of 671 was calculated for O_2.

Comparison of the charge passed through the system during the illumination with the amount of generated O_2 gives the faradaic efficiency of 97% for oxygen. The incident photo to current efficiency (IPCE) of the system has also been measured using actinometry which is described in the materials and methods section. Using a blue light source with a wavelength at around 450 nm, the calculated IPCE was 4.1%.

In conclusion, we have designed and assembled a photoanode using Co-cytc with ATO electrode for oxidation of water with high faradaic efficiency. The ATO-Co-cyt c photoanode is facile to assemble and features high stability over 6 hours of operation, and evolution of both oxygen and hydrogen gases are observed during visible light irradiation of the device with applied potential bias of 0.3 vs SCE. Our results are important in exploiting the redox activity of small proteins such as cyt c in designing PEC water oxidation tandem cells to improve the overall electron transfer kinetics and efficiency of the system.

Table 3.1

n (O_2) µmol	TON (O_2)*	Co surface concentration	Faradaic Efficiency
1609 ± 45	15.62±0.44	103±45	96%

*TON was calculated using surface concentration of cobalt in nmol m^{-2}. ATO's surface area was measured using BET (Brunauer-Emmett-Teller) theory as 92.82±0.18 m^2 g. Using the weight of ATO coating the surface area was calculated as 0.02 m^2.

Figures

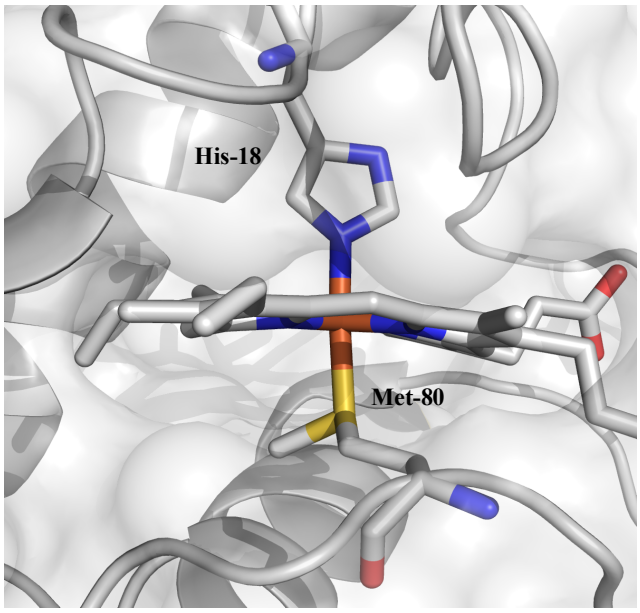

Figure 3.1. Crystal structure of cyt c active site (PDB 1HRC). Highlighted residues are His/Met di-axial coordinating ligands.

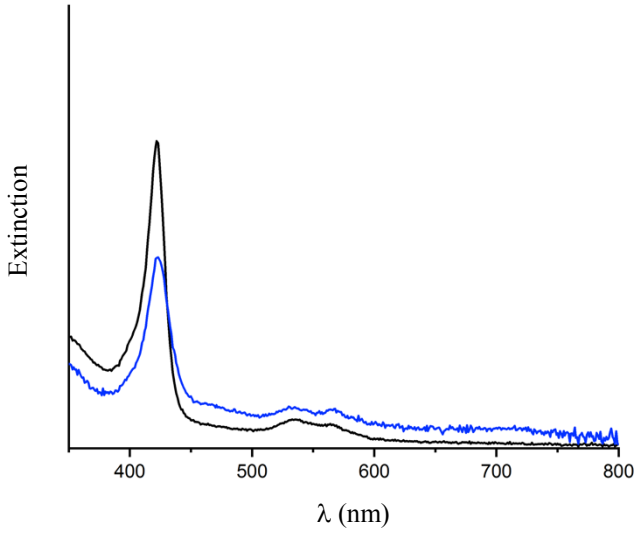

Figure 3.2. UV-Vis spectra of Co-cyt c in 100mM tris, pH 7.5 (black), and Co-cyt c absorbed on ATO coated slide in air (blue). The extinction spectra of blank ATO was taken in air and subtracted from the extinction spectra of ATO-Co-cyt c. The obtained data were multiplied by 3 to improve the visuality of the spectrum. The Soret band maxima at 421nm for both Co-cyt c in solution and on ATO represents six-coordinated Co (III)-porphyrin.

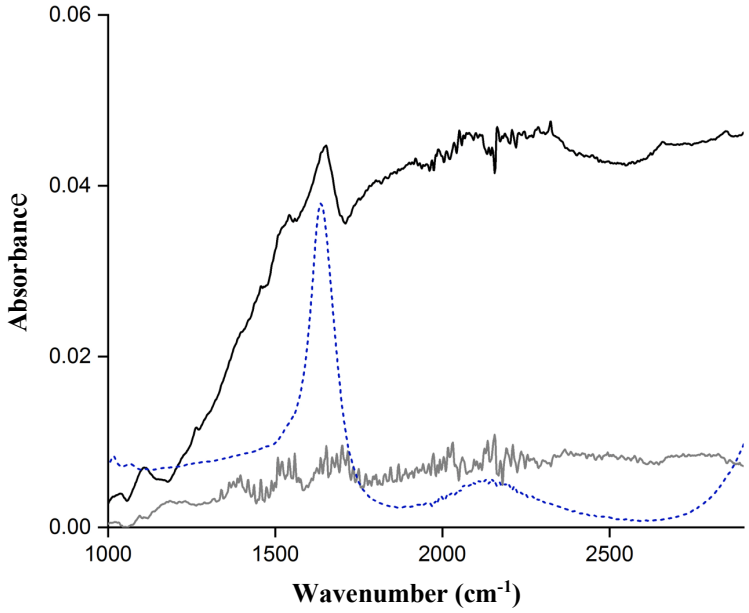

Figure 3.3. IR spectra of blank ATO (gray), ATO with incorporated Co-cyt c (black), and Co-cyt c in solution (dotted blue). The spectrum of Co-cyt c in solution was taken in 100 mM tris pH 7.5 using the instruments liquid cell. The spectra for solid samples were obtained directly on the diamond ATR. The IR spectra of ATO-Co-cyt c and Co-cyt c show the characteristic bands for amide I and II at 1650 cm^{-1} and 1530 cm^{-1} respectively.

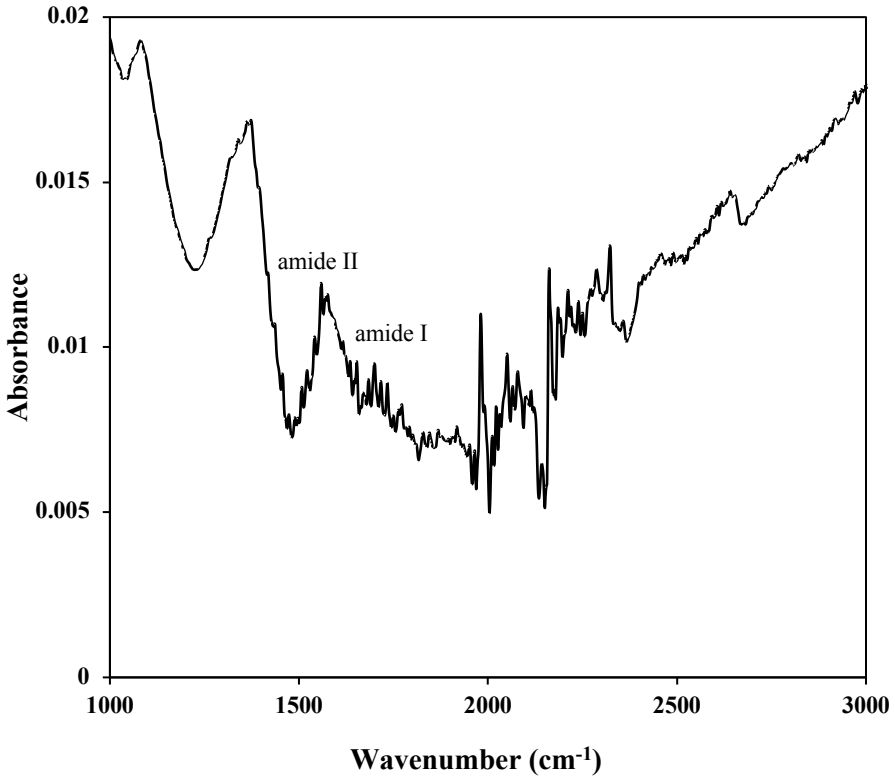

Figure 3.4. IR spectrum of ATO-Co-cyt c after bulk electrolysis. Amide I and amide II peaks appeared at 1695 cm^{-1} and 1575 cm^{-1}. The spectrum was taken using the solid sample on a diamond ATR.

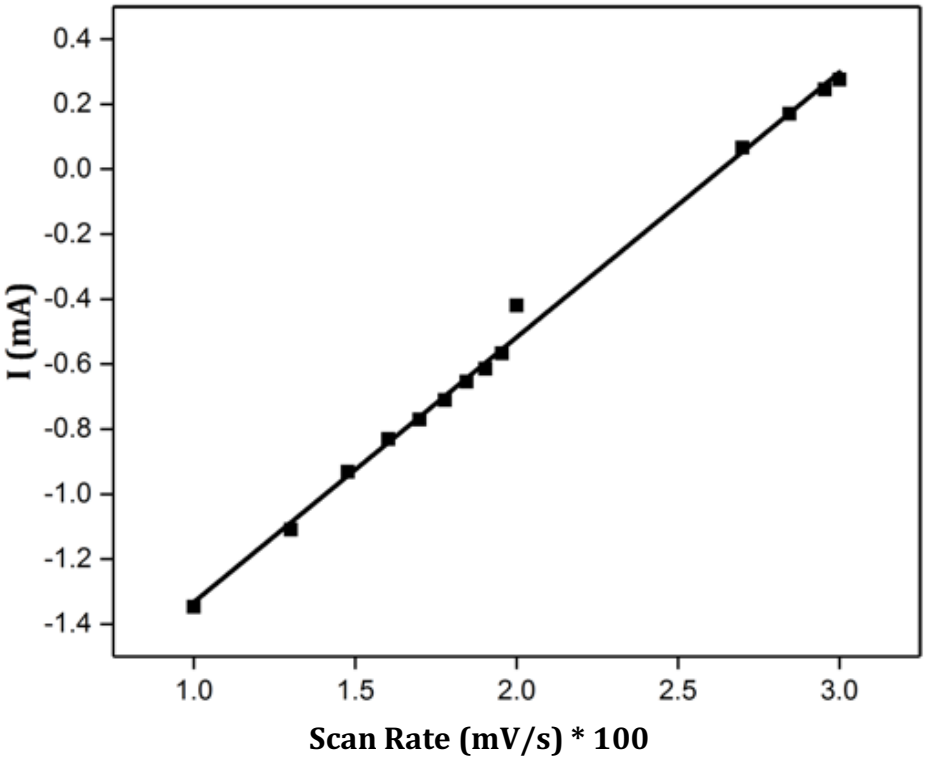

Figure 3.5. Anodic peak current dependence on scan rate for Co-cyt c absorbed on ATO. The cyclic voltammetry was taken in 100 mM tris buffer pH 7.5, 100 mM NaCl supporting electrolyte.

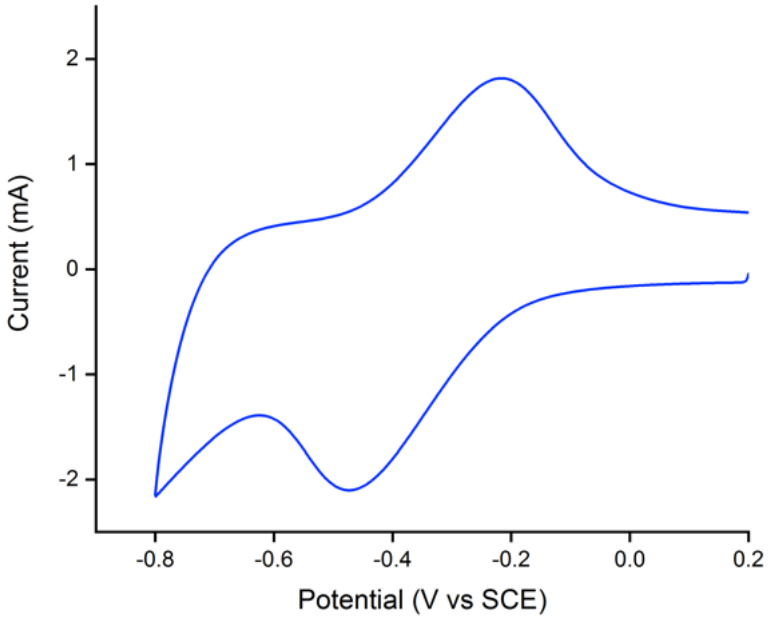

Figure 3.6. Cyclic voltammograms of ATO-Co-cyt c in 100 mM citrate buffer, 1M KNO_3, pH 5.0 at scan rate of 100 mV s^{-1}, the redox wave at -0.34 V vs SCE is assigned to Co (III) to Co (II).

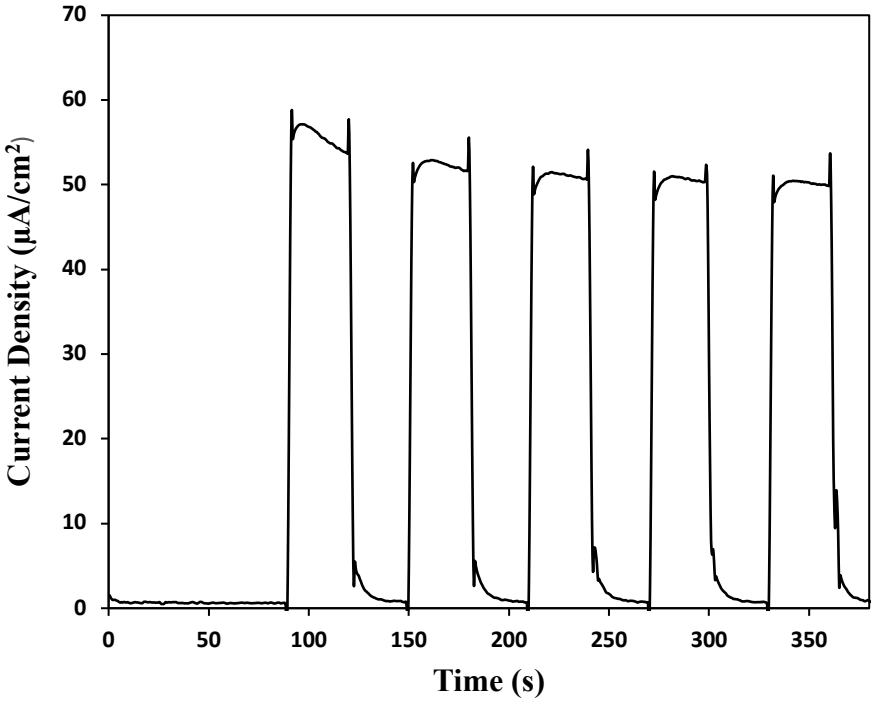

Figure 3.7. Light on/off photocurrent measurement for ATO-Co-cyt c. The data were collected in 100 mM citrate buffer, 1 M KNO_3, pH 5.0. The applied potential bias was 0.3 V vs SCE. The irradiation was performed with a blue light for 30 s at each cycle.

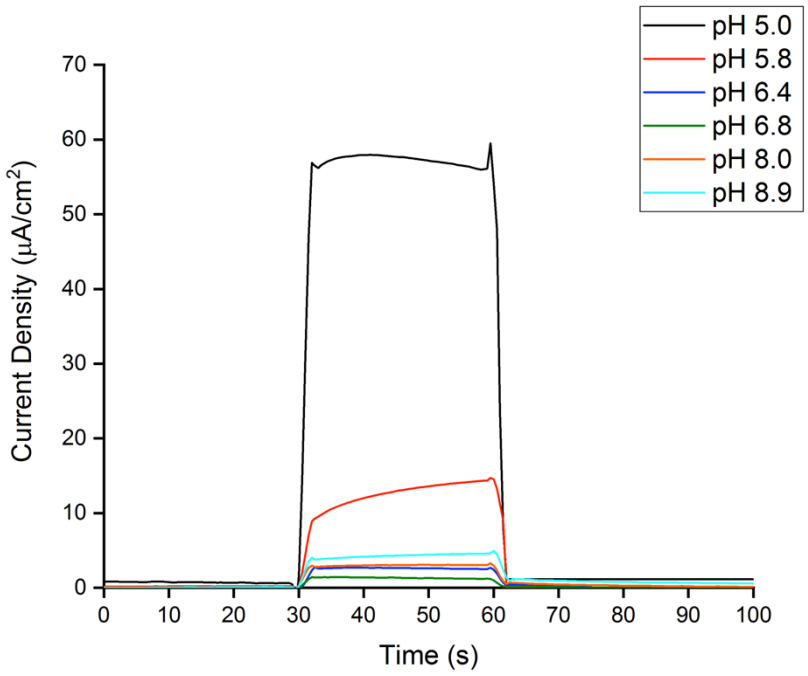

Figure 3.8. Chronoamperometry experiment with ATO-Co-cyt c in various pH values. 100 mM citrate buffer was used for pH 5.0, 5.8, 6.4, and Tris buffer was used for pH 6.8, 8.0. 8.9. The applied potential bias was 0.3 V vs SCE.

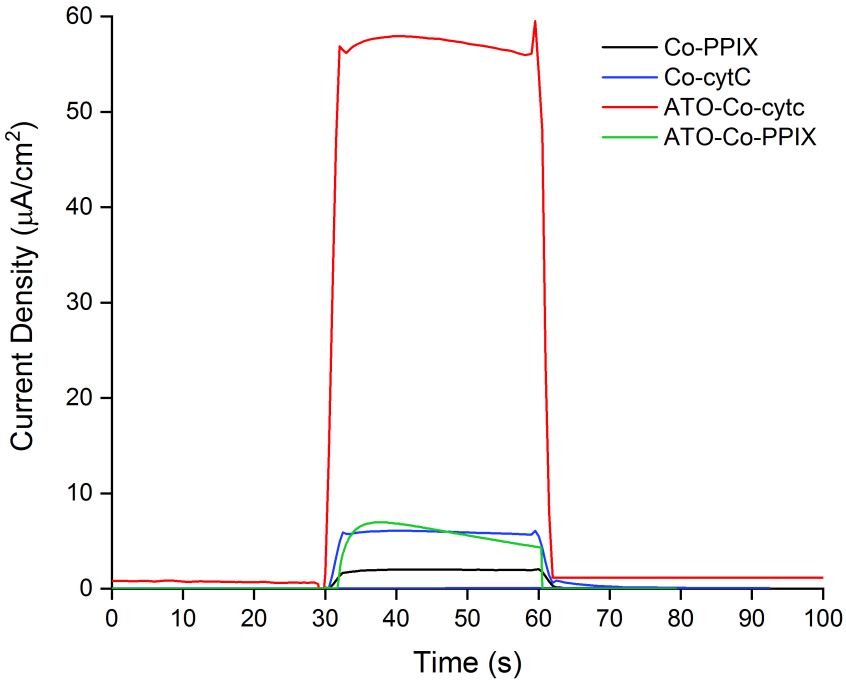

Figure 3.9. Chronoamperometry measurements in a three-electrode configuration in 100 mM citrate buffer pH 5.0; applied bias 0.3 vs SCE; with a blue light source. 5 μM Co-PPIX in solution (black), 5 μM Co-cyt c in solution (blue), ATO-Co-PPIX (green), and ATO-Co-cyt c (red).

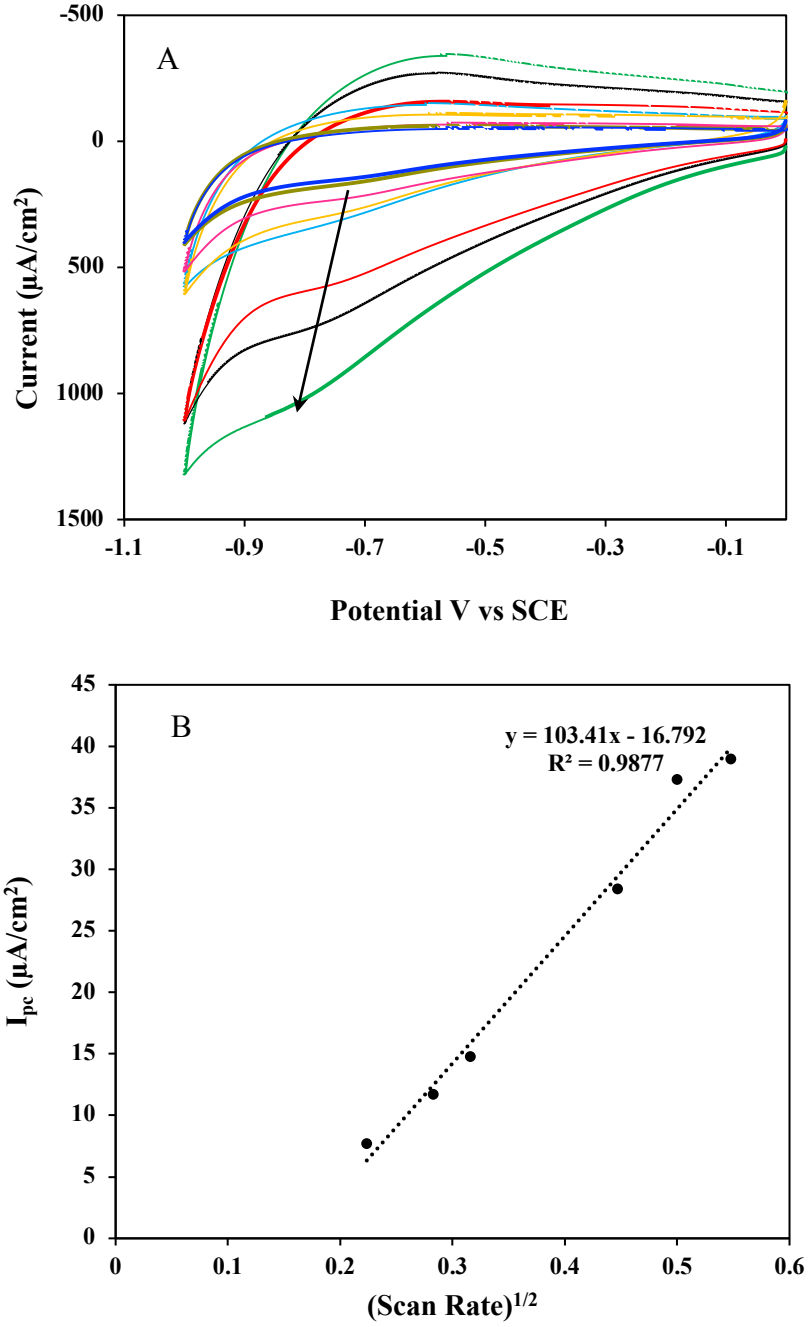

Figure 3.10. (A) Cyclic voltammetry of 5 µM Co-PPIX in 100 mM citrate buffer, 1M KNO_3, pH 5.0, at varying scan rates (B) The I_{pc} vs square root of scan rate obtained from A to calculate the diffusion coefficient.

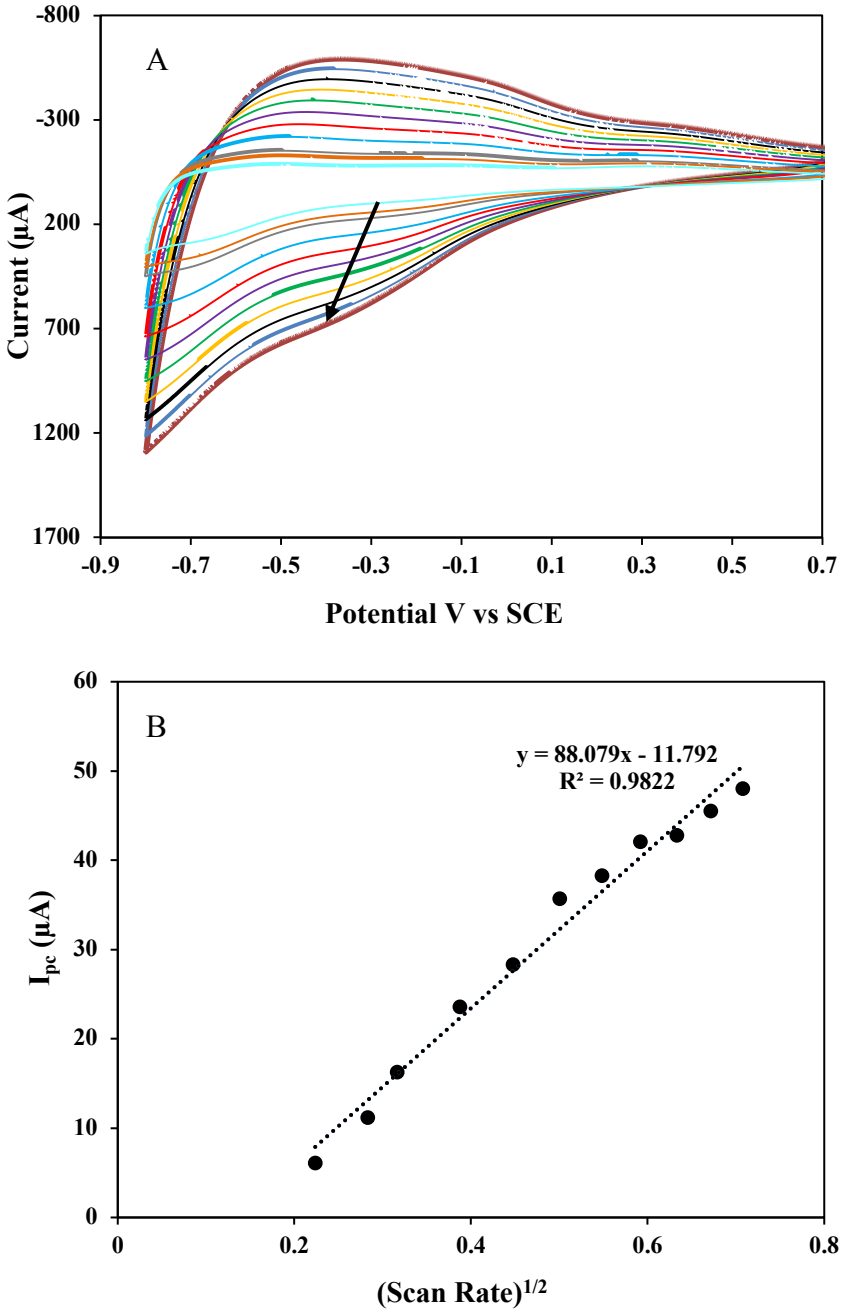

Figure 3.11. (A) Cyclic voltammetry of 5 µM Co-cyt c in 100 mM citrate buffer, 1M KNO_3, pH 5.0, at varying scan rates (B) The I_{pc} vs square root of scan rate obtained from A to calculate the diffusion coefficient.

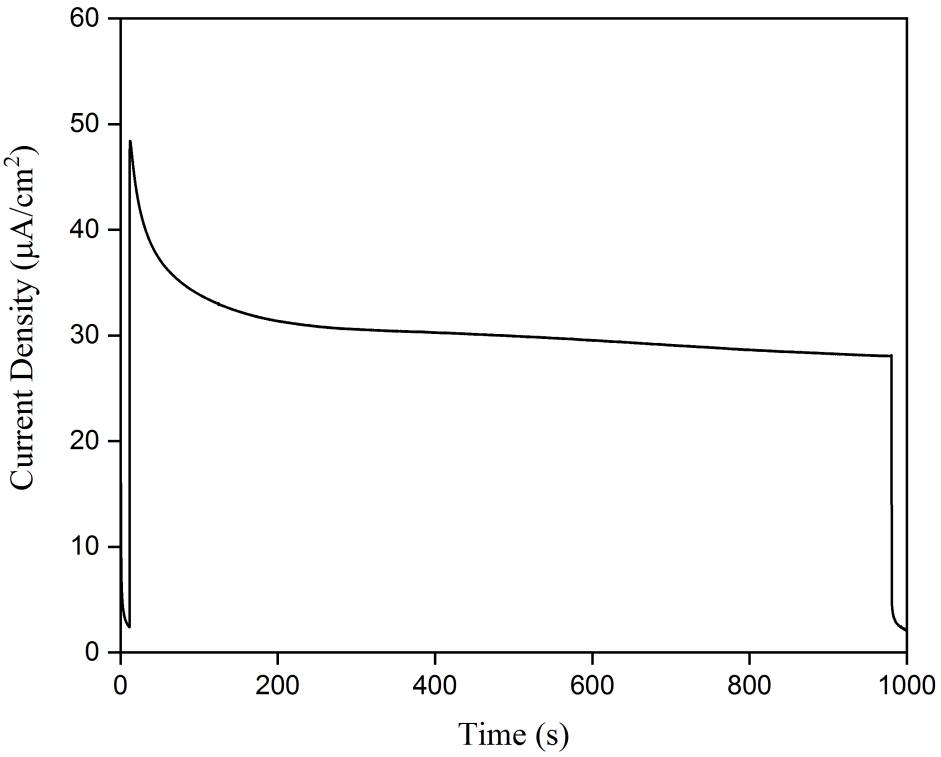

Figure 3.12. Bulk electrolysis measurement with a 0.3 V applied potential vs SCE with ATO-Co-cyt c as the working electrode in 100 mM citrate buffer pH 5.0, illumination was performed with a blue light source.

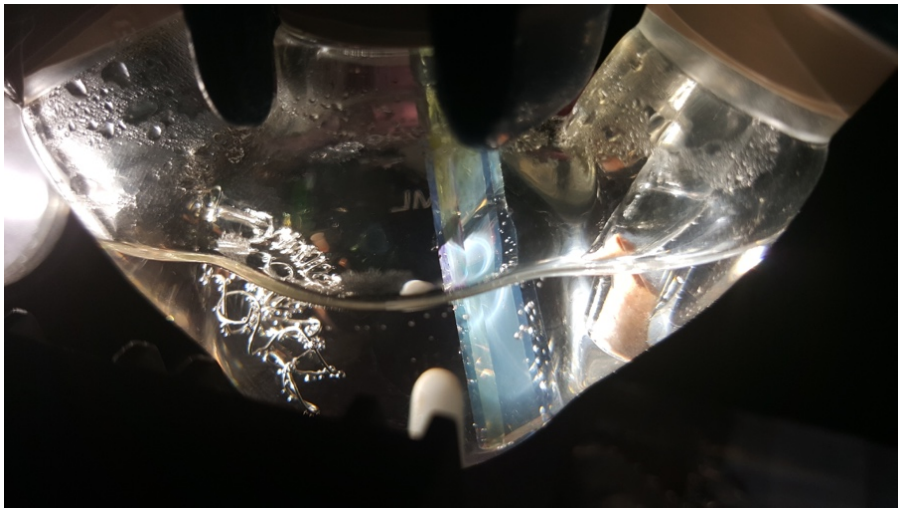

Figure 3.13. Evolution of gas bubbles on the ATO-Co-cyt c working electrode and Pt counter electrode upon illumination in bulk electrolysis.

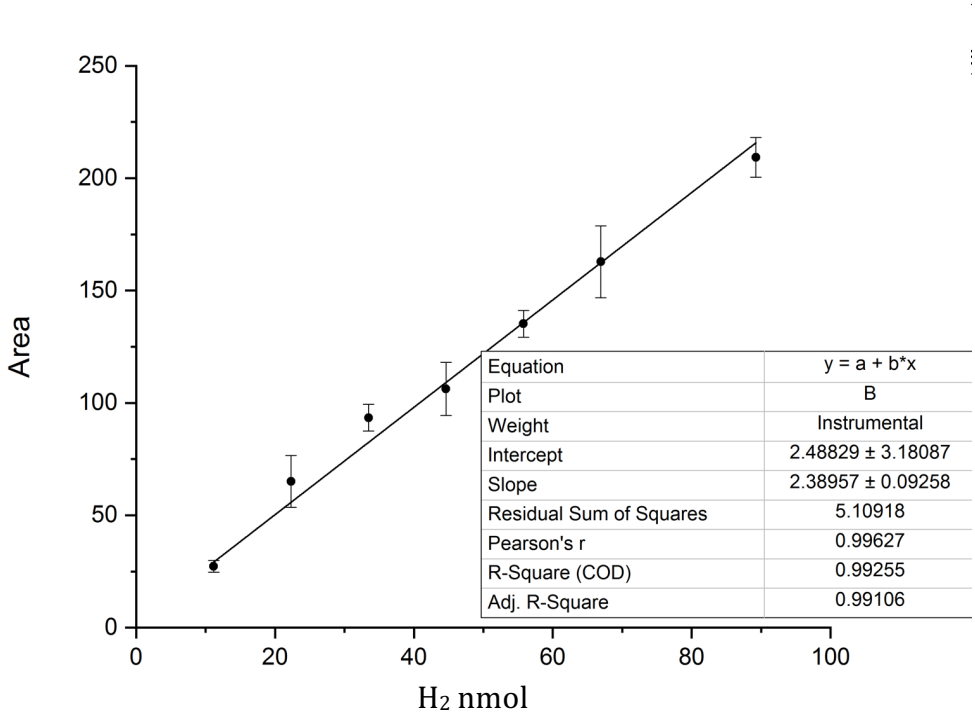

Figure 3.14. Gas chromatography calibration curve for H_2 gas obtained with a standard gas containing 1% H_2 and 99% N_2. The equation is y = 2.49 + 2.39x, and the calculated R^2 is 0.99

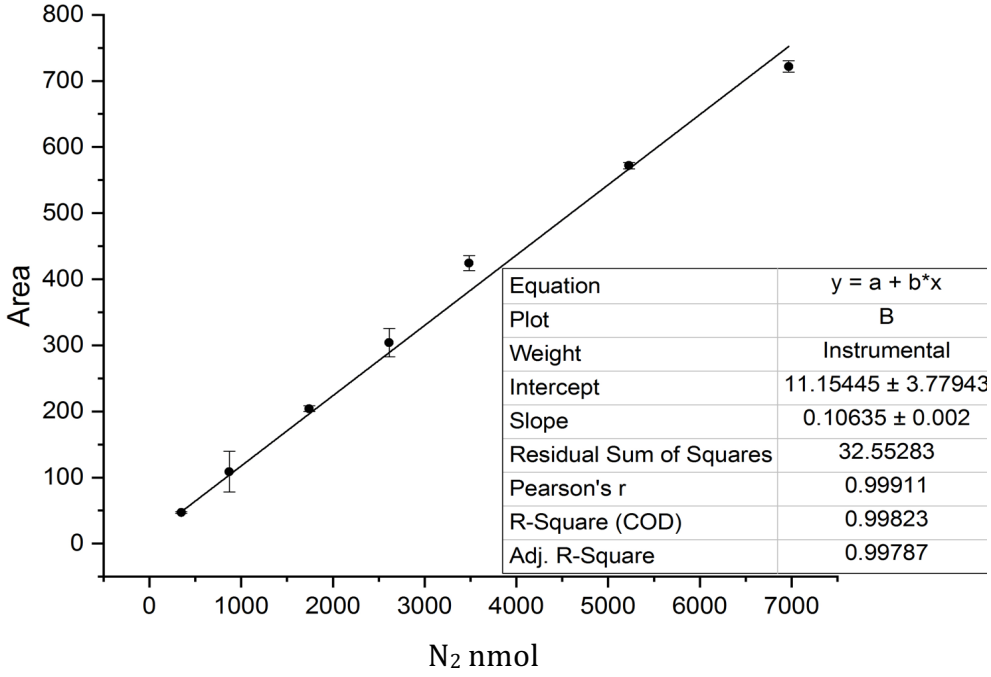

Figure 3.15. Gas chromatography calibration curve for N_2 gas obtained with injecting various volumes of air to the GC column. The equation is y = 11.15 + 0.1x, and the calculated R^2 is 0.99

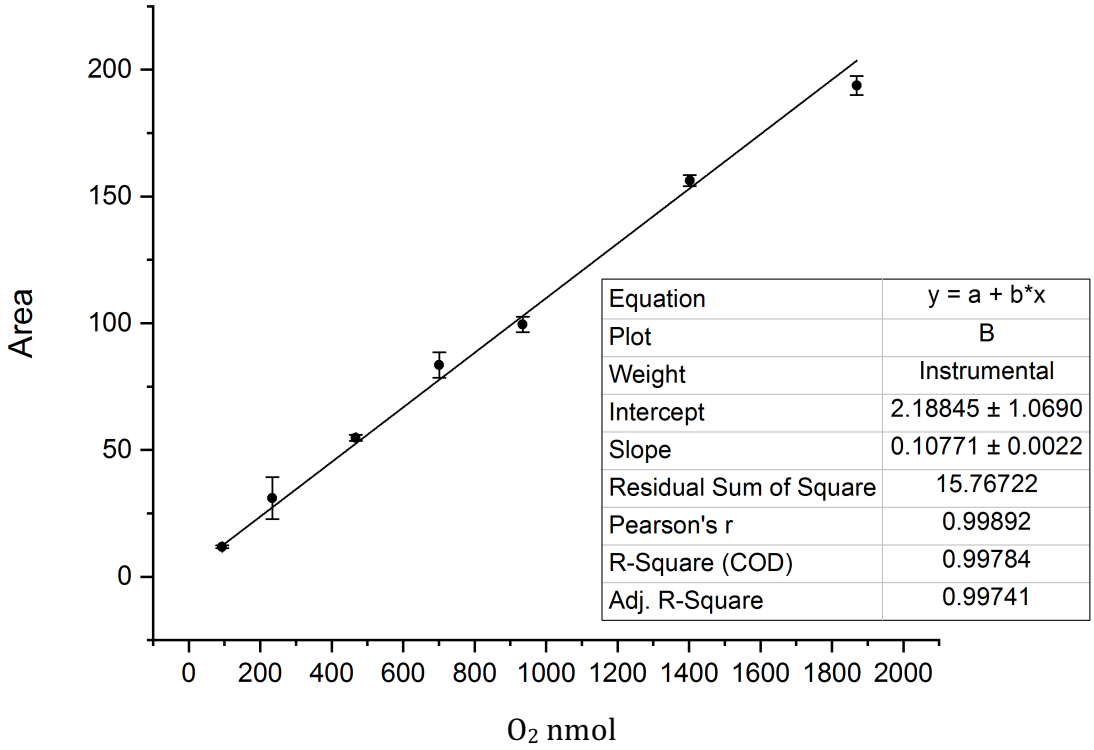

Figure 3.16. Gas chromatography calibration curve for O_2 gas obtained with injecting various volumes of air to the GC column. The equation is y = 2.19 + 0.11x, and the calculated R^2 is 0.99

CHAPTER 4

A WHOLE CELL E. COLI DISPLAY PLATFORM FOR DESIGNED HEME-BINDING PROTEINS: HYDROGEN PRODUCTION WITH COBALT-CYTOCHROME B_{562}

Abstract

Whole cell biocatalysis has emerged as a unique and promising strategy for cost-effective and efficient biosynthesis of chemicals and pharmaceutical products. This approach has several aspects to optimize, including modification of the organism for the intended biocatalysis, designing immobilized biocatalysts, and investigations for the toxic properties of the solvents and produced chemicals. Bacterial cells provide the required viability under the most extreme conditions and have been utilized to harbor biocatalytic activity for many chemical transformations. In this work, an inner membrane whole cell biocatalytic system is designed for light-induced hydrogen production using E. coli. A heme-deficient strain of E. coli which thrives in presence of external trans-metallated porphyrin was exploited to incorporate a non-natural porphyrin, Co-PPIX, to the enzyme's binding pocket.

Introduction

To date, there has been no report of a biological system that exploits cobalt for reduction of protons to hydrogen, yet a significant amount of scientific efforts have been made to design and develop cobalt-based molecular catalysts for photoelectrochemical and photochemical hydrogen production.[129] The reason for such a promise in cobalt complexes as proton reduction catalysts is their low overpotentials (down to 40 mV),

high turnover numbers, and high turnover frequencies.[130,131] Cobalt-based hydrogen-evolution catalyst complexes commonly share Co^{2+} or Co^{3+} resting states and they are categorized into several groups based on their ligands; however, despite the success in designing various cobalt-based hydrogen evolution catalysts, prevailing dependence of these complexes on organic solvents is still a bottleneck. There have been only a handful of water soluble molecular cobalt complexes for hydrogen production.[132]

Porphyrins consist of four pyrrole rings interconnected by methine groups. They absorb strongly at the visible region of light due to their high degree of conjugation.[133] A common feature of all kinds of porphyrins is their ability to bind to metal ions such as Fe, Zn, Mg, Co, and Ru at the center of their ring. Cobalt porphyrin complexes are attractive candidates as hydrogen-evolving catalysts which are functional in organic solvents or acidic aqueous solutions.[134] In a generalized scheme, there are two possible pathways for catalytic hydrogen production which both proceed through cobalt-hydride intermediates (Scheme 4.1). Homolytic mechanism takes place when two metal hydride complexes donate a proton and an electron to form a hydrogen molecule. On the other hand, further protonation of the metal hydride yields hydrogen through heterolytic pathway. The prevailing pathway in cobalt-catalyzed hydrogen production depends on experimental conditions including pH, catalyst concentration, and proton source.[135–137]

Bren et. el reported a porphyrin-binding biomolecular catalyst for hydrogen production in neutral water with a proteolytic fraction of microperoxidase-11 (MP11) which is transmetallated with cobalt.[138] MP11 has eleven residues with a covalently linked Co-PPIX and one axial histidine coordinated to the metal center. This enzyme catalyzed

electrochemical hydrogen production with a TOF of 6.7 s^{-1} and overpotential of 852 mV, with a TON of 20000. However, the activity of MP11 is sustained for only 15 min and this was attributed to porphyrin degradation due to being exposed to the solution.

Secondary shell coordination site of the protein impacts the catalytic functionality of porphyrins, and it induces enhancement to its photoinduced hydrogen generation. In an effort to design a biomolecular hydrogen evolution catalyst, Ghirlanda et.al employed a cobalt-porphyrin binding myoglobin as a photoelectrochemical hydrogen evolving catalyst in mild aerobic conditions with TON of 520 over the course of 8 hours of irradiation.[139] Mutations of His residues that are in close proximity to the active site to Ala resulted in modulation activity of the catalyst 2.5 folds. This design approach exemplifies the importance of secondary coordination shell of the artificial hydrogen-evolving active site, showing that optimizing protein contacts can result in a significant increase in activity. Ghirlanda et. al has also explored the catalytic reactivity of Co-cyt b_{562} for photoinduced hydrogen evolution to investigate the effect of dual axial coordination in Co-PPIX catalytic activity, and the resulting TONs were modulated to 305 by making point mutations in the porphyrin coordination site.[140] The protein scaffold in these proteins is amended to bind to the porphyrin by axial coordinations (Figure 4.1), and mutations leave an open position for the substrate (in this case protons) to bind to the metal center. Furthermore, the native and well-folded structure of the protein improves the catalytic activity through second-sphere and long-range interaction.

Porphyrin substitution in protein is arduous and most protocols to incorporate non-natural porphyrins into protein scaffolds depend on harsh, denaturing conditions to

extract the heme. Therefore, heme substitution brings about challenges and low recovery of active proteins. One possible approach to address this issue is to express the protein with non-natural porphyrin in vivo, and it requires alteration in heme biosynthesis mechanism in the cell. A close look at heme biosynthesis pathway in bacteria will assist to design a system that incorporates trans-metallated porphyrins into proteins. As depicted in Figure 4.2, the heme biosynthesis in bacteria takes place in eight enzymatically catalyzed steps[141]. RP522 is a strain of E.coli which cannot biosynthesize heme due to a mutation on its HemB gene.[142] On the other hand, supplementing RP522 growth media with heme does not have any effect on its growth as the cells cannot uptake external porphyrins. In order to make RP522 heme permeable, it was chemically mutagenized and grew on heme supplemented plates. The resulting medium to large colonies were then selected as heme-permeable strains, called as RP523.[143] Therefore, RP523 is an E. coli strain that has an auxotrophic *hemB* mutation which makes it unable to biosynthesize heme, and an uncharacterized mutation that makes it permeable to external porphyrins and facilitates heme uptake. Here, RP523 strain was utilized to introduce non-natural porphyrins to heme binding proteins.[144] This strategy was exploited in this work to express cyt b_{562} with Co-PPIX in vivo.

Extraction and purification of enzymes from whole cells requires costly and labor-intensive procedures. As a result of that, up to 60% of industrial biocatalytic reactions exploit whole cell catalysis.[145] In spite of cost effectiveness of whole cell catalysis, finding a compatible platform that bypasses catalyst inactivation in the cell is a challenge. In this context, cell surface display offers a promising approach to separate the catalyst

from the often-poisoning cellular environment and provides a phenotype-genotype linkage for further purposes such as directed evolution. Cell envelope of gram-negative bacteria such as E. coli is composed of an inner and an outer membrane and this feature invokes a potential platform to design membrane anchored or membrane infused catalysts The most important transport pathway for exporting proteins out of the cytosol in bacteria is the secretion (or Sec) pathway. In order to facilitate the transportation in Sec pathway, the precursor protein should possess a signal peptide that directs the protein to the cell export system in the cytoplasmic membrane. Sec signal peptides have a conserved overall structure. The n-region which consists of a positively-charged amino acid(s), the h-region which is very hydrophobic, and the c-region which contains the signaling recognition site. All three sections play crucial roles in the effective translocation of Sec substrates in the cell[146–152]. Once transported through the membrane, the Sec sequence gets cleaved by translocase enzymes. In this work, Sec signaling sequence was cloned down-stream of cyt b_{562} gene and the signaling recognition site was mutated in order to prevent cutting the Sec from cyt b_{562} gene; this way the proteins remains anchored to the inner membrane upon translocation. The designed membrane-anchored Co-cyt b_{562} was used as a whole cell hydrogen production catalyst.

Materials and Methods

Preparing porphyrin-supplemented TB plates

To 25 g/L Terrific Broth (TB) media was added 12g/L agar-agar and autoclaved. The mixture was cooled down to ~50°C and 50 μg/mL kanamycin was added to the media. Porphyrin was added to the solution to a final concentration of 30 μg/mL. A solution of

200x (6 mg/mL) of porphyrin in 100 mM NaOH and 200 mM Na_2PO_4, pH 12 used as the stock. The TB agar was then poured into Petri dishes, allowed to solidify, and stored at 4°C wrapped in aluminum foil.

Expression of cytochrome b_{562} in RP523 strains

pET26b-Sec-cyt b_{562} plasmid was transformed to RP523 competent cells using the heat shock method and plated on TB-Kanamycin plates supplemented with heme or Co-PPIX to grow overnight in the dark until the colonies appear. To inoculate colonies,14 mL of TB media was transferred to a sterile Hungate tube and 1X (50 μg/mL) Kanamycin was added to the solution. The tubes then inoculated with picking individual RP523 colonies and the tube was capped with sterile stoppers. The media was purged with sterilized argon for half an hour. The degassed culture was incubated at 37°C overnight while shaking. To begin the protein expression, 100 mL TB, 1X kanamycin, and 0.2% of filter-sterilized D-(+)-glucose was transferred to a sterile small bottle and the medium was inoculated with 1-2 mL of the starter culture. The bottle was crimp-sealed and degassed with filter-sterilized argon for one hour to ensure full deoxygenation. Culture was incubated at 37°C for about 4-5 hours while shaking. The expression was induced at OD_{600} = 0.6 with 1 mM IPTG where 500 μl of 200X heme or Co-PPIX were added and incubated overnight aerobically. Cells were harvested and centrifuged at 5000 RPM and the pellet was kept at -80°C for further analysis.

Protein extraction and purification

Cells were resuspended in 100 mM Tris, 1mM EDTA pH 8.0, lysed with sonication and centrifuged for 30 min at 5000 RPM. Ammonium sulfate was added to the supernatant to

70% concentration and the solution was stirred at 4°C for 3 hours. The suspension was centrifuged, and the supernatant was dialyzed against 50 mM tris pH 8.0 to remove the remaining ammonium sulfate. Reverse-phase HPLC was used to further purify the protein. 100 µl of the supernatant was injected to a C18 HPLC column with the flow rate of 1mL/min in a gradient purification method starting with 0.1% TFA in water to 95% acetonitrile, 0.1% TFA for 50 min. The retention time for cyt b_{562} is 35 min.

Cell outer membrane removal and fractionation

This protocol was used to rupture the outer membrane of E. coli. The cells are called "spheroplasts" after removing their outer membrane. The protein was expressed in E. coli using described protocol. Each sample for spheroplasting should contain 1×10^{10} cells. One OD_{600} contains 10^9 cells; this estimation was used to calculate the required volume that contains enough cell density. The appropriate volume of induced culture was centrifuged at 13000 RPM at room temperature for 5 min in a 1.5 ml centrifuge tube. The supernatant was removed, and the pellet was resuspended in 100 µl of ice-cold fractionation buffer which is 750 mM sucrose and 100mM tris (pH 8.0). The solution then centrifuged at 13000 RPM for 1 min and the supernatant was removed. The pellet was resuspended in 350 µl of ice-cold-fractionation buffer and 0.1 mg/ml lysozyme. The tube was slowly vortexed while 700 µl of 1 mM EDTA was added dropwise, and slowly rotated on a rocker for 20 min. To the tube was then added 50 µl of ice-cold 0.5 $MgCl_2$ and incubated on ice for 10 min, then centrifuged at 11000 RPM for 1o min. The pellet was isolated as the spheroplasts and was resuspended in ice-cold 1X PBS buffer. Spheroplasts can be stored at 4°C for up to two days.

TEV protease his tag digestion

20 μl of spheroplast fraction was added to 7.5 μl of 20X TEV buffer (50 mM Tris-HCl, pH 8.0, 0.5 mM EDTA), 1.5 μl of 0.1 M DTT, 1 μl of AcTEV protease (10 U/μl) and the final volume was adjusted to 150 μl. The solution was incubated at 4°C overnight and purified with affinity chromatography.

Light-induced H_2 production

50 μL of whole cells with expressed Sec-Co-cyt b_{562} at OD of 90 was resuspended in 50 mM tris buffer and 250 μM tris (bipyridine) ruthenium (II) chloride was added as the sensitizer and 100 mM ascorbic acid was added as sacrificial electron donor. The reaction was stirred and irradiated for 3 hours. 250 μM tris (bipyridine) ruthenium (II) chloride and 100 mM ascorbic acid in 50 mM tris buffer used as a negative control and irradiated for 3 hours. 150 μL of the headspace were removed with a gas-tight syringe and injected to GC for analysis. Calibration was achieved by injection of different volumes of 99% N_2 and 1% H_2 gas mixture to the GC.

Results and Discussion

RP523 strain of E. coli was used to incorporate Co-PPIX into cyt b_{562}. A *hemB* (Phophobilinogen synthase) disruption gene makes this strain unable to biosynthesize heme, and another uncharacterized mutation renders it heme-permeable. Therefore, the bacterial growth media has to be supplemented with Co-PPIX under aerobic conditions to keep the cells growing. Expression of proteins under anaerobic conditions leads to improper insertion of heme and the expression of proteins with Co-PPIX should be conducted in two steps:1) growing the bacteria under anaerobic fermentation conditions

to reach to a sufficient culture density and 2) inducing the expression under aerobic conditions and supplementing the medium with Co-PPIX.[144]

Figure 4.3 shows the RP523 cell paste after expression and the soluble fraction of lysed cells. The red color is indicative of cyt b_{562} overexpression with heme and Co-PPIX. Absorption spectroscopy was performed to analyze the expression of cyt b_{562} with heme and Co-PPIX respectively and the results are shown in Figure 4.4. The absorption bands were observed at 418 nm, 531nm, and 562 nm corresponding to Fe (III) porphyrin[153] and 429 nm, 541nm, and 574 nm corresponding to Co (III) porphyrin.

The protein translocation across the inner membrane is facilitated through the Sec pathway, which consists a set of cytosolic and membrane proteins. A hydrophobic N-terminal region, i.e., a signal sequence is always required to make the secretory protein as a substrate for the Sec translocon. The Sec translocon in bacteria has four major components including SecB, SecA, SecYEG, and SecDF. SecB is a cytosolic molecular chaperone which keeps the newly synthesized preprotein in an unfolded conformation and targets it to the translocon to bind to the motor protein, SecA. This protein consumes ATP to thread the unfolded protein through the membrane.[154]

In order to facilitate exporting cyt b_{562} to the bacterial periplasmic space, a N-terminal signaling peptide was cloned into the cyt b_{562} expression vector along with a tobacco etch virus protease (TEV), as shown in Figure 4.5 (A). The signal sequence is cleaved between Ala and Lys amino acids upon being transported across the inner membrane. The Ala and Lys cleavage site was mutated to Val and Arg, as shown in Figure 4.5 (B), to alter the digestion site and to prevent the cleavage so that the protein gets anchored in

the inner membrane. The signaling sequence, 6-His tag, TEV cleavage site, and cyt b_{562} gene were cloned to pET26b plasmid and transformed to RP523 cells and expressed in the presence of Co-PPIX as described in the experimental section. The wild-type (non-mutated) signaling sequence was used as a control. Sequences of each variant are shown in Figure 4.6.

The bacterial cell envelope consists of a complicated multilayer structure that separates the inside of the cell from its external often hostile environment and regulates selective passage of nutrients from the outside and waste products from the inside. Gram-negative bacteria's cell wall has three principal layers; the outer membrane (OM), the peptidoglycan cell wall, and the inner membrane (IM). The OM is an asymmetric layer that contains a phospholipid-rich inner leaflet and an outer leaflet consisting of lipopolysaccharides (LPS). The OM is more permeable than the IM and most hydrophobic molecules are able to penetrate the hydrophobic OM bilayer. Divalent cations, particularly Mg^{2+} and Ca^{2+} play an essential role in maintaining the OM integrity. These ions bind to the anionic phosphate groups of the inner leaflet and link the LPS molecules together electrostatically. Therefore, the interaction of chelating agents such as EDTA with the OM disrupts its integrity and releases LPS into the solution. Once the EDTA permeabilizes the OM, the lysozyme can enter the periplasmic space and impairs the peptidoglycan cell wall.[155] Therefore, a combination of EDTA and lysozyme is used in most laboratory practices to remove the Gram-negative bacteria OM. In order to test the membrane-anchoring feature of Sec-Co-cyt b_{562}, the cell's outer membrane was removed using the described fractionation protocol and collected fractions were used to

run SDS-PAGE. The second lane from right on the gel shown in Figure 4.8 represents the collected periplasmic fraction of the cell and there is no band corresponding to Sec-Co-cyt b_{562}. This means the mutations in the cleavage site of the signaling sequence were effective and it is not cut upon translocating the protein through the membrane. The indicated band on the third lane matches with Sec-Co-cyt b_{562} mass.

The membrane-anchored Sec-Co-cyt b_{562} should be exposed to the solvent after removing the outer membrane. It is assumed that the protein will be released into the periplasmic space upon cleaving the 6-His tag with TEV protease. To test this assumption, TEV protease 6-His tag cleavage was performed to investigate the presence of anchored Sec-cyt b_{562} on the inner membrane, and the resulting mixture was purified with batch Ni-NTA. The wash fraction (line 7 in Figure 4.8) shows the protein without 6-His tag and the elution fraction (line 8 in Figure 4.8) indicates the tagged protein. Figure 4.7 shows the absorption spectra of the collected fractions after OM removal. The first wash with the fractionation buffer removes solubilized porphyrin from the whole cells and the broad absorption peak at 395 nm is indicative of dissolved Co-PPIX (the light blue trace). The periplasmic fraction was collected after adding EDTA and lysozyme and the 395 nm peak arising from dissolved Co-PPIX is still present, indicating the penetration of porphyrin through the OM. The spheroplast fraction shows a band at 427 nm which corresponds to six-coordinated Co-PPIX and demonstrates the presence of Co-PPIX-bonded cyt b_{562} on the IM. After TEV protease digestion, the supernatant shows a peak at 427 nm, indicating the release of Sec-Co-cyt b_{562} into the solution upon removing the tag.

Light-induced hydrogen production with membrane-anchored Sec-Co-cyt b_{562}

The catalytic performance of membrane-anchored Sec-Co-cyt b_{562} was tested for light-induced hydrogen generation in aqueous solution. Tris(bipyridine) ruthenium (II) chloride (RuP) was used as photosensitizer and ascorbic acid as sacrificial electron donor. 512 nmol of hydrogen was produced after three hours of irradiation, and 80 nmol of hydrogen was detected after 3 hours of irradiation of only RuP as a negative control. The calibration curve was generated using a standard 1% H_2 in 99% N_2 and it is shown in Figure 4.9.

In summary, cyt b_{562} was expressed in RP523 strains in presence of external Co-PPIX to yield Co-cyt b_{562}. The Sec translocase machinery of the bacteria was then employed to transport the protein across the inner membrane and the alterations in the translocase cleavage site made the protein anchored to the inner membrane. The catalytic activity of the system towards hydrogen production was investigated in presence of a photosensitizer and a sacrificial electron donor and the generated hydrogen was detected with gas chromatography. This designed whole cell catalyst can be used for future studies in directed evolution to further optimizing its activity.

Figures

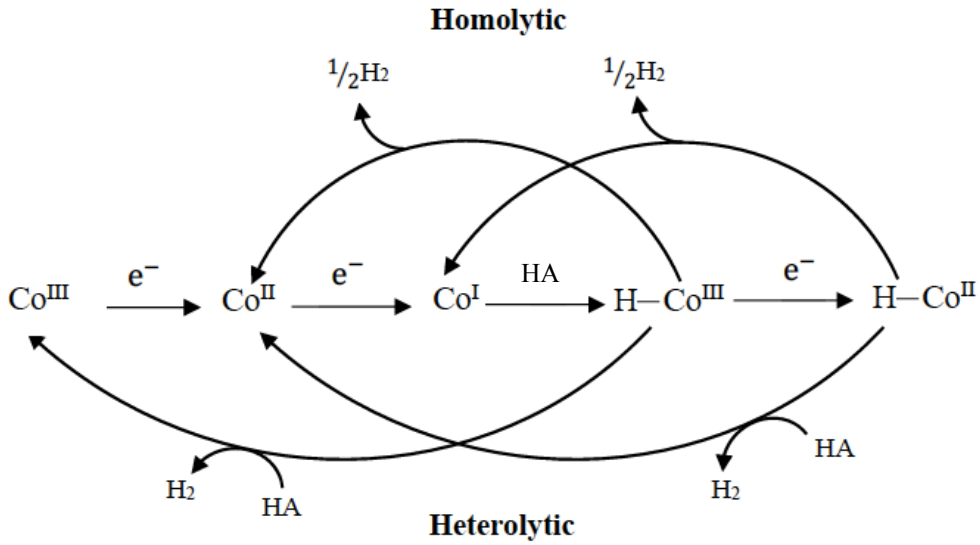

Scheme 4.1. Homolytic and heterolytic pathways for hydrogen production catalyzed by cobalt complexes.

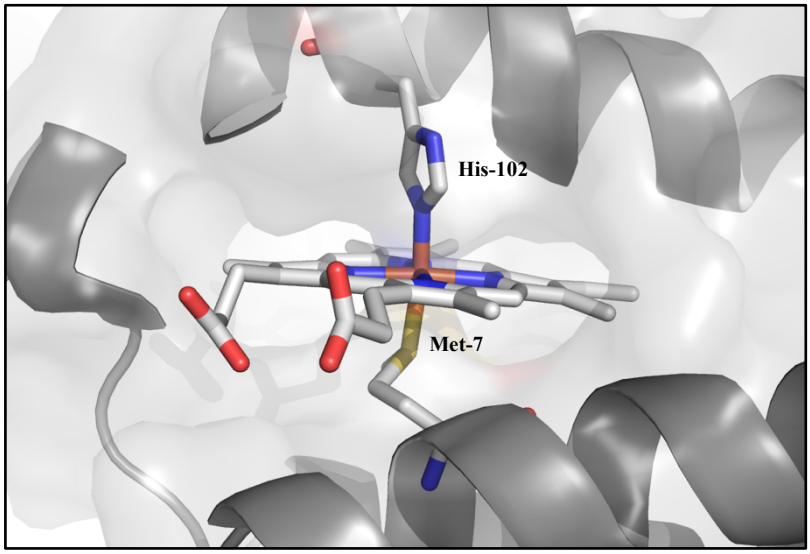

Figure 4.1. Active site of cyt b_{562}, from the crystal structure, PDB 1QPU. The heme is held in the hydrophobic pocket of the four-helix bundle by two axial coordinations provided by Met-7 and His-102.

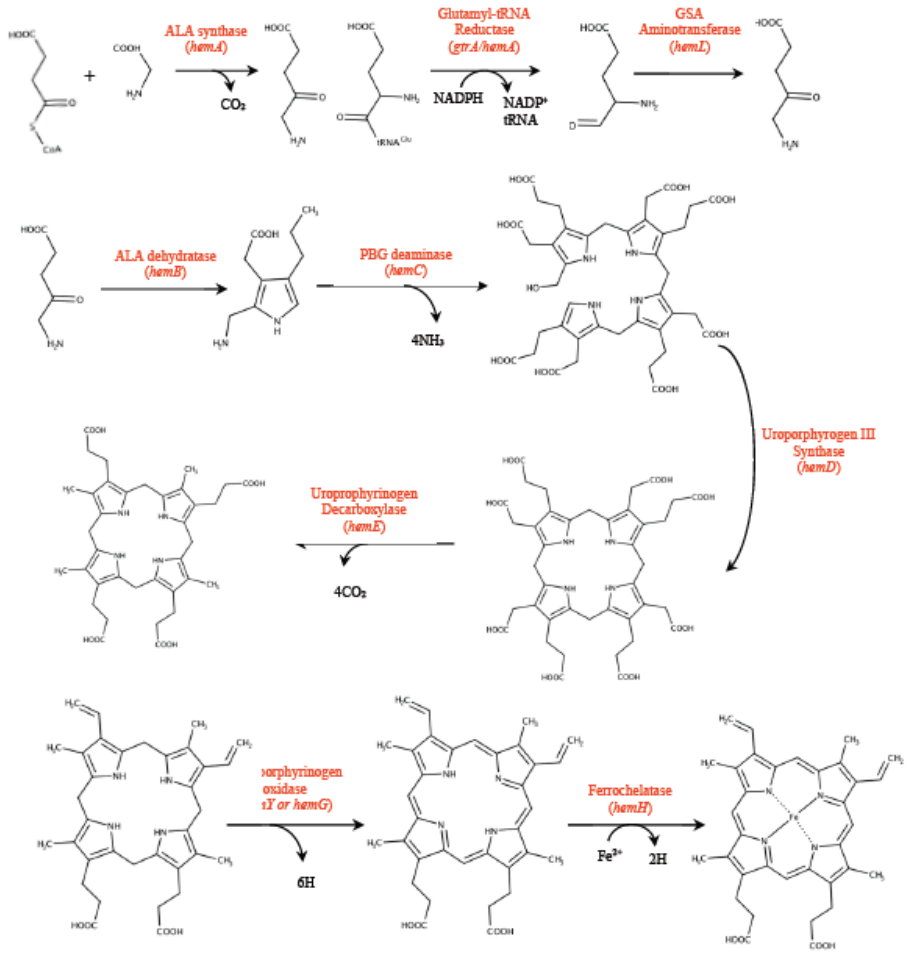

Figure 4.2. Heme biosynthesis pathways in bacteria

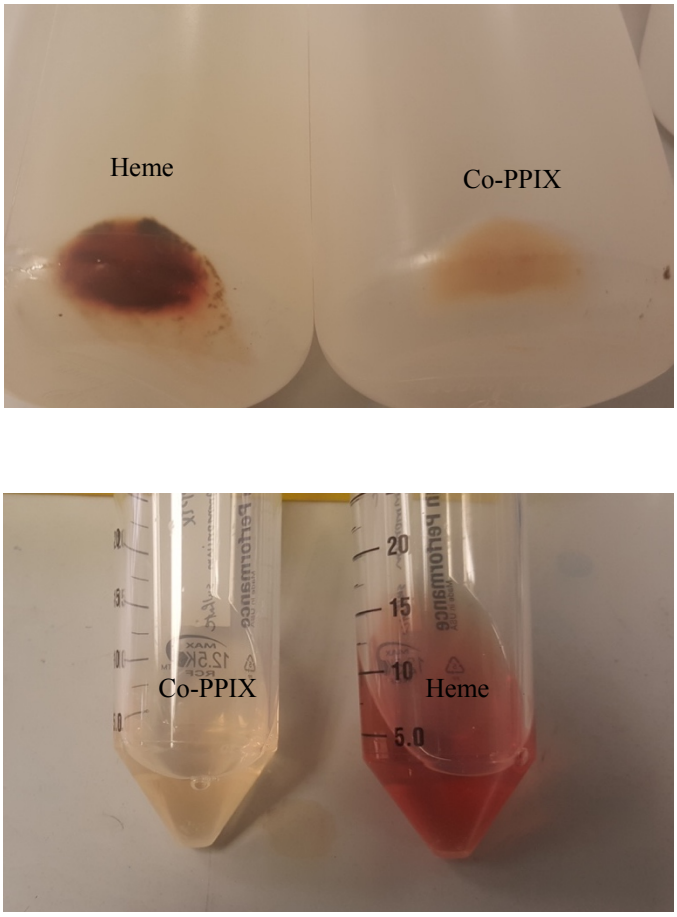

Figure 4.3. (A) Harvested cell paste for overexpression of cyt b_{562} with heme (left) and Co-PPIX (right), (B) soluble fraction after cell lysis for cyt b_{562} with heme (right) and Co-PPIX (left). The expression yield for cyt b_{562} in presence of Co-PPIX is less and that is why the cells with cobalt porphyrin are less red than the ones with heme.

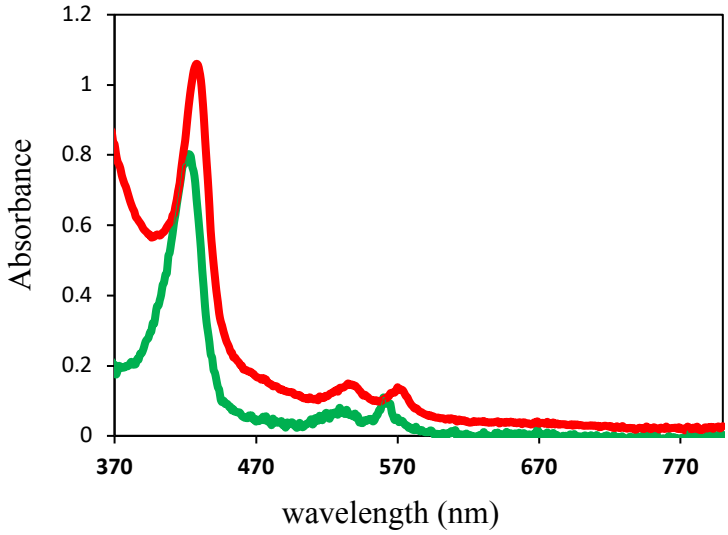

Figure 4.4. Absorption spectra of cyt b_{562} expressed in RP523 strains. Heme cyt b_{562} is shown in green and Co-PPIX-cyt b_{562} is shown in red.

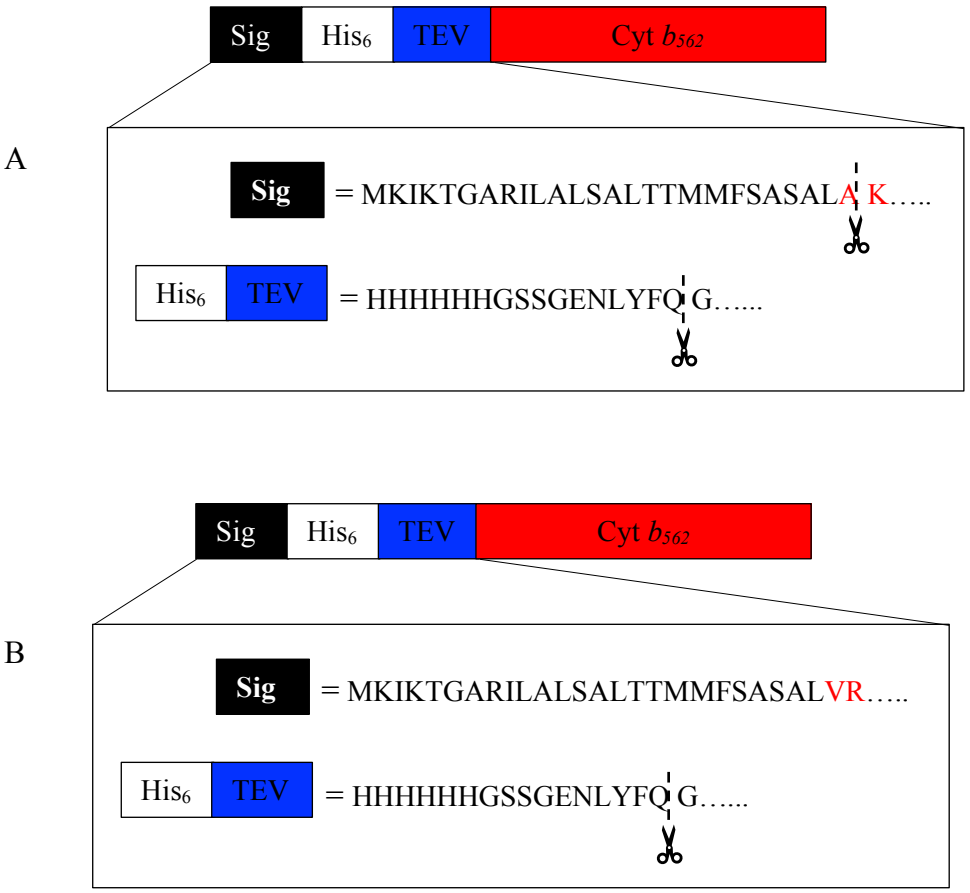

Figure 4.5. Design of periplasmic and membrane-anchored cyt b_{562} gene. (A) The N-terminal signal sequence (black), a six-histidine tag (white), and TEV protease cleavage site (blue). The signal sequence is cleaved between A and K residues upon transporting the protein across the inner membrane[156]. (B) The inner-membrane anchored cyt b_{562} gene includes the same components, except the mutations made in the Sec-translocase cleavage site to prevent the digestion

(A)
MKIKTGARILALSALTTMMFSASALAKHHHHHHGSSGENLYFQGADLEDNM
ETLNDNLKVIEKADNAAQVKDALTKMRAAALDAQKATPPKLEDKSPDSPEM
KDFRHGFDILVGQIDDALKLANEGKVKEAQAAAEQLKTTRNAYHQKYR

(B)
MKIKTGARILALSALTTMMFSASALVRHHHHHHGSSGENLYFQGADLEDNM
ETLNDNLKVIEKADNAAQVKDALTKMRAAALDAQKATPPKLEDKSPDSPEM
KDFRHGFDILVGQIDDALKLANEGKVKEAQAAAEQLKTTRNAYHQKYR

Figure 4.6. Amino acid sequence of Sec-cyt b_{562}. (A) Wilde type signaling sequence adapted from ref 27, the Sec translocase cleavage site is highlighted in yellow. (B) Mutated signaling sequence at the Sec translocase digestion site which is highlighted in yellow.

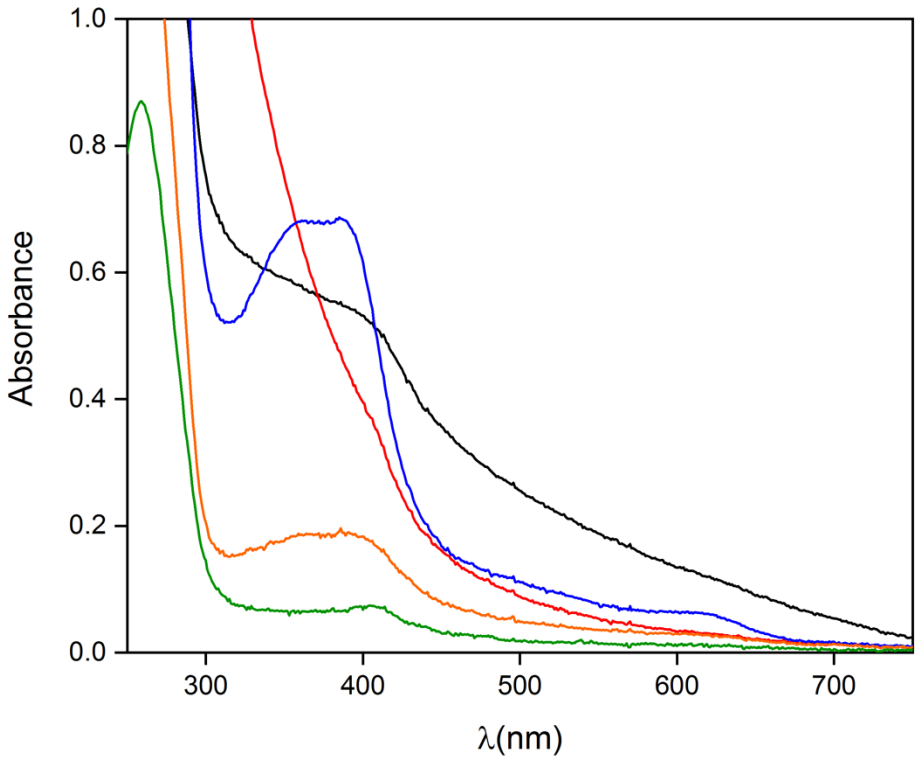

Figure 4.7. UV-Vis spectra of collected fractions after the outer membrane removal. Blue: supernatant after harvesting the cells and centrifugation, the small shoulder arises from the dissolved Co-PPIX in the media ; green: initial wash of the cell pellet with the fractionation buffer (750 mM sucrose, 100 mM Tris pH 8.0), this step has been done to remove the remaining Co-PPIX and media from the pellet and still contains some dissolved porphyrin; dark blue: periplasmic fraction, the broad feature at 395 nm represents dissolved porphyrin which penetrated to the periplasm through the outer membrane; red: spheroplasts, the peak at 427 nm indicates six-coordinated Co-PPIX in the cyt b_{562} binding pocket; yellow: spheroplasts and TEV protease digestion reaction mixture; the peak at 427 nm is more clear now as the protein is cut from the membrane and released into the solution.

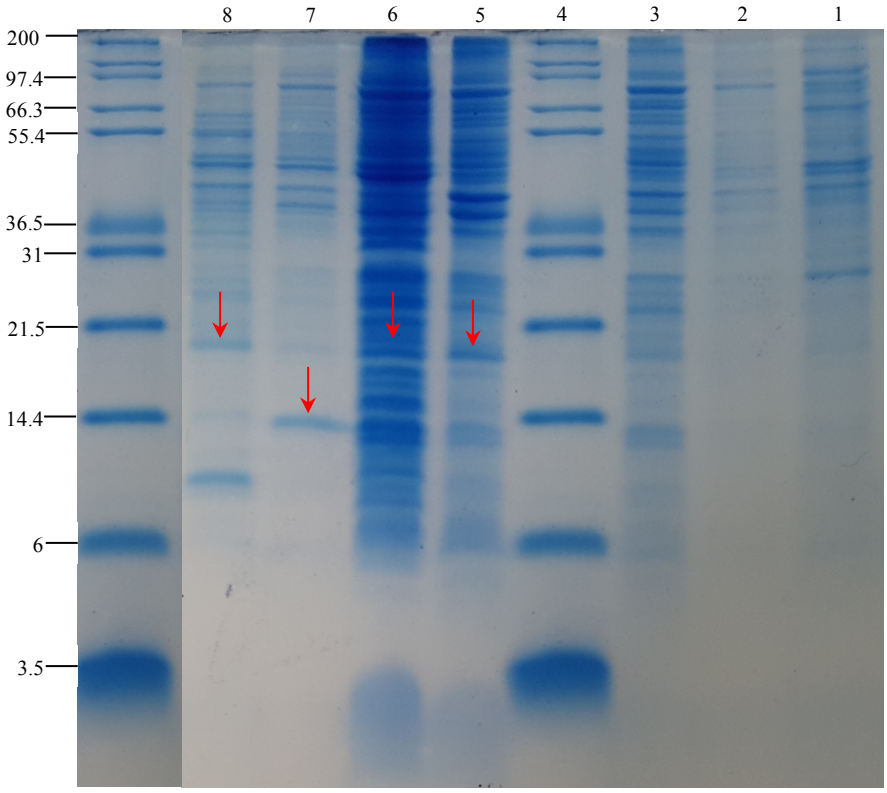

Figure 4.8. SDS-PAGE for the collect fractions from outer membrane removal and His tag digestion. Lines from right to left: 1) Sec-Co-cyt b_{562} supernatant after the first wash with the fractionation buffer, 2) Sec-Co-cyt b_{562} supernatant after washing with the fractionation buffer, EDTA, and $MgCl_2$, this step separates the periplasmic fraction and there is no band corresponding to digested Sec signaling sequence, indicative of the effectiveness of mutations in the digestion site 3) spheroplasts, or cells without the outer membrane, 4) M12 protein size marker, 5) spheroplasts and TEV protease reaction mixture, 6) spheroplasts and TEV protease reaction mixture flow through from the Ni-NTA purification, 7) spheroplasts and TEV protease reaction mixture wash from the Ni-NTA purification, and 8) spheroplasts and TEV protease reaction mixture elution from the Ni-NTA purification. The wash buffer was 50mM sodium phosphate, 1 M NaCl, 50 mM imidazole, pH 8.0. The elution buffer was 50mM sodium phosphate, 300mM NaCl, 300 mM imidazole, pH 8.0

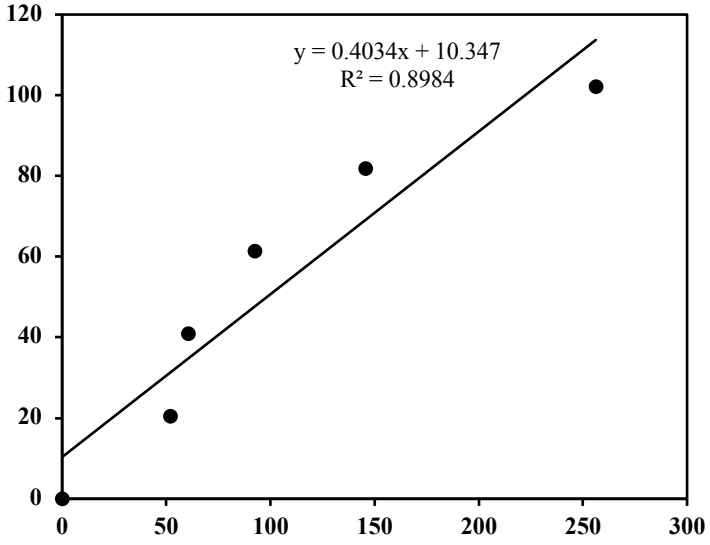

Figure 4.9. The calibration curve for light-induced hydrogen production with membrane-anchored Sec-Co-cyt b_{562}.

CHAPTER 5

CONCLUSIONS

In this dissertation, I have exploited protein design strategies and redox chemistry to achieve artificial metalloproteins and oxidoreductase enzymes. As a step forward from my lab's previous work in designing two [4Fe-4S] cluster-binding proteins and using the established design strategies developed in our group, we have shown the incorporation of multiple [4Fe-4S] clusters into repeat proteins. In this work, we demonstrated that the modular feature of Consensus Tetratricopeptide proteins along with their flexibility in molecular engineering offers a platform to incorporate multiple organometallic cofactors within their hydrophobic core. We were able to demonstrate the redox activity of designed [4Fe-4S]-CTPR proteins with respect to polarized electrodes as well as their neighboring amino acids. This study is a strong step in designing multiple cofactor-binding oxidoreductase proteins and can be extended to constructing multiple cluster binding systems with inter-cluster electron transfer capabilities with either adjusting the inter cluster distances or altering the primary coordination site of the cluster. This work can be expanded further by coupling light-harvesting molecules to CTPR-[4Fe-4S] proteins to design energy transfer systems.

In my second project, I have explored the catalytic activity of the heme-binding protein, cyt c, towards water oxidation. I designed a photoelectrochemical cell by transmetallating the heme cofactor with cobalt and using Antimony-doped Tin Oxide as a semiconductor and I interfaced Co-cyt c to the material as a water oxidation catalyst. Oxygen and hydrogen were produced in the system with the stoichiometric ratio and high Faradaic

efficiency, and the Incident-Photon to Current efficiency was calculated to be 4.1%. This system's overall acticity can be further expanded by coupling the designed photoanode to a hydrogen production photocathode, to obtain a tandem water-splitting cell.

In my third project, I designed a whole cell hydrogen production catalysis system utilizing inner-membrane anchored Co-cyt b_{562} in E. coli. Previous work in our lab has demonstrated the catalytic activity of this trans-metallated protein towards hydrogen production and CO_2 reduction. In this work, I employed a heme-deficient, albeit heme-permeable, strain of E. coli to express cyt b_{562} with a cobalt porphyrin. This strategy for cyt b_{562} expression with Co-porphyrin was used to solve the challenges associated with heme replacement protocols. Furthermore, the introduced inner-membrane display strategy offers the advantage of using whole cells for catalysis for compatible reactions, in this case hydrogen production. The catalytic activity of membrane-anchored cyt b_{562} with whole cells was proved in the presence of RuP as the photosensitizer and ascorbic acid as the sacrificial electron donor. The membrane-anchored cyt b_{562} offers a promising opportunity to develop high-throughput screening systems and directed evolution to enhance the hydrogen production and CO_2 reduction properties of the catalyst.

References

(1) Balzani, V.; Credi, A.; Venturi, M. Photochemical Conversion of Solar Energy. *Chem.Sus.Chem.* **2008**, 1(1-2), 26–58.

(2) Pearson, R. J.; Eisaman, M. D.; Turner, J. W. G.; Edwards, P. P.; Jiang, Z.; Kuznetsov, V. L.; Littau, K. A.; Di Marco, L.; Taylor, S. R. G. Energy Storage via Carbon-Neutral Fuels Made from CO 2, Water, and Renewable Energy. In *Proceedings of the IEEE.* **2012**, 100 (2), 440–460.

(3) Hambourger, M.; Moore, G. F.; Kramer, D. M.; Gust, D.; Moore, A. L.; Moore, T. A. Biology and Technology for Photochemical Fuel Production. *Chem. Soc. Rev.* **2009**, *38* (1), 25–35.

(4) Zhang, H.; Carey, A. M.; Jeon, K. W.; Liu, M.; Murrell, T. D.; Locsin, J.; Lin, S.; Yan, H.; Woodbury, N.; Seo, D. K. A Highly Stable and Scalable Photosynthetic Reaction Center-Graphene Hybrid Electrode System for Biomimetic Solar Energy Transduction. *J. Mater. Chem. A.* **2017**, *5* (13), 6038–6041.

(5) Golubitsky, M. An Introduction to Catastrophe Theory and Its Applications. *SIAM Rev.* **2005**, *20* (2), 352–387.

(6) Tachibana, Y.; Vayssieres, L.; Durrant, J. R. Artificial Photosynthesis for Solar Water-Splitting. *Nature Photonics*. **2012**, 6 (8), 511–518.

(7) Liu, J.; Chakraborty, S.; Hosseinzadeh, P.; Yu, Y.; Tian, S.; Petrik, I.; Bhagi, A.; Lu, Y. Metalloproteins Containing Cytochrome, Iron–Sulfur, or Copper Redox Centers. *Chem. Rev.* **2014**, *114* (8), 4366–4469.

(8) Moser, C. C.; Anderson, J. L. R.; Dutton, P. L. Guidelines for Tunneling in Enzymes. *Biochimica et Biophysica Acta - Bioenergetics*. 2010, pp 1573–1586.

(9) Winkler, J. R.; Gray, H. B. Electron-Transfer in Ruthenium-Modified Proteins. *Chem. Rev.* **1992**, *92* (3), 369–379.

(10) Gray, H. B.; Winkler, J. R. Electron Flow through Proteins. *Chem. Phys. Lett.* **2009**, *483* (1–3), 1–9.

(11) Armstrong, F. A.; Hirst, J. Reversibility and Efficiency in Electrocatalytic Energy Conversion and Lessons from Enzymes. *Proc. Natl. Acad. Sci.* **2011**, *108* (34), 14049–14054.

(12) Dewar, M. J.; Storch, D. M. Alternative View of Enzyme Reactions. *Proc. Natl. Acad. Sci. U. S. A.* **1985**, *82* (8), 2225–2229.

(13) Mulder, D. W.; Shepard, E. M.; Meuser, J. E.; Joshi, N.; King, P. W.; Posewitz, M. C.; Broderick, J. B.; Peters, J. W. Insights into [FeFe]-Hydrogenase Structure, Mechanism, and Maturation. *Structure.* **2011**, *19* (8), 1038–1052.

(14) Madden, C.; Vaughn, M. D.; Díez-P Erez, I.; Brown, K. A.; King, P. W.; Gust, D.; Moore, A. L.; Moore, T. A. Catalytic Turnover of [FeFe]-Hydrogenase Based on Single-Molecule Imaging. *J. Am. Chem. Soc.* **2012**, *134*, 1577–1582.

(15) Fontecilla-Camps, J. C.; Volbeda, A.; Cavazza, C.; Nicolet, Y. Structure/Function Relationships of [NiFe]- and [FeFe]-Hydrogenases. *Chem. Rev.* **2007**, *107* (10), 4273–4303.

(16) Eisenstein, K. K.; Wang, J. H.; Wang, J. H. Conversion of Light to Chemical Free Conversion of Light to Chemical Free Energy. I. Porphyrin-sensitized Photoreduction of ferredoxing by glutathione. *J. Biol. Chem.* **1969**, 244 (7), 1720-1728.

(17) Nanda, V.; Johnson, R. W.; Koder, R. L.; Author, N. C. Designing Artificial Enzymes by Intuition and Computation NIH Public Access Author Manuscript. *Nat Chem* **2010**, *2* (1), 15–24.

(18) Zastrow, M. L.; Peacock, A. F. A.; Stuckey, J. A.; Pecoraro, V. L. Hydrolytic Catalysis and Structural Stabilization in a Designed Metalloprotein. *Nat. Chem.* **2012**, *4* (2), 118–123.

(19) Busch, J. L. H.; Breton, J. L. J.; Bartlett, B. M.; James, R.; Hatchikian, E. C.; Thomson, A. J. Expression in Escherichia Coli and Characterization of a Reconstituted Recombinant 7Fe Ferredoxin from Desulfovibrio Africanus. *Biochem. J.* **2015**, *314* (1), 63–71.

(20) Farinas, E.; Regan, L. The de Novo Design of a Rubredoxin-like Fe Site. *Protein Sci.* **1998**, *7* (9), 1939–1946.

(21) Benson, D. E.; Wisz, M. S.; Liu, W.; Hellinga, H. W. Construction of a Novel Redox Protein by Rational Design: Conversion of a Disulfide Bridge into a Mononuclear Iron-Sulfur Center. *Biochemistry.* **1998**, *37* (20), 7070–7076.

(22) Nanda, V.; Rosenblatt, M. M.; Osyczka, A.; Kono, H.; Getahun, Z.; Dutton, P. L.; Saven, J. G.; DeGrado, W. F. De Novo Design of a Redox-Active Minimal Rubredoxin Mimic. *J. Am. Chem. Soc.* **2005**, *127* (16), 5804–5805.

(23) Robertson, D. E.; Farid, R. S.; Moser, C. C.; Urbauer, J. L.; Mulholland, S. E.; Pidikiti, R.; Lear, J. D.; Wand, A. J.; DeGrado, W. F.; Dutton, P. L. Design and Synthesis of Multi-Haem Proteins. *Nature.* **1994**, *368* (6470), 425–432.

(24) Takahashi, M.; Ueno, A.; Mihara, H. Peptide Design Based on an Antibody Complementarity-Determining Region (CDR): Construction of Porphyrin-Binding Peptides and Their Affinity Maturation by a Combinatorial Method. *Chem. - A Eur. J.* **2000**, *6* (17), 3196–3203.

(25) Dunetz, J. R.; Sandstrom, C.; Young, E. R.; Baker, P.; Van Name, S. A.; Cathopolous, T.; Fairman, R.; De Paula, J. C.; Åkerfeldt, K. S. Self-Assembling Porphyrin-Modified Peptides. *Org. Lett.* **2005**, *7* (13), 2559–2561.

(26) Koay, M. S.; Antonkine, M. L.; Gärtner, W.; Lubitz, W. Modelling Low-Potential [Fe4S4] Clusters in Proteins. *Chem. Biodivers*. **2008**, 5(8), 1571–1587.

(27) Zanello, P. Structure and Electrochemistry of Proteins Harboring Iron-Sulfur Clusters of Different Nuclearities. Part III. [4Fe-4S], [3Fe-4S] and [2Fe-2S] Iron-Sulfur Proteins. *J. Struct. Biol.* **2018**, 202 (3), 264–274.

(28) Grzyb, J.; Xu, F.; Nanda, V.; Łuczkowska, R.; Reijerse, E.; Lubitz, W.; Noy, D. Empirical and Computational Design of Iron-Sulfur Cluster Proteins. In *Biochim. Biophy. Acta. Bioenergetics*. **2012**, 1817, 1256–1262.

(29) Grzyb, J.; Xu, F.; Weiner, L.; Reijerse, E. J.; Lubitz, W.; Nanda, V.; Noy, D. De Novo Design of a Non-Natural Fold for an Iron–Sulfur Protein: Alpha-Helical Coiled-Coil with a Four-Iron Four-Sulfur Cluster Binding Site in Its Central Core. *Biochim. Biophys. Acta - Bioenerg.* **2010**, *1797* (3), 406–413.

(30) Chan, M. K. Recent Advances in Heme-Protein Sensors. *Curr. Opin. Chem. Biol*. **2001**, 216–222.

(31) A. Shelnutt, J.; Song, X.-Z.; Ma, J.-G.; Jia, S.-L.; Jentzen, W.; J. Medforth, C.; J. Medforth, C. Nonplanar Porphyrins and Their Significance in Proteins. *Chem. Soc. Rev.* **1998**, *27* (1), 31.

(32) Yu, Y.; Zhou, Q.; Wang, L.; Liu, X.; Zhang, W.; Hu, M.; Dong, J.; Li, J.; Lv, X.; Ouyang, H.; Li, H.; Gao, F.; Gong, W.; Lu, Y.; Wang, J. Significant Improvement of Oxidase Activity through the Genetic Incorporation of a Redox-Active Unnatural Amino Acid. *Chem. Sci.* **2015**, *6* (7), 3881–3885.

(33) Feng, J.-J.; Zhao, G.; Xu, J.-J.; Chen, H.-Y. Direct Electrochemistry and Electrocatalysis of Heme Proteins Immobilized on Gold Nanoparticles Stabilized by Chitosan. *Anal. Biochem.* **2005**, *342* (2), 280–286.

(34) Liu, J.; Chakraborty, S.; Hosseinzadeh, P.; Yu, Y.; Tian, S.; Petrik, I.; Bhagi, A.; Lu, Y. Metalloproteins Containing Cytochrome , Iron − Sulfur , or Copper Redox Centers. **2014**.

(35) Hara, M.; Waraksa, C. C.; Lean, J. T.; Lewis, B. A.; Mallouk, T. E. Photocatalytic Water Oxidation in a Buffered Tris(2,2‘-Bipyridyl)Ruthenium Complex-Colloidal IrO 2 System. *J. Phys. Chem. A* **2002**, *104* (22), 5275–5280.

(36) McDaniel, N. D.; Coughlin, F. J.; Tinker, L. L.; Bernhard, S. Cyclometalated Iridium(III) Aquo Complexes: Efficient and Tunable Catalysts for the Homogeneous Oxidation of Water. *J. Am. Chem. Soc.* **2008**, *130* (1), 210–217.

(37) Duan, L.; Bozoglian, F.; Mandal, S.; Stewart, B.; Privalov, T.; Llobet, A.; Sun, L. A Molecular Ruthenium Catalyst with Water-Oxidation Activity Comparable to That of Photosystem II. *Nat. Chem.* **2012**, *4* (5), 418–423.

(38) Kärkäs, M. D.; Åkermark, T.; Johnston, E. V.; Karim, S. R.; Laine, T. M.; Lee, B. L.; Åkermark, T.; Privalov, T.; Åkermark, B. Water Oxidation by Single-Site Ruthenium Complexes: Using Ligands as Redox and Proton Transfer Mediators. *Angew. Chemie - Int. Ed.* **2012**, *51* (46), 11589–11593.

(39) Dismukes, G. C.; Brimblecombe, R.; Felton, G. A. N.; Pryadun, R. S.; Sheats, J. E.; Spiccia, L.; Swiegers, G. F. Development of Bioinspired Mn $_4$ O $_4$ −Cubane Water Oxidation Catalysts: Lessons from Photosynthesis. *Acc. Chem. Res.* **2009**, *42* (12), 1935–1943.

(40) Jiao, F.; Frei, H. Nanostructured Cobalt Oxide Clusters in Mesoporous Silica as Efficient Oxygen-Evolving Catalysts. *Angew. Chemie - Int. Ed.* **2009**, *48* (10), 1841–1844.

(41) Ellis, W. C.; McDaniel, N. D.; Bernhard, S.; Collins, T. J. Fast Water Oxidation Using Iron. *J. Am. Chem. Soc.* **2010**, *132* (32), 10990–10991.

(42) Fillol, J. L.; Codolà, Z.; Garcia-Bosch, I.; Gàmez, L.; Pla, J. J.; Costas, M. Efficient Water Oxidation Catalysts Based on Readily Available Iron Coordination Complexes. *Nat. Chem.* **2011**, *3* (10), 807–813.

(43) Barnett, S. M.; Goldberg, K. I.; Mayer, J. M. A Soluble Copper-Bipyridine Water-Oxidation Electrocatalyst. *Nat. Chem.* **2012**, *4* (6), 498–502.

(44) Dürrenberger, M.; Ward, T. R. Recent Achievments in the Design and Engineering of Artificial Metalloenzymes. *Curr. Opin. Chem. Biol*. **2014**, 99–106.

(45) Ginovska-Pangovska, B.; Dutta, A.; Reback, M. L.; Linehan, J. C.; Shaw, W. J. Beyond the Active Site: The Impact of the Outer Coordination Sphere on Electrocatalysts for Hydrogen Production and Oxidation. *Acc. Chem. Res.* **2014**, *47* (8), 2621–2630.

(46) Wilson, M. E.; Whitesides, G. M. Conversion of a Protein to a Homogeneous Asymmetric Hydrogenation Catalyst by Site-Specific Modification with a Diphosphinerhodium(I) Moiety. *J. Am. Chem. Soc.* **1978**, *100* (1), 306–307.

(47) Ozaki Si; Roach, M. P.; Matsui, T.; Watanabe, Y. Investigations of the Roles of the Distal Heme Environment and the Proximal Heme Iron Ligand in Peroxide Activation by Heme Enzymes via Molecular Engineering of Myoglobin. *Acc. Chem. Res.* **2001**, *34* (10), 818–825.

(48) Ozaki, S.; Matsui, T.; Roach, M. P.; Watanabe, Y. Rational Molecular Design of a Catalytic Site: Engineering of Catalytic Functions to the Myoglobin Active Site Framework. *Coord. Chem. Rev.* **2000**, *198* (1), 39–59.

(49) Cammack, R.; Frey, M.; Robson, R. *Hydrogen as a Fuel Learning from Nature*; *CRC Press*. **2001**.

(50) Lewis, N. S.; Nocera, D. G. Powering the Planet: Chemical Challenges in Solar Energy Utilization. *Proc. Natl. Acad. Sci.* **2006**, *103* (43), 15729–15735.

(51) Abanades, S.; Flamant, G. Thermochemical Hydrogen Production from a Two-Step Solar-Driven Water-Splitting Cycle Based on Cerium Oxides. *Sol. Energy* **2006**, *80* (12), 1611–1623.

(52) Ceroni, P. The Exploration of Supramolecular Systems and Nanostructures by Photochemical Techniques. *Springer*, **2012**.

(53) Forrest, S. R.; Thompson, M. E. Introduction: Organic Electronics and Optoelectronics. *Chem. Rev.* **2007**, *107* (4), 923–925.

(54) Gray, H. B.; Winkler, J. R. Electron Flow through Proteins. *Chem. Phys. Lett.* **2009**, *483* (1–3), 1–9.

(55) Moser, C. C.; Keske, J. M.; Warncke, K.; Farid, R. S.; Dutton, P. L. Nature of Biological Electron Transfer. *Nature* **1992**, *355* (6363), 796–802.

(56) Hinchliffe, P.; Sazanov, L. A. Organization of Iron-Sulfur Clusters in Respiratory Complex I. *Science (80-.).* **2005**, *309* (5735), 771–774.

(57) Dayhoff, M. O.; Lippincott, E. R.; Eck, R. V. Thermodynamic Equilibria in Prebiological Atmospheres. *Science (80-.).* **1964**, *146* (3650), 1461–1464.

(58) Meyer, J. Iron–Sulfur Protein Folds, Iron–Sulfur Chemistry, and Evolution. *J. Biol. Inorg. Chem.* **2008**, *13* (2), 157–170.

(59) Beinert, H.; Holm, R. H.; Münck, E. Iron-Sulfur Clusters: Nature's Modular, Multipurpose Structures. *Science (80-.).* **1997**, *277* (5326), 653–659.

(60) Hosseinzadeh, P.; Lu, Y. Design and Fine-Tuning Redox Potentials of Metalloproteins Involved in Electron Transfer in Bioenergetics. *Biochim. Biophys. Acta - Bioenerg.* **2016**, *1857* (5), 557–581.

(61) Dey, A.; Jenney, F. E.; Adams, M. W. W.; Babini, E.; Takahashi, Y.; Fukuyama, K.; Hodgson, K. O.; Hedman, B.; Solomon, E. I. Solvent Tuning of Electrochemical Potentials in the Active Sites of HiPIP versus Ferredoxin. *Science.* **2007**, *318* (5855), 1464–1468.

(62) Calhoun, J. R.; Nastri, F.; Maglio, O.; Pavone, V.; Lombardi, A.; DeGrado, W. F. Artificial Diiron Proteins: From Structure to Function. *Biopolymers - Peptide Science Section*. **2005**, 264–278.

(63) Chakraborty, S.; Iranzo, O.; Zuiderweg, E. R. P.; Pecoraro, V. L. Experimental and Theoretical Evaluation of Multisite Cadmium(II) Exchange in Designed Three-Stranded Coiled-Coil Peptides. *J. Am. Chem. Soc.* **2012**, *134* (14), 6191–6203.

(64) Coldren, C. D.; Hellinga, H. W.; Caradonna, J. P. The Rational Design and Construction of a Cuboidal Iron-Sulfur Protein. *Proc. Natl. Acad. Sci. U. S. A.* **1997**, *94* (13), 6635–6640.

(65) Der, B. S.; Machius, M.; Miley, M. J.; Mills, J. L.; Szyperski, T.; Kuhlman, B. Metal-Mediated Affinity and Orientation Specificity in a Computationally Designed Protein Homodimer. *J. Am. Chem. Soc.* **2012**, *134* (1), 375–385.

(66) Ghirlanda, G.; Osyczka, A.; Weixia Liu, W.; Antolovich, M.; Smith, K. M.; P. Dutton, L.; Wand, J.; DeGrado W.F. De Novo Design of a D_2-Symmetrical Protein That Reproduces the Diheme Four-Helix Bundle in Cytochrome bc_1. *J. Am. Chem. Soc*. **2004**, 126 (26), 8141-8147.

(67) Grzyb, J.; Xu, F.; Nanda, V.; Łuczkowska, R.; Reijerse, E.; Lubitz, W.; Noy, D. Empirical and Computational Design of Iron-Sulfur Cluster Proteins. *Biochim. Biophys. Acta. Bioenerg.* **2012**, 1817, 1256–1262.

(68) Grzyb, J.; Xu, F.; Weiner, L.; Reijerse, E. J.; Lubitz, W.; Nanda, V.; Noy, D. De Novo Design of a Non-Natural Fold for an Iron–Sulfur Protein: Alpha-Helical Coiled-Coil with a Four-Iron Four-Sulfur Cluster Binding Site in Its Central Core. *Biochim. Biophys. Acta - Bioenerg.* **2010**, *1797* (3), 406–413.

(69) Salgado, E. N.; Radford, R. J.; Tezcan, F. A. Metal-Directed Protein Self-Assembly. *Acc. Chem. Res.* **2010**, *43* (5), 661–672.

(70) Zastrow, M. L.; Peacock, A. F. A.; Stuckey, J. A.; Pecoraro, V. L. Hydrolytic Catalysis and Structural Stabilization in a Designed Metalloprotein. *Nat. Chem.* **2012**, *4* (2), 118–123.

(71) Nanda, V.; Senn, S.; Pike, D. H.; Rodriguez-Granillo, A.; Hansen, W. A.; Khare, S. D.; Noy, D. Structural Principles for Computational and de Novo Design of 4Fe–4S Metalloproteins. *Biochim. Biophys. Acta - Bioenerg.* **2016**, *1857* (5), 531–538.

(72) Kennedy, M. L.; Gibney, B. R. Proton Coupling to $[4Fe\text{-}4S]^{2+/+}$ and $[4Fe\text{-}4Se]^{2+/+}$-Oxidation and Reduction in a Designed Protein. *J. Am. Chem. Soc.* **2002**, *124* (24), 6826–6827.

(73) Laplaza, C. E.; Holm, R. H. Helix-Loop-Helix Peptides as Scaffolds for the Construction of Bridged Metal Assemblies in Proteins: The Spectroscopic A-Cluster Structure in Carbon Monoxide Dehydrogenase. *J. Am. Chem. Soc.* **2001**, *123* (42), 10255–10264.

(74) Roy, A.; Sommer, D. J.; Schmitz, R. A.; Brown, C. L.; Gust, D.; Astashkin, A.; Ghirlanda, G. A De Novo Designed 2[4Fe-4S] Ferredoxin Mimic Mediates Electron Transfer. *J. Am. Chem. Soc.* **2014**, *136* (49), 17343–17349.

(75) Roy, A.; Sarrou, I.; Vaughn, M. D.; Astashkin, A. V.; Ghirlanda, G. *De Novo* Design of an Artificial Bis[4Fe-4S] Binding Protein. *Biochemistry* **2013**, *52* (43), 7586–7594.

(76) Main, E. R. G.; Phillips, J. J.; Millership, C. Repeat Protein Engineering: Creating Functional Nanostructures/Biomaterials from Modular Building Blocks. *Biochem. Soc. Trans.* **2013**, *41* (5), 1152–1158.

(77) Mejias, S. H.; Aires, A.; Couleaud, P.; Cortajarena, A. L. Designed Repeat Proteins as Building Blocks for Nanofabrication. *Adv. Exp. Med. Biol.* **2016**, *940*, 61–81.

(78) Kajander, T.; Cortajarena, A. L.; Main, E. R. G.; Mochrie, S. G. J.; Regan, L. A New Folding Paradigm for Repeat Proteins. *J. Am. Chem. Soc.* **2005**, *127* (29), 10188–10190.

(79) Mejías, S. H.; Sot, B.; Guantes, R.; Cortajarena, A. L. Controlled Nanometric Fibers of Self-Assembled Designed Protein Scaffolds. *Nanoscale* **2014**, *6* (19), 10982–10988.

(80) Mejias, S. H.; Couleaud, P.; Casado, S.; Granados, D.; Garcia, M. A.; Abad, J. M.; Cortajarena, A. L. Assembly of Designed Protein Scaffolds into Monolayers for

Nanoparticle Patterning. *Colloids Surf. B. Biointerfaces* **2016**, *141*, 93–101.

(81) Grove, T. Z.; Regan, L.; Cortajarena, A. L. Nanostructured Functional Films from Engineered Repeat Proteins. *J. R. Soc. Interface* **2013**, *10* (83), 20130051–20130051.

(82) Mejías, S. H.; López-Andarias, J.; Sakurai, T.; Yoneda, S.; Erazo, K. P.; Seki, S.; Atienza, C.; Martín, N.; Cortajarena, A. L. Repeat Protein Scaffolds: Ordering Photo- and Electroactive Molecules in Solution and Solid State. *Chem. Sci.* **2016**, *7* (8), 4842–4847.

(83) López-Andarias, J.; Mejías, S. H.; Sakurai, T.; Matsuda, W.; Seki, S.; Feixas, F.; Osuna, S.; Atienza, C.; Martín, N.; Cortajarena, A. L. Toward Bioelectronic Nanomaterials: Photoconductivity in Protein–Porphyrin Hybrids Wrapped around SWCNT. *Adv. Funct. Mater.* **2018**, *28* (24), 1704031.

(84) Couleaud, P.; Adan-Bermudez, S.; Aires, A.; Mejías, S. H.; Sot, B.; Somoza, A.; Cortajarena, A. L. Designed Modular Proteins as Scaffolds to Stabilize Fluorescent Nanoclusters. *Biomacromolecules.* **2015**, *16* (12), 3836–3844.

(85) Antonkine, M. L.; Maes, E. M.; Czernuszewicz, R. S.; Breitenstein, C.; Bill, E.; Falzone, C. J.; Balasubramanian, R.; Lubner, C.; Bryant, D. A.; Golbeck, J. H. Chemical Rescue of a Site-Modified Ligand to a [4Fe–4S] Cluster in PsaC, a Bacterial-like Dicluster Ferredoxin Bound to Photosystem I. *Biochim. Biophys. Acta - Bioenerg.* **2007**, *1767* (6), 712–724.

(86) Sweeney, W. V; Rabinowitz, J. C. Proteins Containing 4Fe-4S Clusters: An Overview. *Annu. Rev. Biochem.* **1980**, *49* (1), 139–161.

(87) Antonkine, M. L.; Koay, M. S.; Epel, B.; Breitenstein, C.; Gopta, O.; Gärtner, W.; Bill, E.; Lubitz, W. Synthesis and Characterization of de Novo Designed Peptides Modelling the Binding Sites of [4Fe-4S] Clusters in Photosystem I. *Biochim. Biophys. Acta - Bioenerg.* **2009**, *1787* (8), 995–1008.

(88) Vignais, P. M.; Billoud, B.; Meyer, J. Classification and Phylogeny of Hydrogenases. *FEMS Microbiology Reviews*. **2001**, 455–501.

(89) Jin, Z.; Heinnickel, M.; Krebs, C.; Shen, G.; Golbeck, J. H.; Bryant, D. A. Biogenesis of Iron-Sulfur Clusters in Photosystem I. *J. Biol. Chem.* **2008**, *283* (42), 28426–28435.

(90) Dubini, A.; Mus, F.; Seibert, M.; Grossman, A. R.; Posewitz, M. C. Flexibility in Anaerobic Metabolism as Revealed in a Mutant of Chlamydomonas Reinhardtii Lacking Hydrogenase Activity. *J. Biol. Chem.* **2009**, *284* (11), 7201–7213.

(91) Alexaki-Tzivanidou, H. Spectrophotometric Determination of Serum Iron with a New Reagent. *Top. Catal.* **1980**, *25* (3), 373–379.

(92) Bradford, M. M. A Rapid and Sensitive Method for the Quantitation of Microgram Quantities of Protein Utilizing the Principle of Protein-Dye Binding. *Anal. Biochem.* **1976**, *72* (1–2), 248–254.

(93) Sedmak, J. J.; Grossberg, S. E. A Rapid, Sensitive, and Versatile Assay for Protein Using Coomassie Brilliant Blue G250. *Anal. Biochem.* **1977**, *79* (1–2), 544–552.

(94) Mathews, R.; Charlton, Steven.; Sands, R.H.; Palmers, G. On the Nature of the Spin Coupling between the Iron-Sulfur Clusters in the Eight-Iron Ferredoxins. *J. Biol. Chem.* **1974**, *249*, 4326–4328.

(95) Hadzifejzovic, E.; Stankovic, J.; Firth, S.; McMillan, P. F.; Caruana, D. J. Plasma Electrochemistry: Electroreduction in a Flame. *Phys. Chem. Chem. Phys.* **2007**, *9* (39), 5335–5339.

(96) Hosseinzadeh, P.; Lu, Y. Design and Fine-Tuning Redox Potentials of Metalloproteins Involved in Electron Transfer in Bioenergetics. *Biochim. Biophys. Acta - Bioenerg.* **2016**, *1857* (5), 557–581.

(97) Aizman, A.; Case, D. A. Electronic Structure Calculations on Active Site Models for 4-Fe, 4-S Iron-Sulfur Proteins. *J. Am. Chem. Soc.* **1982**, *104* (12), 3269–3279.

(98) Van Stokkum, I. H. M.; Larsen, D. S.; Van Grondelle, R. Global and Target Analysis of Time-Resolved Spectra. *Biochim. Biophys. Acta. Bioenerg*. **2004**, 82–104.

(99) Aubert, C.; Mathis, P.; Eker, A. P. M.; Brettel, K. Intraprotein Electron Transfer between Tyrosine and Tryptophan in DNA Photolyase from Anacystis Nidulans. *Proc. Natl. Acad. Sci.* **2002**, *96* (10), 5423–5427.

(100) Glover, S. D.; Jorge, C.; Liang, L.; Valentine, K. G.; Hammarström, L.; Tommos, C. Photochemical Tyrosine Oxidation in the Structurally Well-Defined A3Y Protein: Proton-Coupled Electron Transfer and a Long-Lived Tyrosine Radical. *J. Am. Chem. Soc.* **2014**, *136* (40), 14039–14051.

(101) Walter, M. G.; Warren, E. L.; McKone, J. R.; Boettcher, S. W.; Mi, Q.; Santori, E. A.; Lewis, N. S. Solar Water Splitting Cells. *Chem. Rev.* **2010**, *110* (11), 6446–6473.

(102) Reece, S. Y.; Hamel, J. A.; Sung, K.; Jarvi, T. D.; Esswein, A. J.; Pijpers, J. J., H.; Nocera, D. G. Wireless Solar Water Splitting Using Silicon-Based Semeiconductors and Earth-Abundant Catalysts. *Science.* **2011**, *334*, 645–648.

(103) Sokol, K. P.; Robinson, W. E.; Warnan, J.; Kornienko, N.; Nowaczyk, M. M.; Ruff, A.; Zhang, J. Z.; Reisner, E. Bias-Free Photoelectrochemical Water Splitting with Photosystem II on a Dye-Sensitized Photoanode Wired to Hydrogenase. *Nature Energy*. *Nature*. **2018**, 944–951.

(104) Hisatomi, T.; Kubota, J.; Domen, K. Recent Advances in Semiconductors for Photocatalytic and Photoelectrochemical Water Splitting. *Chemical Society Reviews*. The Royal Society of Chemistry January 13, 2014, pp 7520–7535.

(105) Abdi, F. F.; van de Krol, R. Nature and Light Dependence of Bulk Recombination in Co-Pi-Catalyzed BiVO4 Photoanodes. *J. Phys. Chem. C.* **2012**, *116* (17), 9398–9404.

(106) Zhong, D. K.; Choi, S.; Gamelin, D. R. Near-Complete Suppression of Surface Recombination in Solar Photoelectrolysis by "Co-Pi" Catalyst-Modified W:$BiVO_4$. *J. Am. Chem. Soc.* **2011**, *133* (45), 18370–18377.

(107) Bourguignon, J.; Jaquinod, M. An Overview of the Arabidopsis Proteome. In *Plant Proteomics:* Technologies, Strategies, and Applications, *Nature*. **2008**, 5, 141–164.

(108) Sayama, K.; Nomura, A.; Arai, T.; Sugita, T.; Abe, R.; Yanagida, M.; Oi, T.; Iwasaki, Y.; Abe, Y.; Sugihara, H. Photoelectrochemical Decomposition of Water into H_2 and O_2 on Porous $BiVO_4$ Thin-Film Electrodes under Visible Light and Significant Effect of Ag Ion Treatment. *J. Phys. Chem. B*. **2006**, 110, 23, 11352-11360.

(109) Zhang, L.; Lin, C. Y.; Valev, V. K.; Reisner, E.; Steiner, U.; Baumberg, J. J. Plasmonic Enhancement in BiVO4photonic Crystals for Efficient Water Splitting. *Small* **2014**, *10* (19), 3970–3978.

(110) Jo, W. J.; Jang, J. W.; Kong, K. J.; Kang, H. J.; Kim, J. Y.; Jun, H.; Parmar, K. P. S.; Lee, J. S. Phosphate Doping into Monoclinic BiVO4for Enhanced Photoelectrochemical Water Oxidation Activity. *Angew. Chemie - Int. Ed.* **2012**, *51* (13), 3147–3151.

(111) Bonanni, B.; Andolfi, L.; Bizzarri, A. R.; Cannistraro, S. Functional Metalloproteins Integrated with Conductive Substrates: Detecting Single Molecules and Sensing Individual Recognition Events. *J. Phys. Chem. B* **2007**, *111* (19), 5062–5075.

(112) Das, R.; Kiley, P. J.; Segal, M.; Norville, J.; Yu, A. A.; Wang, L.; Trammell, S. A.; Reddick, L. E.; Kumar, R.; Stellacci, F.; Lebedev, N.; Schnur, J.; Bruce, B. D.; Zhang, S.; Baldo, M. Integration of Photosynthetic Protein Molecular Complexes in Solid-State Electronic Devices. *Nano Lett.* **2004**, *4* (6), 1079–1083.

(113) Hu, X. M.; Rønne, M. H.; Pedersen, S. U.; Skrydstrup, T.; Daasbjerg, K. Enhanced Catalytic Activity of Cobalt Porphyrin in CO2Electroreduction upon Immobilization on Carbon Materials. *Angew. Chemie - Int. Ed.* **2017**, *56* (23), 6468–6472.

(114) Pasternack, R. F.; Francesconi, L.; Raff, D.; Spiro, E. Aggregation of Nickel(II), Copper(II), and Zinc(II) Derivatives of Water-Soluble Porphyrins. *Inorg. Chem.* **1973**, *12* (11), 2606–2611.

(115) Ow, Y. L. P.; Green, D. R.; Hao, Z.; Mak, T. W. Cytochrome c: Functions beyond Respiration. *Nature. Rev. Mol. Cell Biol.* **2008**, 532–542.

(116) Wang, Y.; Qian, K.; Guo, K.; Kong, J.; Marty, J. L.; Yu, C.; Liu, B. Electrochemistry and Biosensing Activity of Cytochrome c Immobilized in Macroporous Materials. *Microchim. Acta* **2011**, *175* (1–2), 87–95.

(117) Deng, Z.; Gong, Y.; Luo, Y.; Tian, Y. WO_3 Nanostructures Facilitate Electron Transfer of Enzyme: Application to Detection of H_2O_2 with High Selectivity. *Biosens. Bioelectron.* **2009**, *24* (8), 2465–2469.

(118) Hulko, M.; Hospach, I.; Krasteva, N.; Nelles, G. Cytochrome c Biosensor-A Model for Gas Sensing. *Sensors.* **2011**, *11* (6), 5968–5980.

(119) Carey, A. M.; Zhang, H.; Mieritz, D.; Volosin, A.; Gardiner, A. T.; Cogdell, R. J.; Yan, H.; Seo, D. K.; Lin, S.; Woodbury, N. W. Photocurrent Generation by Photosynthetic Purple Bacterial Reaction Centers Interfaced with a Porous Antimony-Doped Tin Oxide (ATO) Electrode. *ACS Appl. Mater. Interfaces* **2016**, *8* (38), 25104–25110.

(120) Hou, K.; Puzzo, D.; Helander, M. C.; Lo, S. S.; Bonifacio, L. D.; Wang, W.; Lu, Z. H.; Scholes, G. D.; Ozin, G. A. Dye-Anchored Mesoporous Antimony-Doped Tin Oxide Electrochemiluminescence Cell. *Adv. Mater.* **2009**, *21* (24), 2492–2496.

(121) Simmons, C. R.; Schmitt, D.; Wei, X.; Han, D.; Volosin, A. M.; Ladd, D. M.; Seo, D. K.; Liu, Y.; Yan, H. Size-Selective Incorporation of DNA Nanocages into Nanoporous Antimony-Doped Tin Oxide Materials. *ACS Nano*. **2011**; 5, 6060–6068.

(122) Kwan, P.; Schmitt, D.; Volosin, A. M.; McIntosh, C. L.; Seo, D. K.; Jones, A. K. Spectroelectrochemistry of Cytochrome c and Azurin Immobilized in Nanoporous Antimony-Doped Tin Oxide. *Chem. Commun.* **2011**, *47* (45), 12367–12369.

(123) Pitre, S. P.; McTiernan, C. D.; Vine, W.; Dipucchio, R.; Grenier, M.; Scaiano, J. C. Visible-Light Actinometry and Intermittent Illumination as Convenient Tools to

Study Ru(Bpy)3Cl2 Mediated Photoredox Transformations. *Sci. Rep.* **2015**, *5* (1), 16397.

(124) Kleingardner, J. G.; Kandemir, B.; Bren, K. L. Hydrogen Evolution from Neutral Water under Aerobic Conditions Catalyzed by Cobalt Microperoxidase-11. *J. Am. Chem. Soc.* **2014**, *136* (1), 4–7.

(125) KONG, J.; YU, S. Fourier Transform Infrared Spectroscopic Analysis of Protein Secondary Structures. *Acta Biochim. Biophys. Sin. (Shanghai).* **2007**, *39* (8), 549–559.

(126) Frasca, S.; von Graberg, T.; Feng, J. J.; Thomas, A.; Smarsly, B. M.; Weidinger, I. M.; Scheller, F. W.; Hildebrandt, P.; Wollenberger, U. Mesoporous Indium Tin Oxide as a Novel Platform for Bioelectronics. *Chem.Cat.Chem.* **2010**, *2* (7), 839–845.

(127) Mersch, D.; Lee, C. Y.; Zhang, J. Z.; Brinkert, K.; Fontecilla-Camps, J. C.; Rutherford, A. W.; Reisner, E. Wiring of Photosystem II to Hydrogenase for Photoelectrochemical Water Splitting. *J. Am. Chem. Soc.* **2015**, *137* (26), 8541–8549.

(128) Bard, A. J.; Faulkner, L. R. Electrochemical Methods : Fundamentals and Applications. *Wiley*, **2001**.

(129) Thoi, V. S.; Sun, Y.; Long, J. R.; Chang, C. J. Complexes of Earth-Abundant Metals for Catalytic Electrochemical Hydrogen Generation under Aqueous Conditions. *Chemi. Soc. Rev*. **2013**, 2388–2400.

(130) Hu, X.; Brunschwig, B. S.; Peters, J. C. Electrocatalytic Hydrogen Evolution at Low Overpotentials by Cobalt Macrocyclic Glyoxime and Tetraimine Complexes. *J. Am. Chem. Soc.* **2007**, *129* (29), 8988–8998.

(131) Mondal, B.; Sengupta, K.; Rana, A.; Mahammed, A.; Botoshansky, M.; Dey, S. G.; Gross, Z.; Dey, A. Cobalt Corrole Catalyst for Efficient Hydrogen Evolution Reaction from H2O under Ambient Conditions: Reactivity, Spectroscopy, and Density Functional Theory Calculations. *Inorg. Chem.* **2013**, *52* (6), 3381–3387.

(132) Singh, W. M.; Baine, T.; Kudo, S.; Tian, S.; Ma, X. A. N.; Zhou, H.; Deyonker, N. J.; Pham, T. C.; Bollinger, J. C.; Baker, D. L.; Yan, B.; Webster, C. E.; Zhao, X. Electrocatalytic and Photocatalytic Hydrogen Production in Aqueous Solution by a Molecular Cobalt Complex. *Angew. Chemie - Int. Ed.* **2012**, *51* (24), 5941–5944.

(133) Schlettwein, D.; Jaeger, N. I.; Oekermann, T. Photoelectrochemical Reactions at Phthalocyanine Electrodes A2 - Kadish, Karl M. *The Porphyrin Handbook*;

Academic Press. **2003**, 247–283.

(134) Kellett, R. M.; Spiro, T. G. Cobalt(I) Porphyrin Catalysis of Hydrogen Production from Water. *Inorg. Chem.* **1985**, *24* (15), 2373–2377.

(135) Dalle, K. E.; Warnan, J.; Leung, J. J.; Reuillard, B.; Isabell, S.; Reisner, E. Immobilization of First Row Transition Metal Complexes for Electro- and Solar-Driven Fuel Synthesis. *Chem. Rev.* **2019**, *119* (4), 2752–2875.

(136) Kellett, R. M.; Spiro, T. G. Cobalt(I) Porphyrin Catalysts of Hydrogen Production from Water. *Inorg. Chem.* **1985**, *24* (15), 2373–2377.

(137) Lee, C. H.; Dogutan, D. K.; Nocera, D. G. Hydrogen Generation by Hangman Metalloporphyrins. *J. Am. Chem. Soc.* **2011**, *133* (23), 8775–8777.

(138) Kleingardner, J. G.; Kandemir, B.; Bren, K. L. Hydrogen Evolution from Neutral Water under Aerobic Conditions Catalyzed by Cobalt Microperoxidase-11. *J. Am. Chem. Soc.* **2014**, *136* (1), 4–7.

(139) Sommer, D. J.; Vaughn, M. D.; Ghirlanda, G. Protein Secondary-Shell Interactions Enhance the Photoinduced Hydrogen Production of Cobalt Protoporphyrin IX. *Chem. Commun.* **2014**, *50* (100), 15852–15855.

(140) Sommer, D. J.; Vaughn, M. D.; Clark, B. C.; Tomlin, J.; Roy, A.; Ghirlanda, G. Reengineering Cyt b_{562} for Hydrogen Production: A Facile Route to Artificial Hydrogenases. *Biochim. Biophys. Acta - Bioenerg.* **2016**, *1857* (5), 598–603.

(141) Anzaldi, L. L.; Skaar, E. P. Overcoming the Heme Paradox: Heme Toxicity and Tolerance in Bacterial Pathogens. *Infect. Immun.* **2010**, *78* (12), 4977–4989.

(142) CLOWES, R. C.; ROWLEY, D. Genetic Studies on Small-Colony Variants of Escherichia Coli K-12. *J. Gen. Microbiol.* **2009**, *13* (3), 461–473.

(143) Proenca, R.; Li, J. M.; Russell, C. S.; Cosloy, S. D.; Umanoff, H. Cloning of the Escherichia Coli K-12 HemB Gene. *J. Bacteriol.* **2016**, *170* (2), 1021–1025.

(144) Woodward, J. J.; Martin, N. I.; Marletta, M. A. An Escherichia Coli Expression-Based Method for Heme Substitution. *Nat. Methods* **2007**, *4* (1), 43–45.

(145) Okuda, J.; Hayashi, T.; Sauer, D. F.; Schwaneberg, U.; Polen, T.; Grimm, A. R.; Zhu, L. A Whole Cell E. Coli Display Platform for Artificial Metalloenzymes: Poly(Phenylacetylene) Production with a Rhodium–Nitrobindin Metalloprotein. *ACS Catal.* **2018**, *8* (3), 2611–2614.

(146) Rusch, S. L.; Kendall, D. A. Interactions That Drive Sec-Dependent Bacterial Protein Transport. *Biochem*. **2007**, 9665–9673.

(147) Freudl, R. Signal Peptides for Recombinant Protein Secretion in Bacterial Expression Systems. *Microbial Cell Factories*. **2018**.

(148) Inouye, M.; Itakura, K.; Inouye, S.; Soberon, X.; Franceschini, T.; Nakamura, K. Role of Positive Charge on the Amino-Terminal Region of the Signal Peptide in Protein Secretion across the Membrane. *Proc. Natl. Acad. Sci.* **2006**, *79* (11), 3438–3441.

(149) Kaye, S.S.; Long, J. R. Hydrogen Storage in the Dehydrated Prussian Blue Analogues $M_3[Co(CN)_6]_2$. *J. Am. Chem. Soc.* **2005**, *27* (12), 1574–1574.

(150) Goldstein, J.; Lehnhardt, S.; Inouye, M. In Vivo Effect of Asparagine in the Hydrophobic Region of the Signal Sequence. *J. Biol. Chem.* **1991**, *266* (22), 14413–14417.

(151) von Heijne, G. How Signal Sequences Maintain Cleavage Specificity. *J. Mol. Biol.* **1984**, *173* (2), 243–251.

(152) Kajava, A. V; Zolov, S. N.; Pyatkov, K. I.; Kalinin, A. E.; Nesmeyanova, M. A. Processing of Escherichia Coli Alkaline Phosphatase: Sequence Requirements and Possible Conformations of the -6 to -4 Region of the Signal Peptide. *J. Biol. Chem.* **2002**, *277* (52), 50396–50402.

(153) Itagaki, E.; Hager, L. P. Studies on Cytochrome b_{562} of Escherichia Coli I. Purification and Crystallization of Cytochrome b_{562}. **1966**, 241 (16), 3688-3695.

(154) Lycklama a Nijeholt, J. A.; Driessen, A. J. M. The Bacterial Sec-Translocase: Structure and Mechanism. *Philosophical Transactions of the Royal Society B: Biological Sciences*. **2012**, 1016–1028.

(155) Clifton, L. A.; Skoda, M. W. A.; Le Brun, A. P.; Ciesielski, F.; Kuzmenko, I.; Holt, S. A.; Lakey, J. H. Effect of Divalent Cation Removal on the Structure of Gram-Negative Bacterial Outer Membrane Models. *Langmuir.* **2015**, *31* (1), 404–412.

(156) Anderson, J. L. R.; Armstrong, C. T.; Kodali, G.; Lichtenstein, B. R.; Watkins, D. W.; Mancini, J. A.; Boyle, A. L.; Farid, T. A.; Crump, M. P.; Moser, C. C.; Dutton, P. L. Constructing a Man-Made c-Type Cytochrome Maquette in Vivo: Electron Transfer, Oxygen Transport and Conversion to a Photoactive Light Harvesting Maquette. *Chem. Sci.* **2014**, *5* (2), 507–514.